Investigation of Hydrodynamic and Depletion Interactions in Binary Colloidal Dispersions

Gregory K. James

Dissertation submitted to the faculty of Virginia Polytechnic Institute and State University in fulfillment of the requirements for the degree of

Doctor of Philosophy
In
Chemical Engineering

John Y. Walz, Co-Chair
William A. Ducker, Co-Chair
Stephen M. Martin
Richey M. Davis

December 10, 2013
Blacksburg, VA

Keywords: Colloidal Dispersions, Depletion and Structural Forces, Colloidal Stability, Atomic Force Microscopy

Investigation of Hydrodynamic and Depletion Interactions in Binary Colloidal Dispersions

Gregory K James

Abstract

Within a colloidal dispersion, the presence of negatively adsorbing material can produce a variety of effects on the dispersion properties and interactions. With increasing concentration, the negatively adsorbing material induces both depletion and structural forces on the dispersion, which can dramatically affect both colloidal stability and near-contact hydrodynamics. This project focused on expanding our understanding of the effects of such negatively adsorbing materials on both equilibrium and dynamic interactions between particles.

The effects of charged, hard spheres (silica nanoparticle) on the hydrodynamic drag force a particle experiences as it approaches a flat plate were measured experimentally using colloid probe atomic force microscopy (CP-AFM). Deviation was found between the measured drag force and predictions for the drag force in a simple, Newtonian fluid. The measured drag force was always smaller than the predicted drag force as the particle approached contact with the plate. An effective viscosity, that approached the dispersing fluid viscosity at contact and the bulk viscosity at large separations, was determined for the system. This effective viscosity displayed similar characteristics to those predicted theoretically by Bhattacharya and Blawzdziewicz (*J. Chem. Phys.* **2008**, *128*, 214704.).

The effects of both anionic and cationic micelles on the depletion and structural forces in a colloidal dispersion were studied both experimentally (with CP-AFM) and theoretically. The depletion and structural forces between a microparticle and a flat plate were measured and compared with the depletion force predicted by the force-balance model of Walz and Sharma (*J. Colloid Interface Sci.* **1994**, *168*, 485-496.). Consistent with previous work, the measured depletion force for both micelles was smaller in magnitude than that predicted by the Walz and Sharma model for hard, charged spheres. It is theorized that rearrangement of the micelle surfaces charges or physical deformation of the micelles may be responsible for the observed result. An effective surface potential for the micelles is proposed as a correction to the Walz and Sharma model.

Finally, the stability of colloidal dispersions was studied macroscopically in solutions of ionic micelles. The colloidal dispersions displayed clear flocculation behavior in both cationic and anionic micelles. This flocculation behavior was compared with energy profiles determined from CP-AFM experiments between a single particle and a flat plate. A simple phase diagram was proposed for predicting the stability of

colloidal dispersions based solely on the depth of the depletion energy well and the height of the repulsive energy barrier.

To my Dad,
Because a 4-year-old who wants a Ph.D. is normal

Acknowledgement

It is here that I would like to thank all of the people who have both directly and indirectly influenced this work and helped me in achieving the goal of earning my Ph.D.

First and foremost, I must thank my advisor Dr. John Walz whose support, trust, direction, and assistance made this dissertation possible. I thank him for his many years of guidance through both undergraduate and graduate school. In particular, I would like to thank him for the many lessons on presentation, both written and oral, that will serve me throughout my life and career.

I must also thank the members of my committee, Dr. William Ducker, Dr. Richey Davis, and Dr. Stephen Martin. I thank them for their many helpful conversations on both research and life over the years. In particular, I must also thank Dr. Ducker and Dr. Davis for the shared use of their lab spaces and equipment without which this research would not have been possible.

To the staff in the Department of Chemical Engineering office thank you for your endless patience. I'm not sure Dr. Walz gave you fair warning on how much his research group might disrupt you.

To my lab mates Shunxi, David, Francisco, and Wenle, I thank you all for your support, helpful conversations, and problem solving skills. You each have made the last four and a half years both fun and entertaining. To my many other friends throughout the department, both graduated and remaining, I thank you for the good times and many "happy-hours" we have shared together.

To my parents, Janice and Keith, thank you for your support from the day I was born. I know much of my success has been because of your love and patience. I was lucky to have parents who believed in my dreams as much as I did. To my in-laws, Roger and Karen, thank you for your many years of support and prayers as well.

Finally, to my wife Amy, who put her full support behind my dream thank you from the bottom of my heart. Without your patience, love, and encouragement none of this would have been possible.

Table of Contents

List of Figures

List of Tables

Attributions

Chapters 2-4: John Y. Walz, PhD, PI for this work, Department of Chemical and Materials Engineering at the University of Kentucky, currently Dean of Engineering at the University of Kentucky. Dr. Walz was a co-author on each of these papers and contributed to their editing and review.

Chapter 1 Introduction

1.1 Motivation and Significance

In the early 20th century it was observed that negatively adsorbing material could promote the flocculation of larger particles[1]. The induced stability or flocculation from negatively adsorbed material has come to be known as the depletion effect or the depletion force. Over the last 25 years many researchers have spent time studying the depletion force theoretically, computationally, and experimentally in a variety of systems that include colloidal dispersions of nanoparticles[2-11], micelles[11-20], polyelectrolytes[19,21-26], polymers[27-28], and rod-like[29-30] and disk-like[31-32] particles. The interactions of depletant materials play a vital role in many agricultural, biological, and industrial processes. Some of these processes include the production of milk and other food products, blood and tissue modeling and engineering, and the production and manufacturing of paints, coatings, and inks. In the coming years, colloidal dispersions are expected to become even more common with applications in reinforced polymer composites, cosmetics, and catalysis.

This work focuses on two previously unresolved issues in colloidal systems containing a negatively adsorbing species. The first is how the presence of a negatively adsorbed material impacts the near-contact hydrodynamic interaction between two surfaces. The second is whether the equilibrium forces between particles in dispersions of ionic micelles can be predicted using current models employed for particle interactions in dispersion of charged, hard spheres.

The hydrodynamic force has been well understood in simple, Newtonian fluids for more than 50 years[33]. However, little work has been done on the study of hydrodynamic interactions in complex fluids (i.e. fluids with one or more dispersed phases). This work seeks to characterize how colloidal interactions affect the longer range hydrodynamic force. Applications for these phenomena range from extrusion of nanocomposite reinforced polymers to pumping of mineral slurries, where the dynamic effects of colloidal particles are far more significant than those at equilibrium.

Micelles also offer a unique system of study that has direct applications in everyday life. Because micelles can literally be “turned-on and turned-off” simply by controlling their concentration, it is possible to create depletant induced flocculation and by simple dilution to create an environment that no longer favors flocculation. This concept has many applications in the industrial world because the depletant can simply be “washed away” unlike in systems which contain nanoparticles or polymers.

1.2 Overview of Sections

Chapter 2 opens with a review of the previous work performed in the area of colloidal hydrodynamics. Measured experimental results are presented for the hydrodynamic interaction of a large colloidal particle with a flat plate in dispersions of

nanoparticles. These results are compared to those of a theoretical model particle traveling through a simple, Newtonian fluid. For the system containing nanoparticles, an effective viscosity is determined for the gap region between the particle and plate that reduces in magnitude to the viscosity of the dispersing fluid as the particle and plate approach contact.

Chapter 3 begins with a review of the relevant literature in the field of depletion forces induced by micellar systems. Measured results are then presented for the depletion interaction of a large colloidal particle with a flat plate in solutions of ionic micelles of varying concentration. A comparison is made between these measurements and the results of a model for the depletion interaction produced by charged, hard-spheres. Poor agreement is found between the measured results and the model predictions and an explanation for this deviation is presented based on the unique properties of micelles.

Chapter 4 opens with a review of the relevant literature regarding the effects of depletion interactions on colloidal stability. Measured results are presented for the depletion energy profile acting between a large colloidal particle and a flat plate in solutions of ionic micelles of varying concentrations. The depletion energy profile is compared with results from macroscopic studies of colloidal stability. A simple phase diagram is presented for predicting the stability of colloidal silica particles in ionic micellar solutions.

Chapter 5 summarizes the work presented in this dissertation and clearly defines the major contributions to the field of colloidal dispersions. Recommendations are also presented regarding future work that would further extend the presented findings.

Appendix A reviews the topic of Atomic Force Microscopy including the development and history of the Atomic Force Microscope, its functional uses, and data analysis techniques. Appendix B presents a summary of other completed research.

Chapter 2 Hydrodynamic Force Measurements in Binary Colloidal Systems

The work described in this chapter was published under the title Hydrodynamic Force on a Microparticle Approaching a Wall in a Nanoparticle Dispersion: Observation of a Separation-Dependent Effective Viscosity in *Langmuir,* 2012, Volume 28, Issue 1, pp. 92-103. Reprinted with permission, American Chemical Society 2013.

2.1 Abstract

Colloid probe atomic force microscopy was used to measure the hydrodynamic force exerted on a 30 μm diameter silica particle being moved toward or away from a silica plate in aqueous dispersions of 22 nm diameter silica nanoparticles (6 or 8 vol.%). Upon comparing the measured force to predictions made using the well-known expression of Cox and Brenner[34] assuming a constant viscosity equal to that of the bulk dispersion, the measured drag force was found to become significantly less than that predicted at smaller particle-plate separation distances (*i.e.*, < 500 nm). A recent theoretical paper by Bhattacharya and Blawzdziewicz[35] predicted that in a solution of dispersed nanoparticles, the effective viscosity characterizing the hydrodynamic force on the particle should vary from that of the solvent at contact to that of the bulk dispersion at large separations. By adjusting the viscosity in the Cox and Brenner expression to make the predicted hydrodynamic force match that measured (*i.e*., the 'effective viscosity'), a curve showing these exact characteristics was obtained for the nanoparticle solutions. The effective viscosity profile was not a function of particle speed, and changes in the effective viscosity extended to separation distances as large as 2 μm (nearly 100 times the hard diameter of the nanoparticles). These results suggest that in the range of typical colloidal forces (order 100 nm), the dynamics of particle motion in such systems are determined by the viscosity of the solvent and not that of the bulk dispersion.

2.2 Introduction and Background

Understanding the hydrodynamic interaction between a colloidal particle and a solid surface is important in a number of natural and industrial processes, including particle filtration and capture, migration through porous media, and transport through the small channels of microfluidic devices. In the 1960's, Brenner and coworkers[33,36] developed relationships for the hydrodynamic force on a colloidal particle in near-contact motion near a solid wall. The friction factor for both normal and parallel motion is increased relative to that in the bulk due to lubrication flow in the gap region. In the limit of the particle-plate separation distance, h, approaching zero, the friction factor for *normal* motion was predicted to diverge at contact as a $1/h$ singularity. This equation assumes no-slip boundary conditions on both surfaces and negligible inertial effects.

With the development of advanced experimental tools, a number of experimental studies have been performed to validate these theoretical predictions. Chan and Horn[37] used the surface forces apparatus to measure the drainage rate of liquid films between crossed cylinders of mica in three nonpolar liquids. Excellent agreement with predictions was obtained for separations greater than 50 nm. At closer separations, the drainage rate was slower than predicted, which the authors attributed to nonshearing of the molecular layers closest to each solid surface.

Brown and coworkers[38-39] studied the interaction of a polystyrene latex particle and a quartz plate using total internal reflection microscopy (TIRM) and radiation pressure. The authors assumed the Brenner corrections to be valid in order to determine the absolute separation between the particle and plate. TIRM experiments were also conducted by Prieve and coworkers[40-41], who used the initial slope of the autocorrelation in scattered light intensity to determine the normal component of the particle's diffusion coefficient. The variation in this parameter with separation distance was found to agree well with predictions.

Adamcyk *et. al*.[42] measured the sedimentation rate of steel spheres through a viscous oil toward surfaces of various shape and found good agreement with theory. Walz and Suresh[43] used TIRM to measure the sedimentation of Brownian particles toward a flat plate for values of h/R, where R is the particle radius, between 0.01 and 0.05, and found good agreement between the measured rate of sedimentation and predicted values. Oetama and Walz[44] performed similar experiments, however by focusing on the short time random motion of the particle, the spatially-varying diffusion coefficient of the particle could be determined. Again, excellent agreement with theory was obtained. Honig *et. al*.[45] used colloid probe atomic force microscopy (CP-AFM) to measure the interaction between a 20 μm diameter particle and a flat plate in a sucrose solution. Their results were consistent with a no-slip boundary condition and Brenner's lubrication theory for a solution with constant viscosity.

Theoretical work in this area, including that of Brenner and coworkers, has focused almost exclusively on simple, Newtonian fluids as the dispersing medium, and

the experimental studies described above also utilized such fluids (primarily water). Recently, Bhattacharya and Blawzdziewicz[35] performed a theoretical analysis of the hydrodynamic force exerted on a particle (microparticle) approaching a solid wall in a dilute solution of smaller, nonadsorbing, spherical particles (nanoparticles). The authors considered the effect of charge on the particle surfaces by including an excluded shell around the surface of each particle and wall. The approach was to determine the effect of the nanoparticles on the velocity and pressure fields in the lubrication region. It was found that as the particle-plate gap width approached zero, the effective viscosity in the lubrication region approached that of the solvent. At large separations, the effective viscosity asymptotically approached that of the bulk dispersion. Perhaps most surprisingly was the distance over which the effective viscosity varied. Specifically, depending on the volume fraction and the size of the excluded shells, the effective viscosity was less than the bulk viscosity at separation distances as large as 20 nanoparticle diameters.

Experimental measurement of the hydrodynamic force on a sphere approaching a plate in a dispersion of nanoparticles has been obtained by Walz and coworkers. Using total internal reflection microscopy, Oetama and Walz[46] measured the diffusion coefficient of a 15 μm diameter polystyrene latex particle near a flat plate in a solution containing nanospheres or nanodiscs (laponite clay particles). The authors found that at relatively low concentrations of nanoparticles, the measured diffusion coefficients agreed relatively well with predictions made using the expression of Brenner and coworkers assuming an effective viscosity equal to the bulk viscosity. It should be noted, however, the majority of these experiments were conducted in solutions with a bulk viscosity that was only slightly larger than water (*i.e.*, within 20%) and that there was considerable scatter in the results.

Tulpar and Walz[9] used colloid probe atomic force microscopy to measure the force exerted on a 5 μm diameter silica sphere being driven toward a silica plate in aqueous solutions containing 22 nm diameter silica nanoparticles. At relatively small separation distances (<200 nm), the authors found the measured hydrodynamic force to be significantly less than predicted using the equations of Brenner and coworkers assuming an effective viscosity equal to the bulk viscosity. The authors postulated that this discrepancy could be caused by an offset in the measured separation distance, possibly arising from a finite amount of nanoparticle deposition on the surfaces of either the 5 μm silica sphere and silica plate. When the measured separation distances were adjusted upward by 44 nm (twice the nanoparticle diameter), much better agreement was obtained, especially at smaller separation distances (*i.e.*, < 100 nm). At separation distances above 100 nm, however, the measured hydrodynamic force remained significantly below that predicted.

In this current work, the experiments of Tulpar and Walz are expanded upon in an effort to better understand the effect of dispersed nanoparticles on the near-contact

hydrodynamic force exerted on a particle approaching a wall in a colloidal dispersion. Specifically, one of the limitations in the experiments of Tulpar and Walz was the maximum scan speed of the atomic force microscope used (approximately 11 μm/s) limited the magnitude of the hydrodynamic drag force that could be imposed. As a result, significant colloidal forces arising from the nonadsorbed nanoparticles (*i.e.*, depletion and structural forces) were always observed in the measured forces, which complicated the data analysis and also caused significant scatter in the resulting hydrodynamic forces. In the experiments described here, a different type of AFM was used which allowed much larger scan speeds (up to 100 μm/s possible).

One of the goals was to experimentally test the predictions of Bhattacharya and Blawzdziewicz. Specifically, we sought to determine whether a separation-dependent effective viscosity could indeed be detected and, if so, what is the length scale over which such variations occur.

2.3 Theory

2.3.1 Description of System

A schematic of the experimental system used in this work is shown in Figure 2-1. A single, micron-sized colloidal sphere of radius R that has been glued to the tip of a flexible AFM cantilever is moved toward or away from a solid plate in a fluid (this fluid can also contain dispersed nanoparticles of radius a). The cantilever moves at a constant speed, u_{scan}, in either direction. The tip of the cantilever deflects by amount δ toward or away from the plate in response to forces acting on the particle, which can be either from direct interactions with the plate (*i.e.*, electrostatic forces, depletion forces, structural forces) or from hydrodynamics arising from viscous drag. Because the spring constant, k, of the cantilever is known, this deflection, which can be measured using the position of a laser beam reflected from the back of the cantilever, can be directly converted into force.

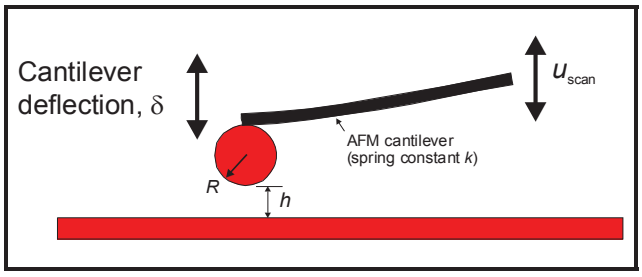

Figure 2-1. Schematic of the experimental system. A single, micron-sized colloidal particle is attached to the tip of an AFM cantilever. The cantilever is moved up or down at a set scan speed, u_{scan}, causing the particle to move toward or away from a solid plate. In response to forces exerted on the particle, the cantilever deflects by amount δ.

2.3.2 *Hydrodynamic Force Acting on Particle*

For a spherical particle of radius *R* being acted upon an external force **F** in a fluid, the particle's steady-state velocity **u** is given by

$$\mathbf{u} = m\mathbf{F} \qquad [2\text{-}1]$$

In this equation *m* is the hydrodynamic mobility. In the case of steady-state, this external force is balanced by the hydrodynamic force on the particle, $\mathbf{F}_{hydro}$. Eq. [2-1] assumes that Brownian effects can be ignored in predicting the particle velocity, which is completely valid in the experiments described here. The Stokes-Einstein relationship gives the mobility for a spherical particle in creeping flow (Reynolds numbers <<1) as

$$m = \frac{1}{6\pi\eta R} \qquad [2\text{-}2]$$

where η is the fluid viscosity.

The Stokes-Einstein relationship assumes the particle is moving through a fluid which is infinite and isotropic in all directions. However, when a particle is in proximity to a solid wall, its mobility is reduced from hydrodynamic interactions between the particle and wall. Brenner and coworkers[33,36] developed correction factors to the Stokes mobility for motion both normal and parallel the wall. The mobility for motion normal to the wall, $m_\perp$, can be expressed as

$$m_\perp = \frac{1}{6\pi\eta R\lambda_\perp} \qquad [2\text{-}3]$$

where $\lambda_\perp$ is the correction factor for normal motion.

The complete expression for $\lambda_\perp$ given by Brenner and coworkers is an infinite series in dimensionless separation distance α, defined as $\alpha = \cosh^{-1}(1 + h/R)$. Cox and Brenner[34] showed that when $h<R$, $\lambda_\perp$ can be approximated by

$$\lambda_\perp = \frac{R}{h} - 0.21\ln\left(\frac{h}{R}\right) + 0.97 \qquad [2\text{-}4]$$

A comparison of the values of $\lambda_\perp$ with those of the full series expression over the range of h/R values encountered in the experiments has shown that the approximate expression of Eq. [2-4] is quite accurate (*i.e.*, within 3% of the full series expression for h/R equal to 0.5). We have thus chosen to use this approximate expression in the modeling work described below.

Combining Eq. [2-1] and [2-4] gives the following expression for the hydrodynamic force exerted on a particle moving normally toward or away from a solid wall

$$F_{hydro,\perp} = -\frac{u}{m_\perp} = -6\pi\eta R\lambda_\perp u \qquad [2\text{-}5]$$

where the vector notation has been dropped since the focus is on normal motion only.

There are two primary assumptions that are important in this work: the Reynold's number must remain much less than 1.0 so that the creeping flow assumption remains valid, and inertial terms arising from the change in particle speed as it approaches the wall are small compared to frictional forces. (Although the scan speed in the experiments is constant, the actual speed at which the particle approaches the plate changes in response to deflection of the cantilever.) The Reynold's number for a spherical particle is $Du\rho/\eta$, where D is the particle diameter, u is the particle's velocity, and ρ and η are the density and viscosity of the fluid, respectively. For a 30 μm diameter particle moving in water at 50 μm/s (the maximum scan rate used in our experiments), the Reynolds number is of order $1\text{x}10^{-3}$.

For a particle undergoing acceleration, the complete force balance on the particle can be written as[47]

$$F_{external,\perp} + F_{hydro,\perp} = \left(m_s + m_f/2\right)\frac{\mathrm{d}^2 h}{\mathrm{d}t^2} \qquad [2\text{-}6]$$

In the system, $F_{external,\perp}$ is the external force exerted on the particle by the AFM cantilever and $F_{hydro,\perp}$ is the opposing hydrodynamic force exerted on the particle by the fluid (both of these forces act normal to the solid plate). The right-hand-side of Eq. [2-6] is the inertial term and accounts for acceleration of both the particle and the fluid displaced by the particle. Here m_s is the mass of the sphere, m_f is the mass of fluid displaced by the sphere, and $\frac{\mathrm{d}^2 h}{\mathrm{d}t^2}$ is the time derivative of the particle's instantaneous speed.

The mass of a 15 μm radius silica sphere of density 2.65 g/cm^3 is approximately $3.7\text{x}10^{-11}$ kg, while the mass of fluid (water) displaced by this sphere is approximately $1.4\text{x}10^{-11}$ kg. In reviewing the experimental results, the maximum change in dh/dt typically occurred around a separation distance of 20 nm, and a typical magnitude of d^2h/dt^2 at this position was order $1\text{x}10^4$ μm/s^2. Using these values, the right-hand-side of Eq. [2-6] is of magnitude $4\text{x}10^{-13}$ N. By comparison, the magnitude of the hydrodynamic force at this 20 nm separation distance, $F_{hydro,\perp}$, was roughly $2\text{x}10^{-9}$ N – four orders of magnitude larger. These values confirm that inertial terms can safely be neglected in our analysis.

2.3.3 Model of Particle Motion

In the colloid probe atomic force microscopy experiments, the force exerted on the particle as it is driven toward or away from the solid wall is measured simultaneously

with the particle's position. Correctly analyzing these results requires a model predicting the particle's position as a function of time.

As shown by Tulpar and Walz[9], the particle's instantaneous velocity, d*h*/d*t*, upon approach can be calculated as

$$\frac{\mathrm{d}h}{\mathrm{d}t} = -u_{scan} + \frac{\mathrm{d}\delta}{\mathrm{d}t} \quad [2\text{-}7]$$

where u_{scan} is the set peizo scan speed and δ is the instantaneous deflection of the cantilever. As discussed above, in our experiments the external spring force exerted on the particle by the cantilever, $-k\delta$, where k is the cantilever spring constant, is balanced by the hydrodynamic force. Because inertial terms are not important, we can thus write

$$k\delta = -6\pi\eta R\lambda_{\perp}\frac{\mathrm{d}h}{\mathrm{d}t} \quad [2\text{-}8]$$

Eq. [2-8] can be rearranged to

$$\delta = -B\lambda_{\perp}\frac{\mathrm{d}h}{\mathrm{d}t} \quad [2\text{-}9]$$

where B is the group of constants $B = 6\pi\eta R/k$.

Taking the derivative with respect to time of Eq. [2-9] and applying the chain rule yields

$$\frac{\mathrm{d}\delta}{\mathrm{d}t} = -B\left(\frac{\mathrm{d}\lambda_{\perp}}{\mathrm{d}t}\frac{\mathrm{d}h}{\mathrm{d}t} + \lambda_{\perp}\frac{\mathrm{d}^2h}{\mathrm{d}t^2}\right) = -B\left(\frac{\mathrm{d}\lambda_{\perp}}{\mathrm{d}h}\left(\frac{\mathrm{d}h}{\mathrm{d}t}\right)^2 + \lambda_{\perp}\frac{\mathrm{d}^2h}{\mathrm{d}t^2}\right) \quad [2\text{-}10]$$

Taking the derivative of Eq. [2-4] with respect to h gives

$$\frac{\mathrm{d}\lambda_{\perp}}{\mathrm{d}h} = -\frac{R}{h^2} - \frac{0.21}{h} \quad [2\text{-}11]$$

Finally, combining Eq. [2-7], [2-10], and [2-11] yields the following second order differential equation in time for the velocity of the particle

$$\frac{\mathrm{d}^2h}{\mathrm{d}t^2} = \frac{\left(B\left(\frac{R}{h^2} + \frac{0.21}{h}\right)\left(\frac{\mathrm{d}h}{\mathrm{d}t}\right)^2 - \frac{\mathrm{d}h}{\mathrm{d}t} - u_{scan}\right)}{B\lambda_{\perp}} \quad [2\text{-}12]$$

Given the scan speed, along with the particle's initial separation (h at t=0) and speed (dh/dt at t=0, assumed here to be equal to the scan speed), this equation allows determining the separation at any time t, assuming the assumptions inherent in its derivation remain valid (*i.e.*, no slip, constant viscosity).

Eq. [2-12] was solved using the known system parameters (measured spring constant, measured particle radius, scan speed, and bulk viscosity) and the built-in ODE solver (ode15s) in MATLAB (The Mathworks, Natick, MA, USA). ode15s is a variable

order, multistep solver based on the numerical differentiation formulas (NDFs). It is designed for solving ODEs which are "stiff". When running the ODE solver, the time step is defined to be on the order of 10^{-4} to 10^{-5} s to achieve convergent solutions.

2.4 Experimental

2.4.1 Materials

Water was purified using a Barnstead EASYpure II water purification system (Thermo Fisher Scientific Inc., Asheville, NC, USA) equipped with a 0.22 μm final filter. Solutions of 1.0 M KOH standard (Sigma-Aldrich Co., St. Louis, MO, USA) were diluted to 0.1 M and used to adjust the pH of the experimental solutions. The flat plates used in the AFM experiments were polished z-cut silica single crystals (MTI Corporation, Richmond, CA, USA) that measured 10.0 mm by 10.0 mm and had a thickness of 1.0 mm. The flats had a manufacturer's stated rms roughness <1.0 nm over 1 μm^2.

Microparticles used in AFM experiments were silica spheres ~30 μm in diameter and having a measured rms roughness <1.0nm over 1 μm^2 (Microsphere-Nanosphere, Cold Spring, NY, USA). Ludox TMA colloidal silica suspensions in deionized water (34 wt %) (Sigma-Aldrich Co., St. Louis, MO, USA) were used to prepare nanoparticle solutions. The manufacturer-reported nominal diameter of the nanoparticles was 22 nm. Van Blaaderen and Kentgens[48] measured the size of similar silica nanoparticles (Ludox AS-40 grade) and found their diameters to be 22.2±4.4 nm. Piech and Walz[19] also found good agreement with the manufactures-reported diameter for Ludox TMA, reporting a value for the diameter of 26 nm.

2.4.2 Solution Preparation

Ludox TMA solutions were prepared in a similar method to that of Tulpar and Walz[9]. Solutions were prepared in 30 mL polycarbonate bottles (Nalge Company, Rochester, NY, USA). When bottles were received they were cleaned with a 1% Liqui-Nox solution (Alconox, Inc., New York, NY, USA) for 2 h, rinsed with water and 200 proof ethanol, left in water for 2 h, and rinsed with water and ethanol again. If the bottles were being reused, they were cleaned with a 10 w/v % NaOH solution for a minimum of 4 h to remove any adsorbed silica from the walls of the bottles. Bottles were then rinsed with copious amounts of water and ethanol before use.

The different concentrations of solutions were prepared by diluting the stock Ludox TMA suspension. Ion-exchange resin (AG 501-X8, Bio-Rad Laboratories, Hercules, CA, USA) was then added to the solutions and bottles were placed on a vertical rotator overnight. After deionization, the solutions were passed through an 8 μm polycarbonate filter (Whatman, Piscataway, NJ, USA) to remove the resin. KCl salt (Thermo Fisher Scientific Inc., Fair Lawn, NJ, USA) was baked at 600°C for 6 h to remove possible organic contamination. The ionic strength of the solution was then adjusted using baked KCl and the pH of the solutions adjusted to ~7 using 0.1 M KOH. At this pH, the surfaces of all components should be strongly negatively charged.[49] The

solutions were then filtered a second time using a 1.0 μm filter (Whatman, Piscataway, NJ, USA). Hydrogen ion activities were measured using a Fisher Scientific Accumet XL20 pH meter (Thermo Fisher Scientific Inc., Fair Lawn, NJ, USA).

The concentration of the experimental solutions was checked using the procedure of Piech and Walz[19]. A known amount of nanoparticle solution was dried at 400°C for 24 h and then the weight fraction of silica was calculated and converted to a volume fraction. It was found that there was no significant loss in nanoparticle concentration during filtering.

2.4.3 Rheological Measurements

Viscosity measurements where performed using and Anton-Paar Physica MCR 301 rheometer with a Double-Gap system 26.7 mm in diameter. The temperature was controlled at 23°C by a Peltier plate system that surrounded the lower cup. The upper cylinder was rotational. Viscosity was measured as a function of shear rate by an increasing torque ramp. Graphs of viscosity versus shear rate were flat over the range of 1 to 1000 s^{-1}. The viscosities for 6 and 8 vol.% solutions at different ionic strengths are reported in Table 2-1. As expected, the viscosities were slightly larger at the higher nanoparticle concentration and decreased upon raising the ionic strength (reducing the electrostatic repulsion between the nanoparticles).

Ionic strength/mM	Viscosity of 6 vol.% nanoparticle solution/mPa-s	Viscosity of 8 vol.% nanoparticle solution/mPa-s
0.1	3.2	--
1.0	2.1	2.2
4.0	1.4	1.6

Table 2-1. Measured viscosities for 6 and 8 vol.% silica nanoparticle solutions at varying ionic strengths. (CP-AFM experiments were not performed with the 8 vol.% nanoparticle solution at 0.1 mM ionic strength, so the viscosity of this solution was not measured.)

2.4.4 Colloid Probe Atomic Force Microscope Measurements (CP-AFM)

Deflection-distance measurements were performed with a MFP-3D AFM (Asylum Research, Santa Barbara, CA, USA). These raw measurements were converted into force-separation data using the analysis method of Ducker *et. al*.[50] Silica microparticles were attached to AFM Cantilevers (ORC-8, Bruker AFM Probes, Camarillo, CA, USA) using a temperature curable epoxy (EPON 1004F Resin, Momentive, Columbus, OH, USA). The D-lever on the ORC-8 cantilever chip was used, which had a manufacturer-reported spring constant of 0.05 N/m. The spring constant for each cantilever used in the experiments was independently measured using the method of Hutter and Bechhoefer[51], and this measured value was used in the data analysis. The size of the spheres was measured after each experiment using a pixel counting ruler (MB-Ruler, MB-Softwaresolutions, Iffezheim, Germany). The ruler was calibrated using an AFM

calibration grating with a step size of 10 μm (Asylum Research, Santa Barbara, CA, USA).

Prior to each experiment the silica flats were soaked in 200 proof ethanol for 2 h and then rinsed with ethanol and water. The large silica spheres and AFM cantilevers were cleaned using UV radiation (UV/Ozone ProCleaner, Bioforce Nanosciences, Ames, IA, USA) for 15 min. The AFM fluid cell was sonicated in 200 proof ethanol for 1 h, rinsed with water, and then blown dry with nitrogen.

Multiple approach and withdrawal runs were performed in each experiment and average force curves were calculated to reduce noise. Scan ranges were ~7.35 μm with scan speeds ranging from 500 nm/s to 50 μm/s. At the end of each run, data was collected after the piezo stopped moving to determine the undeflected position (zero position) of the cantilever. Measurements were performed at room temperature, which was a steady 23°C.

2.5 Results

2.5.1 Colloidal Forces

Shown in Figure 2-2 is a typical approach force curve, measured here between a 30 μm diameter silica particle and a silica plate in an 8 vol.% silica nanoparticle solution (ionic strength of 1 mM) at scan speeds of 500 nm/s and 50 μm/s. For this and all subsequent curves, the effects of virtual deflection and cantilever resistance have been removed. (Details of the procedure used to remove these effects are provided in Appendix A.) At the slow speeds, oscillations are observed in the force curve, similar to those seen by Tulpar *et al*.[18] and Piech and Walz[19]. As explained by these authors, these oscillations are produced by structural forces and arise from oscillations in the concentration profile of the nanoparticles next to each surface.

At the higher scan speed, a pronounced long range repulsion is observed due to the hydrodynamic force exerted on the particle being pushed toward the plate. Interestingly, the oscillations are no longer present. While it is possible that the oscillatory forces are simply being overwhelmed by the large hydrodynamic force, another possibility is that the flow in the lubrication region is hampering the formation of the ordered layers of nanoparticles. This topic was discussed in greater detail by Tulpar and Walz[9].

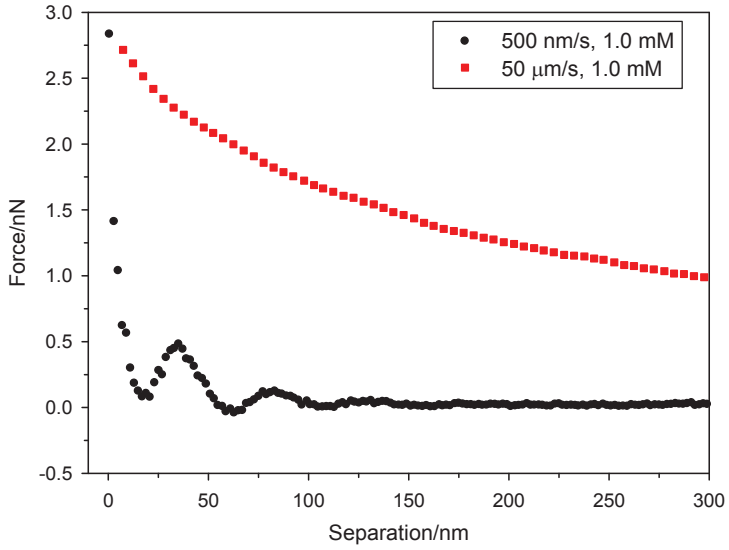

Figure 2-2. Comparison of the force profile at scan speeds of 500 nm/s and 50 μm/s. This data was taken in an 8 vol.% nanoparticle solution at 1 mM ionic strength.

2.5.2 Hydrodynamic Forces

One of the challenges in analyzing the measured results is to isolate the hydrodynamic component of the measured force. Specifically, once corrections to the measured force profile for the effects of virtual deflection and cantilever resistance have been made, the remaining forces are colloidal forces (*i.e.*, electrostatic forces, depletion forces, structural forces) and the hydrodynamic force on the particle.

In similar experiments, Tulpar and Walz[9] assumed that the hydrodynamic contribution to the measured force could be calculated by subtracting the forces measured upon approach and withdrawal at the same position and scan speed. Thus

$$F_{\text{hydro}} = 1/2\left(F_{measured,approach} - F_{measured,withdrawal}\right) \qquad [2\text{-}13]$$

The primary assumption with this approach is that at a given separation and scan speed, the colloidal forces will be the same upon approach and withdrawal and will thus cancel when the two measurements are subtracted.

For the present work, this method was not required, primarily because as shown in Figure 2-2, the measurements here were taken at much greater scan speeds than those used by Tulpar and Walz[9], meaning that the colloidal forces were generally much smaller than the hydrodynamic component. This was especially true at larger separation distances (*i.e.*, larger than several hundred nanometers) were colloidal forces have decayed substantially (evident in the 500 nm/s results in Figure 2-2). In addition, it was found that during the withdrawal of the particle away from contact with the plate, a large over-shoot in particle speed was observed at these high scan speeds. This overshoot occurred when the force exerted by the cantilever overcame the adhesion force and the particle 'snapped' away from the plate. Since this overshoot

was an unsteady event, data taken during this process could not be used. We therefore focused solely on the hydrodynamic force measured upon approach. (It should be mentioned that the overshoot did not affect the determination of either the virtual deflection or the cantilever resistance, discussed in Appendix A, since these corrections only used forces measured at large separation distances, beyond the range of the overshoot.)

Figure 2-3 shows a comparison between the measured results at 50 μm/s in Figure 2-2 and the prediction made using Eq. [2-12]. The specific conditions in the model calculations are given in the figure caption. Note that the model predictions were made using a constant bulk viscosity of 2.2×10^{-3} Pa-s. As can be seen, while the two curves converge at large separations, the measured force becomes significantly less than that predicted as contact is approached. Since the effects of virtual deflection and cantilever resistance have been removed from the measured profile, it is our hypothesis that this difference is caused by a reduction in the effective viscosity, as suggested by the predictions of Bhattacharya and Blawzdziewicz[35].

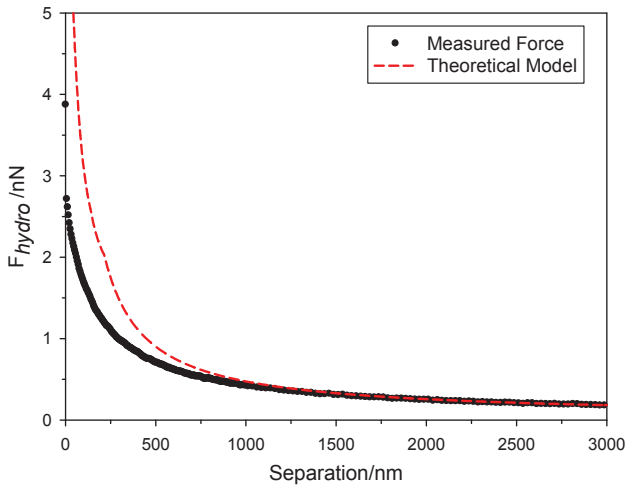

Figure 2-3. Comparison of the measured hydrodynamic force to the theoretical model. The theoretical curve was calculated using Eq. [2-12] and the following parameters: particle radius = 14.4 μm, initial separation distance = 7 μm, scan speed = 50 μm/s, spring constant = 0.0573 N/m, solution viscosity = 2.2×10^{-3} Pa-s.

Because the functional form of the relationship between effective viscosity and separation distance is not known *a priori*, the theoretical model of Eq. [2-12] cannot simply be used to determine this parameter. Specifically, in the derivation of Eq. [2-12], viscosity was assumed constant, thus the form of that equation is not correct here. Instead, an 'effective viscosity' has been calculated directly from the measured results using the following procedure:

1. For each measured profile, a polynomial fit was made relating the measured separation distance to time.
2. The derivative of this polynomial function with respect to time was taken at each measured separation distance and a curve of speed versus separation distance was then constructed. From the CP-AFM data, corrected for virtual deflection and cantilever resistance as described in Appendix A, the measured $F_{hydro,\perp}$ at each separation distance was determined.
3. The effective viscosity was then calculated as that needed to match the value of $F_{hydro,\perp}$, predicted using Eq. [2-5] and the speed obtained in step 2 to the measured $F_{hydro,\perp}$.

It should be emphasized here that this effective viscosity is not a true physical parameter of the system. Specifically, in the derivation of the drag correction factors by Brenner and coworkers[33,36], the fluid viscosity was assumed to be spatially invariant. Rather, this effective viscosity is defined here as the viscosity that allows matching the measured hydrodynamic force at a given position and velocity to predictions made using Eq. [2-5].

Figure 2-4 shows the effective viscosities obtained in this manner for 6 and 8 vol.% solutions at varying ionic strengths and scan speeds. For each ionic strength, the bulk measured viscosity is also plotted. As can be seen, the effective viscosity becomes approximately equal to the bulk value at separation distances ranging from 1 to 2 μm (roughly 50 to 100 nanoparticle diameters). It is also clear that the shape of the curve is unaffected by the scan speed.

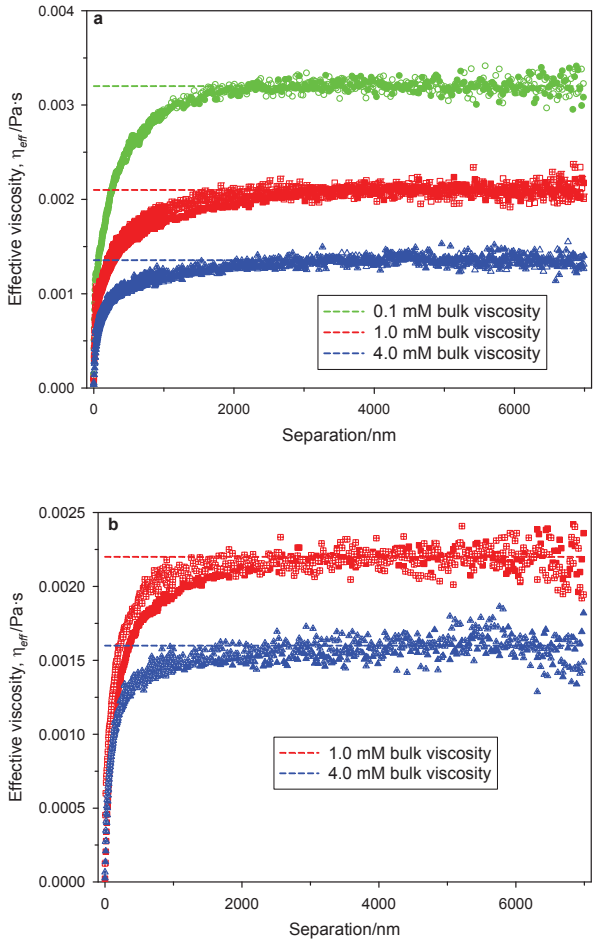

Figure 2-4. Effective viscosity obtained for (a) 6 vol.% and (b) 8 vol.% nanoparticle solutions at varying scan speeds and ionic strengths. The dashed lines in each graph represent the bulk viscosity at the indicated ionic strength, while the symbols correspond to the following scan speeds and ionic strengths:

(4a) ● 50 μm/s and 0.1 mM, ○ 40 μm/s and 0.1 mM,
■ 50 μm/s and 1.0 mM, □ 40 μm/s and 1.0 mM, ⊞ 20 μm/s and 1 mM,
▲ 50 μm/s and 4.0 mM, △ 40 μm/s and 4.0 mM, ⧋ 20 μm/s and 4.0 mM,

(4b) ■ 50 μm/s and 1.0 mM, ⊞ 20 μm/s and 1.0 mM.
▲ 50 μm/s and 4.0 mM, ⧋ 20 μm/s and 4.0 mM.

As the separation distance approaches zero, the effective viscosity falls toward that of pure water, and in many cases actually drops close to zero. While the qualitative trend is consistent with the prediction of Bhattacharya and Blawzdziewicz[35], an effective viscosity below that of pure water is obviously unrealistic.

Rather than suggesting a shortcoming in our analysis procedure, there is a much more practical explanation for this result, namely an error in the measured separation distance. As discussed in Appendix A, in a CP-AFM experiment, all separation

distances are measured relative to the point of hard contact between the test particles (glued to the cantilever) and plate. The assumption is that when such hard contact occurs, the spherical test particle is touching the plate.

What can alter this picture is surface roughness on either the large particle or plate. In addition to inherent roughness on the particle and plate, as discussed in Appendix A, there is also the possibility of a finite amount of nanoparticle deposition occurring. Although all surfaces in these experiments should be strongly negatively-charged, some deposition of nanoparticles is likely to occur, such as that due to heterogeneity in the surface charge density, and the presence of only one nanoparticle in the region of closest approach could alter the measured separation distance. A second possible explanation for an offset in the separation distance stems from the use of a relatively weak spring constant cantilever (ORC-8 D-Lever, nominal spring constant of 0.05 N/m). Due to the strong charges of the silica surfaces, it is possible the cantilever experiences a region of constant compliance before hard contact. Similar findings have been made by Piech and Walz[7], with the separation distance corrections being on the order of a few nanometers.

Using this assumption, the effective viscosities of Figure 2-4 are re-calculated with a procedure in which the actual separation distances were adjusted by amount h_{offset} in order to force the effective viscosity to equal that of pure water at contact (i.e., the result predicted by Bhattacharya and Blawzdziewicz[35]). In each case, the value of h_{offset} ranged between 10 and 50 nm. The facts that h_{offset} was (1) positive in each case, and (2) comparable to the nominal diameter of the nanoparticles used in these experiments (22 nm) is consistent with the explanation of roughness and/or nanoparticle deposition.

The re-calculated values of effective viscosity are shown in Figure 2-5. It should be emphasized while this adjustable parameter, h_{offset}, was needed to match the expected result at contact, *slightly offsetting the separation distance had essentially no effect on the shape of the curves nor on the range over which the effective viscosity varied*. This can be clearly seen by comparing the trends in Figure 2-4 and Figure 2-5.

A second possible contributing factor that should be mentioned is the presence of colloidal forces at small separation distances, which are ignored in the analysis. These would include van der Waals attraction, electrostatic repulsion between the highly charged microparticle and plate, and depletion and structural forced produced by the nanoparticles themselves. As seen in Figure 2-2, such forces are detectable at separations below approximately 100 nm. While these forces are assumed to be smaller than hydrodynamic drag over most of the separation distances sampled, it is possible that their contribution near contact is significant enough to affect the effective viscosities near contact. Because of the complex nature of these forces, their effect on the results is difficult to quantify. However, *it should again be stressed that such forces*

would not affect the curve at separations above roughly 100 nm, which is clearly well below the range over which viscosity changes are observed.

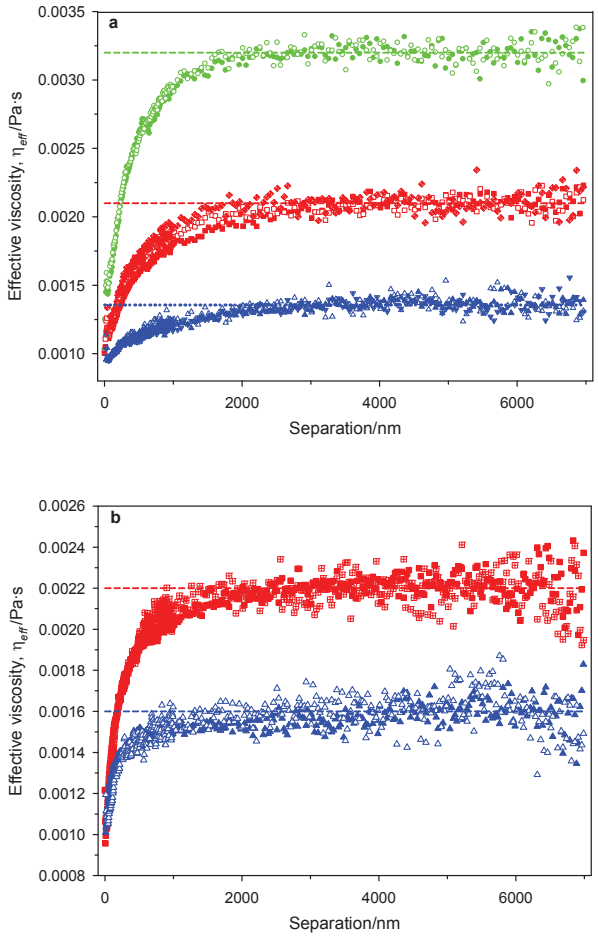

Figure 2-5. Effective viscosity calculation for (a) 6 vol.% and (b) 8 vol.% nanoparticle solutions from Figure 2-4, adjusted so that the effective viscosity equals that of the pure fluid at contact. The values of h_{offset} needed to force this match all range between 10 and 50 nm. The symbols and dashed lines in each graph are defined the same as in Figure 2-4.

Figure 2-6 replots the data in Figure 2-5 by rescaling the vertical axis as $\frac{\eta_{eff} - \eta_{water}}{\eta_{bulk} - \eta_{water}}$. Plotting the viscosities in this manner allows normalizing for different bulk viscosities such that the distance dependence of the viscosity can be examined in greater detail. As expected, the curves have a value of 0 at contact and asymptotically approach 1 at large separation distances. In addition, data taken at different scan speeds generally overlay, indicating that the variation in viscosity is not a function of the rate at which the particle approaches the plate. For the solution containing 6 vol.% nanoparticles (Figure 2-6a), decreasing the solution ionic strength from 4.0 mM to 0.1

mM results in a sharper rise in the effective viscosity toward the bulk value. This trend is opposite to that predicted by Bhattacharya and Blawzdziewicz and is discussed in greater detail in the Discussion section. For the 8 vol.% solution, little difference is observed between the 1.0 mM and 4.0 mM solutions.

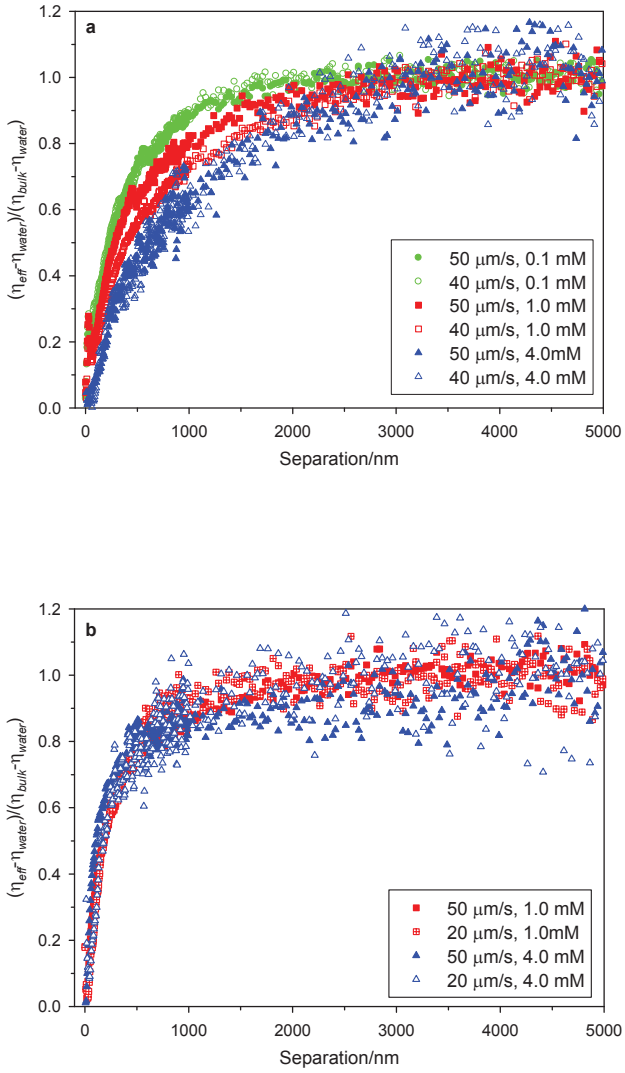

Figure 2-6. Effective viscosity results from Figure 2-5 replotted using a dimensionless effective viscosity for the (a) 6 vol.% and (b) 8 vol.% nanoparticle solutions. A dimensionless effective viscosity of 1.0 corresponds to the bulk viscosity while a value of zero corresponds to the pure fluid. The symbols in each graph are defined the same as in Figure 2-4 and Figure 2-5.

2.6 Discussion

2.6.1 Possible Role of Slip

There are three primary findings from the results presented above. First, the effective viscosity characterizing the hydrodynamic drag on the particle varies from that of the solvent at contact to that of the bulk dispersion and this variation occurs over length scales that are orders of magnitude larger than the hard-core size of the nanoparticle. Second, the effective viscosity does not depend on the scan rate used in the experiments, indicating that this is not a 'shear-thinning' effect. Third, in Figure 2-6a the length scale characterizing the change in effective viscosity appears to be smaller at the lower ionic strength. However, no significant difference in this length scale is seen in Figure 2-6b.

One of the issues that should be discussed before proceeding is the possible effect of slip at the solid/fluid interfaces in these experiments. The possible existence of slip in experiments of this type has been received quite a bit of attention recently[52-56], and slip could theoretically be a contributing factor in our results. Specifically, the onset of slip would lower the resulting hydrodynamic force between the particle and plate in a manner similar to that observed in the experiments.

However, there are several reasons that support our assertion that slip is not playing a significant role here. In a recent paper, Honig and Ducker[57] describe the results of a set of experiments made using colloidal probe atomic force microscopy specifically to test the validity of the no-slip boundary condition. Hydrophilic glass spheres with a radius of approximately 10 μm were glued to cantilever tips and then driven toward hydrophilic glass plates at drive speeds as large as 100 μm/s (twice the maximum speed used in our experiments). To increase the magnitude of the drag force, the authors used concentrated aqueous sucrose solutions as the suspending fluid. The hydrodynamic force on the particle was measured versus separation distance at varying viscosities and approach speeds.

To analyze their results, Honig and Ducker used the fact that as contact is approached ($h \rightarrow 0$), the drag correction of Eq. [2-4] can be approximated as simply $\lambda_{\perp} \approx R/h$. This allows rewriting the equation for the hydrodynamic drag (Eq. [2-5]) as

$$F_{hydro,\perp} = -\frac{6\pi\eta R^2}{h}\frac{\mathrm{d}h}{\mathrm{d}t}, \qquad [2\text{-}14]$$

which can be rearranged to

$$\frac{\frac{dh}{dt}}{F_{hydro,\perp}} = -\frac{h}{6\pi\eta R^2} \qquad [2\text{-}15]$$

Thus a plot of the approach rate divided by the hydrodynamic force versus *h* should yield a straight line that passes through the origin and has a slope of $1/6\pi\eta R^2$. The authors assumed that any slip would cause an offset in the distance at which the line passed through an ordinate value of zero (*i.e.*, x-intercept) and that the magnitude of this offset could be equated to the hydrodynamic slip length. In all experiments, the authors found that plotting their results in this manner yielded straight lines with slopes consistent with Eq. [2-15]. In addition, the slip lengths were essentially within experimental error of zero, leading them to conclude that the no-slip boundary condition was valid.

As further confirmation on the lack of slip in our experiments, we repeated this analysis using two sets of results, shown in Figure 2-7. The first set was obtained in a 1 mM ionic strength aqueous solution without any added nanoparticles (these results are also presented in Figure A-6 in Appendix A), while the second set was data obtained from an 8 vol.% nanoparticle solution with an approach speed of 20 μm/s. It is clear that in the water solution (no nanoparticles), the data is well-described by a straight line. Using the regressed slope of the data, a viscosity of 1.05×10^{-3} Pa-s was calculated, which agrees well with the expected value for pure water, supporting the assertion that slip is minimal in this system. By comparison, the data for the nanoparticles solution shows a clear curvature. Since the fluid/solid interfaces are the same in both systems (*i.e.*, water/silica), the hydrodynamic boundary conditions should also be the same, meaning that the curvature seen in the results from the nanoparticle dispersion in Figure 2-7 would not be due to slip.

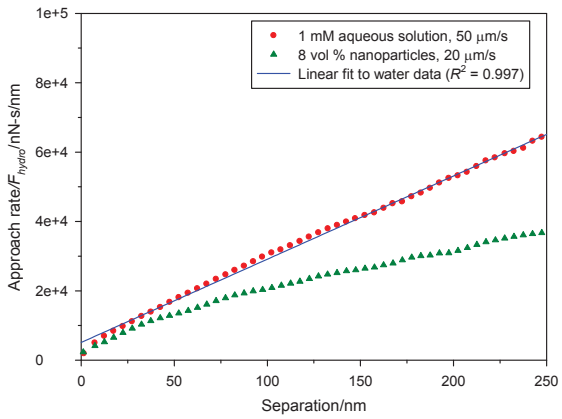

Figure 2-7. Plots of approach rate divided by hydrodynamic drag force versus separation distance for experiments in both water and an 8 vol.% nanoparticle solution.

2.6.2 Physical Explanation of Findings

Shown in Figure 2-8 is a simple schematic of the distribution of nanoparticles in our system, which can also be used to understand our results. Around each particle and surface is a dashed line representing a repulsive barrier, which in this case is due to an electrostatic repulsion between the like-charged silica surfaces. The thickness of this barrier will be of order the solution Debye length. (For example, Odiachi and Prieve[32] and Piech and Walz[58] found that the hard sphere depletion model of Asakura and Oosawa[59] could be matched to the depletion force in charged systems by adding approximately five Debye lengths to the radius of the suspended nanoparticles.) Here, the repulsive barrier is treated as a hard wall that limits the distance of closest approach between surfaces. The light blue region around the microparticle and wall denote the exclusion region and represents the closest distance that the center of a nanoparticle can approach. Because the concentration of nanoparticles inside this region is zero, the viscosity in the region is that of the pure fluid.

As can be seen in this schematic, even when the separation distance is much greater than a nanoparticle diameter, a significant fraction of the lubrication region (characteristic dimension $\sqrt{Rh}$ measured laterally from the distance of closest approach) will be pure fluid. In the Bhattacharya and Blawzdziewicz[35] model, interactions between the nanoparticles were ignored (dilute solution approximation), such that while the nanoparticle concentration inside the exclusion layers was zero, the concentration outside was that of the bulk. Because it is the lubrication region that primarily controls the frictional resistance exerted on the particle as it approaches the plate, the effective viscosity for the flow in this region will be less than that of the bulk. (Another way of thinking about this is that the *average* concentration of nanoparticles in the lubrication region, which is obtained by integrating the local concentration profile over this region, will be less than that in the bulk.)

Consider for example, a 1 mM ionic strength solution in which the bulk Debye length is approximately 10 nm. Since the nanoparticle radius in these experiments is also approximately 10 nm, the thickness of the exclusion layer surrounding each surface would be roughly 60 nm (assuming the effective radius of the nanoparticle can be approximated as the hard sphere radius plus five Debye lengths, as discussed above). Thus when the separation distance between the particle and plate is 1 μm, for example, 120 nm of this distance (12%) will be essentially pure fluid. At larger distances, the percentage of the lubrication region consisting of pure fluid will decrease, asymptotically approaching zero.

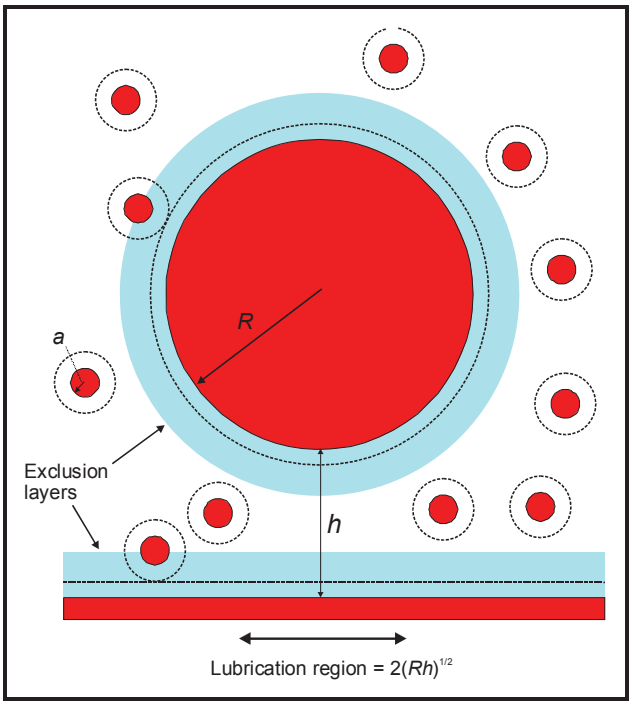

Figure 2-8. This schematic shows how nanoparticles are excluded from areas next to the surface of the microparticle and plate. The dashed line next to each surface indicates the thickness of the repulsive barrier caused by electrostatic interactions. The areas in light blue denote the region next to the surface and the plate from which the nanoparticles are excluded. Since the nanoparticle concentration in these regions is zero, the fluid viscosity inside will be that of the pure fluid.

Conversely, as the separation distance decreases, the fraction of the lubrication region that is pure fluid increases, meaning the effective viscosity becomes closer to that of the pure solvent. At sufficiently small separations, the excluded regions around the particle and plate actually overlap, as shown in Figure 2-9. Now, the nanoparticles also become excluded from the region around the centerline connecting the particle center and plate (shown as the broken line in the figure), and the size of this region expands as the separation distance becomes smaller. This may explain the more rapid decrease in effective viscosity that is observed as the separation distances decreases (*i.e.,* in Figure 2-5).

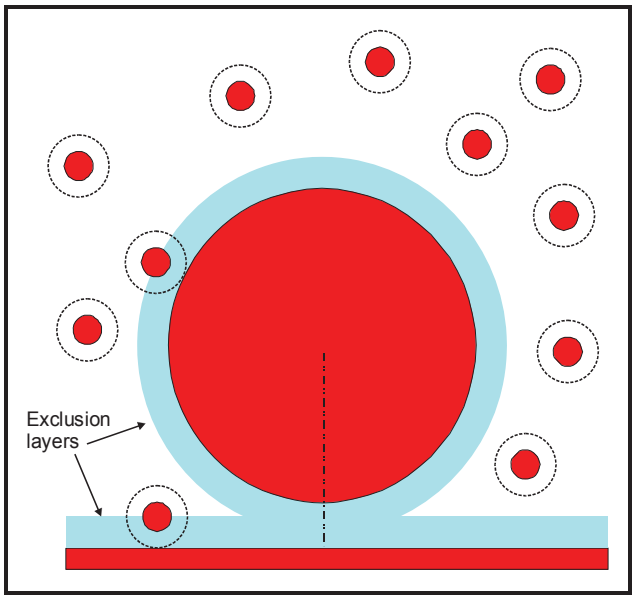

Figure 2-9. This schematic shows the overlap of the exclusion layers at smaller separation distances. Now, the nanoparticles are excluded from the gap region near the point of closest approach, indicated by the broken line.

This description explains why there is no effect of scan speed on the effective viscosity profile. *Essentially, the reduced viscosity arises from the exclusion of nanoparticles from regions next to the particle and plate and this exclusion is independent of the rate at which the particle approaches the plate.*

A more interesting observation is the effect of ionic strength. Bhattacharya and Blawzdziewicz found that when the thickness of the repulsive barrier around the surfaces increased, such as by increasing the solution Debye length, the characteristic length scale of the viscosity change also increased. Intuitively, this is what would be expected, since increasing the thickness of the repulsive barrier would also increase the thickness of the exclusion layers shown in Figure 2-8, meaning that an even greater portion of the lubrication region would consist of pure fluid.

However, Figure 2-6a shows just the opposite effect when the ionic strength is lowered from 4.0 mM to 0.1 mM (Debye length increases from 4.81 nm to 30.4 nm), while Figure 2-6b shows that lowering the ionic strength from 4.0 mM to 1.0 mM (increasing the Debye length from 4.81 nm to 9.61 nm) has essentially no effect on the range of the viscosity change.

One possible explanation for this finding is the interaction between the nanoparticles themselves, which are significant in our system but ignored in the work of Bhattacharya and Blawzdziewicz. As shown in Figure 2-2, at slow scan speeds, significant oscillations in the force profile can be observed. These structural forces arise due from oscillations in the concentration of the nanoparticles next to the surfaces, which has been predicted[3,5,60] and measured[11,61-64,] by numerous researchers. In addition, Piech and Walz[19] showed that lowering the solution ionic strength (increasing

the Debye length) greatly increases the magnitude of these force oscillations, while Tata *et al*.[65] showed that the amplitude of oscillation in the concentration of charged particles confined between two walls increased as the ionic strength decreased. In the Bhattacharya and Blawzdziewicz model, the concentration at any point in the fluid was either equal to zero (inside the exclusion layers) or the bulk concentration (outside the exclusion layers), meaning the local viscosity was either that of the pure fluid or of the bulk. However, oscillations in concentration mean that the local viscosity can vary greatly, even far above the bulk viscosity since the local nanoparticle concentration can exceed that of the bulk[60].

Shown in Figure 2-10 is a plot of measured bulk viscosity versus nanoparticle concentration for our system. The ionic strength here was 1 mM. As seen, the viscosity increases nonlinearly with increasing nanoparticle concentration. What this means is that lowering the ionic strength and increasing the solution Debye length can have competing effects. On one hand, the larger Debye length will increase the size of the exclusion layers, which will tend to extend the range over which viscosity changes are seen, consistent with that predicted by Bhattacharya and Blawzdziewicz. On the other hand, the larger Debye lengths will also lead to greater oscillations in nanoparticle concentration in the gap region, and the high-concentration regions of these oscillations will tend to increase the local viscosity significantly. Thus the overall effect of changing the ionic strength on the shape of the effective viscosity profile could depend in a complex manner on these two competing effects. Although not observed in our experiments, it would be interesting to investigate whether these oscillations in concentration could even lead to an effective viscosity that actually exceeded that of the bulk.

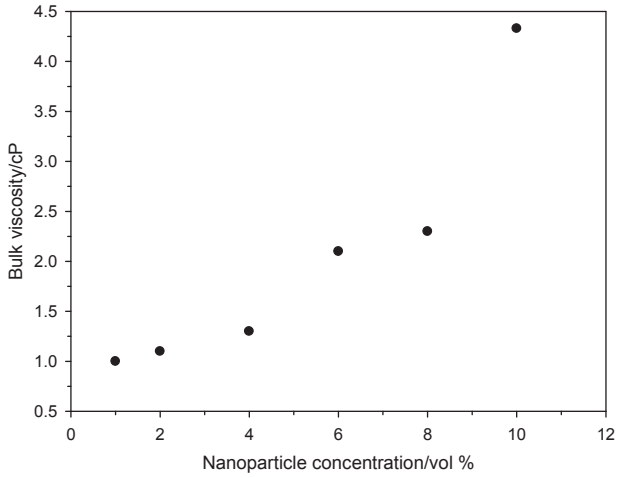

Figure 2-10. Bulk solution viscosity versus volume fraction of silica nanoparticles. The ionic strength here was 1 mM.

One of the important implications of these results lies in the prediction of particle dynamics in the range of surface forces. Specifically, the characteristic range of most surface forces, such as electrostatic and van der Waals forces, is typically tens of nanometers. For structural forces, such as those seen in Figure 2-2, the length scale can be larger, but is still of order 100 nm. In looking at the effective viscosities shown in Figure 2-5, it is clear that the value of the effective viscosity in this range will be approximately equal to that of the solvent. This implies that in complex solutions containing a dispersed component, calculation of the dynamic behavior in response to typical colloidal forces should be based on the viscosity of the solvent and not on that of the bulk solution.

2.7 Conclusions

Measurements of the hydrodynamic drag force exerted on a micron-sized colloidal particle moving normal to a solid plate in a solution of nonadsorbed nanoparticles show a pronounced dependence of the effective viscosity characterizing the frictional resistance on particle-plate separation distance. The results are in qualitative agreement with the predictions of Bhattacharya and Blawzdziewicz[35] in that the effective viscosity varies from that of the solvent at contact to that of the bulk dispersion at distances that are orders of magnitude larger than the nanoparticle diameter.

The effective viscosity profile was not found to be a function of the scan speed used to measure the force. However, changing the solution ionic strength had a complex effect, as in one case the characteristic length of the range of the change in the effective viscosity actually decreased upon lowering the ionic strength, opposite to the predictions of Bhattacharya and Blawzdziewicz, while in another case altering the ionic strength had no apparent effect on this length. It is suggested that this complex behavior may be related to interactions between the nanoparticles themselves, which are significant at the nanoparticle concentrations used here.

These results would have application in predicting transport rates of particles next to stationary surfaces in complex fluids containing a dispersed phase. Specifically, it is the solvent viscosity that should be used in such predictions and not that of the bulk solution.

Chapter 3 Investigation of the Depletion and Structural Forces Produced by Ionic Micelles

The work described in this chapter was published under the title Experimental and Theoretical Investigation of the Depletion and Structural Forces Produced by Ionic Micelles in Colloids and Surfaces A: Physicochemical and Engineering Aspects, 2014, Volume 441, pp. 406-419. Reprinted with permission, Elsevier 2013.

3.1 Abstract

The technique of colloid probe atomic force microscopy was used to measure the force profile between a silica particle and a flat silica plate in solutions of tetradecyltrimethylammonium bromide (C_{14}TAB) and sodium dodecylsulfate (SDS) at varying concentrations. With increasing surfactant concentration the onset of a depletion well and structural forces was observed. The measured results were compared to the predicted results of the model of Walz and Sharma[4] for hard, charged, spherical depletants. For C_{14}TAB the measured depletion force was substantially smaller in magnitude than that predicted by this model. In solutions of SDS micelles, a similar overestimation of the depletion force was observed but not to the same degree as for the C_{14}TAB solutions. It was found that by reducing the magnitude of the electrostatic repulsive interactions in the system via lowering the effective surface potentials, the measured force profiles could be accurately matched. These results suggest that modeling ionic micelles as simple hard, charged spheres may not be appropriate and that the level of deviation from such a modeling approach depends on the specific properties of each type of micelle.

3.2 Introduction

The depletion interaction has been heavily studied in various systems since the initial work of Asakura and Oosawa over a half century ago[59]. In general, a depletion force arises between two particles in solution when they approach sufficiently close to exclude any smaller, negatively adsorbed material from the gap region between them. The exclusion of the 'depletants' creates an osmotic pressure difference between the gap region and the bulk solution which results in a net attraction between the particles.

In more concentrated systems, longer-range forces, known as structural forces, are also observed. These forces arise from the ordering of depletants into layers in the gap region between particles that results from repulsion between the depletants. Structural forces are observed as oscillations between repulsive and attractive forces that increase in magnitude as the particle separation distance decreases[64].

Over the last 25 years, extensive work has been done to study both depletion and structural forces from both a theoretical and experimental stand point. Many different materials, including polyelectrolytes[19,21-26], polymers[27-28], nanoparticles[2-3,5-6,8-11,19], and rod-like[29-30] and disk-like[31-32] particles, have been used as depletants.

This work focuses on the depletion and structural forces produced by ionic micelles. The specific goal was to investigate how well these forces can be predicted using models developed (and successfully tested) for systems of hard, charged spheres. As explained in the Background section, section 3.3, preliminary experimental measurements have indicated that the depletion and structural forces produced by ionic micelles may be substantially smaller than predicted by modeling the micelles as simple charged spheres with constant properties[10,13].

Direct measurement of the force between a single colloidal particle and plate in solutions of both anionic and cationic micelles was conducted using the technique of colloidal probe atomic force microscopy (CP-AFM)[50]. The force profiles were then compared to predictions made using the model of Walz and Sharma[4] which has been previously shown to work well for low concentration of charged spheres (i.e., silica nanoparticles)[7].

3.3 Background

The initial work of Asakura and Oosawa focused on uncharged systems in which the particles and depletant material interacted as hard walls[59]. In later work, Asakura and Oosawa modeled the depletion interaction between two spherical particles in solutions of coiled chain macromolecules and charged spherical macromolecules[66]. For the latter case, an approximate solution was presented in which the depletion interaction was a function of the macromolecule concentration, charge, and solution ionic strength. A major finding of this work was that the presence of surface charge greatly enhanced the magnitude of the depletion force.

Expanding on this work, Walz and Sharma developed a model for the interaction force between two spherical particles in the presence of non-adsorbing, spherical macromolecules[4]. Using a general force balance approach, the authors were able to extend the hard sphere/ hard wall approach of Asakura and Oosawa to systems in which all components were charged. The model includes a virial expansion (to 2nd order) of the single particle distribution function to account for interactions between the depletants that become significant at higher depletant concentrations. These authors also showed that in charged systems, the magnitude and range of the depletion force can be orders-of-magnitude greater than in purely hard sphere systems.

The validity of the Walz and Sharma model was later confirmed experimentally in a model hard, charged system by Piech and Walz[7]. Using CP-AFM, Piech and Walz measured the force between a silica particle and an oxidized silicon wafer in a solution of silica nanoparticles (all components were negatively charged). For low concentrations of depletants (<1 vol.%) the authors found excellent agreement between the model predictions and their experimental results. Although the model was unable to capture the oscillatory structural forces that arise with increasing depletant concentration, the magnitude of the depletion force at these conditions was still predicted with approximate accuracy.

Several other groups have developed computational tools for predicting depletion and structural forces produced by charged depletants. Garibay-Alonso *et al*. used the Rogers-Young closure relation to solve for the structure factor in binary liquids of large uncharged particles and smaller charged particles[67]. The authors found phase separation would occur between particles in concentrated solutions of charged particles. Mendez-Alcaraz and Klein used an integral equation approach to predict the depletion force in a binary colloidal mixture [68]. Their results for charged particles showed depletion and structural forces that were both energy-driven and entropic in origin.

Trokhymchuk *et al*. derived an analytical result for the radial distribution function of two large spheres dispersed in a fluid of smaller spheres[69]. Their results yielded oscillatory interaction energy and disjoining pressure profiles that agreed well with other computer simulations. Later, these same authors used a canonical Monte Carlo method to study the ordering of sodium dodecylsulfate (SDS) micelles confined between two parallel plates[60]. They found the micelles formed layers, similar to those observed in nanoparticle solutions, when confined between the two plates. Fazelabdolabadi *et al*. employed a grand canonical Monte Carlo simulation to investigate the structural forces between charged plates created by charged nanoparticles (the results were extended to a particle-plate geometry using the Derjaguin approximation)[10]. In their approach, the nanoparticle-nanoparticle interaction was represented by a Yukawa interaction while the nanoparticle-wall interaction was modeled using a one-dimensional solution to the linear Poisson-Boltzmann equation. While the period of the structural force oscillations agreed well with the results of the CP-AFM experiments of Tulpar *et al*.[9] made using

SDS micelles as the depletant, the magnitude of the measured force was much smaller than that predicted.

Most experimental work with charged systems has focused on spherical nanoparticles as the depletant species due to their easily characterizable structure and properties. However, other charged particles can also act as depletants. With their unique properties, surfactant molecules have the ability to act as a simple electrolyte below their critical micelle concentration (cmc) or as charged depletants (i.e. micelles) above their cmc. The first observation of micelle induced depletion effects was made by Cockbain who noted the aggregation of oil particles in emulsions when soaps where added above their cmc[70].

The development of advanced experimental techniques has allowed for the direct measurement of both depletion and structural forces in micellar systems. Horn and Israelachvili published the first observation of an oscillatory force profile between two mica sheets in a solution of octamethylcyclotetrasiloxane using the surface forces apparatus (SFA)[71]. For uncharged systems, these authors determined the period of oscillation corresponded to the diameter of the solvent molecule. The first observation of long range structural forces in charged systems was obtained by Richetti and Kékicheff[12]. Using the SFA, these authors found structural forces between two mica sheets in a solution of cetyltrimethylammoniumbromide (C_{16}TAB) at concentrations above the critical micelle concentration.

Sober and Walz used total internal reflection microscopy (TIRM) to measure the interaction energy profile between a colloidal latex particle and flat plate in a C_{16}TAB solution[13]. The authors observed the onset of oscillations at higher surfactant concentrations. The magnitude of the measured depletion energy at contact was actually found to agree relatively well with potentials predicted by the Asakura and Oosawa model for purely hard spheres, leading the authors to conclude that in ionic micellar systems, ‘the effect of long range electrostatic interactions on the depletion force may be smaller than expected’.

Vlachy was able to model results similar to those seen experimentally by Sober and Walz using an integral equation technique[14]. At low concentrations (below the cmc) only a repulsive interaction was seen between macroions (large particles). At concentrations above the cmc the onset of an attractive minimum was observed, and at high concentrations (well above the cmc) structural oscillations were observed. The major drawback of Vlachy’s method was the limited size of the macroion and micelle-both had to be smaller than in previously studied experimental systems.

Using the technique of CP-AFM, Subramanian and Ducker observed oscillatory forces between a glass particle and a silica sheet in a solution of dodecyltrimethylammonium bromide (C_{12}TAB)[15]. While the focus of their work was on micelle adsorption to silica, they did note that the spacing of micelles adsorbed on the silica surface, as measured by AFM, was much different from that in the bulk solution

measured through small-angle neutron scattering (SANS) and assuming a hexagonally closed packed system.

McNamee *et al*. used CP-AFM to measure the force between two silica surfaces in solutions of sodium bis(2-ethylhexyl) sulfosucciante (NaAOT) and SDS, both anionic surfactants[16-17]. The authors observed oscillatory forces that increased in magnitude with increasing surfactant concentration and observed no effect of scan speed until the onset of the hydrodynamic force between the particle and plate. For both surfactants, they explained their results with an expansion of the Derjaguin-Landau-Verway-Overbeek (DLVO) theory that included electrostatic, van der Waals, and structural forces.

Tulpar *et al*. also used CP-AFM to study forces between a silica particle and silica plate in solutions of SDS micelles[18]. They found that the wavelength of the structural oscillations was inversely proportional to the cube root of the bulk number density of the depletants. This was in agreement with the earlier work of Piech and Walz who found the same relationship for both silica nanoparticles and negatively charged polyelectrolytes[19]. Zeng and von Klitzing also found this relationship to be true for C_{16}TAB micelles confined between a silica microsphere and an air bubble[20].

More recently, Iracki *et al*. used TIRM to measure the interaction of a silica particle with glass plate in solutions of SDS micelles near the cmc[72]. The authors found good agreement between the measured potentials and a modified Asakura-Oosawa depletion potential that also included an excluded volume term to account for electrostatic interactions. In their model, the micelle partitioning was the only adjustable parameter. The authors also note that “charged micelles are probably too “soft” to be treated as effective hard spheres”.

One of the shortcomings in most of these prior efforts in micellar system has been the lack of a direct test of our ability to correctly predict the magnitude and range of the depletion and structural forces in these systems. By comparison, various researchers have found reasonably good agreement between predicted and measured interactions using charged, spherical nanoparticles as the depletant. In the two cases where such comparisons in micellar systems have been performed (Fazelabdolabdi *et al*.[10] using SDS micelles and a grand canonical Monte Carlo simulation method, and Sober and Walz[13] using C_{16}TAB micelles and the force balance model of Walz and Sharma[4]), the magnitude of the depletion and structural forces were significantly weaker than predicted. These results suggest that the repulsive electrostatic interactions between ionic micelles or between such micelles and other charged particles or walls may be much softer than that predicted by modeling the micelle as a simple hard sphere with a net surface charge.

Our goal in this work was to perform a more comprehensive test to determine the degree to which depletion and structural forces can be predicted in micellar systems using the hard, charged sphere approach. CP-AFM was used to measure the force-vs.-

distance profiles between a relatively large silica probe particle and a silica plate in aqueous surfactant solutions below and above the cmc. The force profiles were then compared to predictions made using the Walz and Sharma model, which was previously demonstrated to be capable of accurately predicting these forces in charged nanosphere solutions at depletant concentrations of order 1 vol.% or less[7].

3.4 Experimental

3.4.1 Materials

Water was purified using a Barnstead EASYpure II water purification system (Thermo Fisher Scientific Inc., Asheville, NC, USA) equipped with a 0.22 μm final filter. Powdered myristyltrimethylammonium bromide (C_{14}TAB) (≥99%) (Sigma-Aldrich Co., St. Louis, MO, USA) and sodium dodecylsulfate (≥99%) (Sigma-Aldrich Co., St. Louis, MO, USA) were used to make micelle solutions. Note that we choose to use C_{14}TAB instead of the more common C_{16}TAB due to its similar characteristics but lower Krafft temperature. Specifically, the Krafft temperature of C_{14}TAB is below 10°C whereas that for C_{16}TAB is close to 18°C[73]. The lower Krafft temperature ensures that micelles are present in solution under all experimental conditions and that small changes in the ambient temperature will not significantly affect the measurements.

Fused silica slides measuring 63.5 mm by 25.4 mm with a thickness 3.2 mm (Technical Glass Products, Inc., Painesville Twp., OH, USA) were used for zeta-potential measurements.

Microparticles used in the AFM experiments were silica spheres, 5 μm in diameter and having a measured rms roughness of <1.0nm over 1 μm^2 (Polysciences Inc., Warrington, PA, USA). The flat plates used in the AFM experiments were polished z-cut silica single crystals (MTI Corporation, Richmond, CA, USA) that measured 10.0 mm by 10.0 mm and had a thickness of 1.0 mm. The flats had a manufacturer's stated rms roughness of <1.0 nm over 1 μm^2.

3.4.2 Solution Preparation

Micelle solutions were prepared in 30 mL polycarbonate bottles (Nalge Company, Rochester, NY, USA). When bottles were received they were cleaned with a 1% Liqui-Nox solution (Alconox, Inc., New York, NY, USA) for 2 h, rinsed with water and 200 proof ethanol, left in water for 2 h, and rinsed with water and ethanol again.

Powdered C_{14}TAB was recrystallized two times in an 80/20 solution of acetone and 200 proof ethanol. Powdered SDS was recrystallized two times in a 70/30 solution of 200 proof ethanol and water. The solution ionic strength and pH were not adjusted.

3.4.3 Zeta Potential Measurements

The zeta potential of the silica slides was determined from streaming potential measurements using a SurPASS Electrokinetic Analyzer (Anton Paar GmbH, Graz, Austria). The SurPASS tubing was rinsed using the extended rinse program instructions

with very dilute isopropanol (<1 vol.% in water) and then with deionized water; rinse cycles were approximately 5 min for each. The fused silica microscope slides were cleaned with pure ethanol, rinsed in deionized water, and cleaned for 30 min in a UV/Ozone ProCleaner (BioForce Nanosciences, Inc., Ames, IA, USA), after which the slides were rinsed with water and ethanol again. Slides were then soaked in a weak (pH < 10) potassium hydroxide (KOH) solution for 30 min to increase the surface charge before a final rinse with water.

Once clean, the slides were mounted in the SurPASS clamping cell. A 5 min rinse cycle was then run using potassium bromide (KBr) as the electrolyte for experiments using C_{14}TAB, or sodium chloride (NaCl) as the electrolyte for experiments using SDS. This gave a control measurement for the silica zeta potential. Once a control value was determined, the salt solution was flushed out of the SurPASS instrument and replaced with the micellar solution. The micellar solution was rinsed through the instrument before any measurements were taken. Each measured value was the average of four instrument passes and a minimum of two points were taken for each electrolyte or surfactant concentration. Points were taken between 30 and 60 min apart with a rinse cycle performed between each measurement.

Micellar solution concentrations were adjusted by adding known amounts of powdered C_{14}TAB or SDS to the SurPASS solution holding container, which was constantly stirred. After changing the solution concentration, the SurPASS rinse cycle was run for 5 min to thoroughly distribute the added surfactant.

Additional zeta potential measurements were performed on SiO_2 spheres (Polysciences, Warrington, PA, USA) using a Zetasizer Nano ZS (Malven Instruments Ltd., Worcestershire, UK). The SiO_2 spheres were 0.5 μm in diameter and were mixed into solutions of known concentrations of C_{14}TAB or SDS.

3.4.4 Colloid Probe Atomic Force Microscope Measurements (CP-AFM)

Deflection-distance measurements were performed with a MFP-3D AFM (Asylum Research, Santa Barbara, CA, USA). These raw measurements were converted into force-separation data using the analysis method of Ducker *et al*.[50]. Silica microparticles were attached to AFM cantilevers (ORC-8, Bruker AFM Probes, Camarillo, CA, USA) using a temperature curable epoxy (EPON 1004F Resin, Momentive, Columbus, OH, USA). The D-lever or A-lever on the ORC-8 cantilever chip was used, which had manufacturer-reported spring constant of 0.05 N/m and 0.73 N/m respectively. The spring constant for each cantilever used in the experiments was independently measured using the method of Hutter and Bechhoefer[51] and this measured value was used in the data analysis.

Prior to each experiment the silica flats were soaked in 200 proof ethanol for 2 h and then rinsed with ethanol and water. The flats where then soaked for 30 min in a weak (pH < 10) KOH solution. The flats were rinsed with water and dried with ultra high purity nitrogen before use. The silica spheres and AFM cantilevers were cleaned using

UV radiation for 15 min. The AFM fluid cell was sonicated in 200 proof ethanol for 1 h, rinsed with water, and then blown dry with nitrogen.

Approximately 20 approach and withdrawal runs were performed in each experiment and average force curves were calculated to reduce noise. Scan ranges were ~1.35 μm with a scan speed 50 nm/s (hydrodynamic forces were found to be negligible at this scan speed). At the end of each run, data was collected after the piezo stopped moving to determine the undeflected position (zero position) of the cantilever. Measurements were performed at room temperature, which was a steady 23°C.

3.4.5 Rheological Measurements

The viscosity of the surfactant solutions was measured using an Anton-Paar Physica MCR 301 rheometer (Anton Paar GmbH, Graz, Austria) with a Double-Gap system, 26.7 mm in diameter. The temperature was controlled at 23°C by a Peltier plate system that surrounded the lower cup. The upper cylinder was rotational. Viscosity was measured as a function of shear rate by an increasing torque ramp. Graphs of viscosity versus shear rate were flat over the range of 1-500 s^{-1}.

3.5 Theory

3.5.1 Model Description

A schematic of our system is shown in Figure 3-1. A charged particle of radius R is separated by distance h from a charged plate in a solution of spherical depletants, each of radius a. We assume that the interaction force between the particle and plate can be written as the sum of an electrostatic repulsion plus a depletion/structural interaction. Thus

$$F_{tot}(h)=F_{elec}(h)+F_{depl}(h) \qquad [3\text{-}1]$$

Because of strong electrostatic repulsion between the charged particle and plate, the attractive van der Waals interaction between them is ignored.

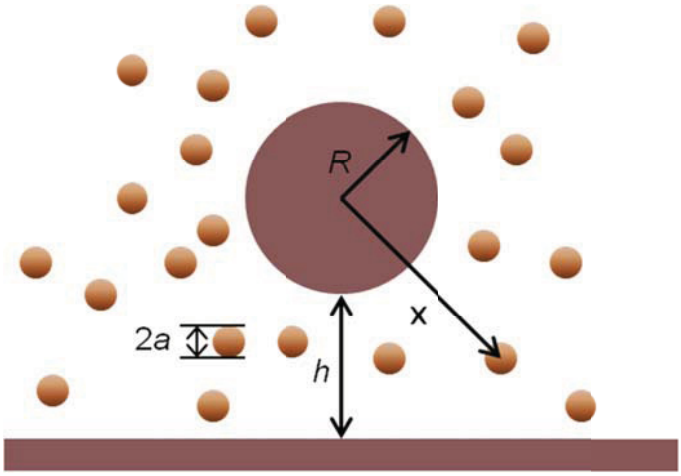

Figure 3-1. Schematic of the model system. A silica particle of radius *R* interacts with a silica plate across gap width *h*. In solution are spherical depletants of radius *a* and bulk number density ρ_∞.

The electrostatic component of Eq. [3-1] is calculated using

$$F_{elec}(h)=64\pi\varepsilon_0\varepsilon_r R\kappa\left(\frac{k_BT}{e}\right)^2\tanh^2\left(\frac{e\psi_0}{4k_BT}\right)\exp(-\kappa h) \qquad [3\text{-}2]$$

where ε_0 is the permittivity of free space, ε_r is the permittivity of the medium, k_B is the Boltzmann constant, T is the absolute temperature, e is the fundamental unit of charge, ψ_0 is the surface potential of the particle and plate (assumed to be equal as both were silica), and κ is the Debye parameter. This equation assumes superposition of potentials, which is valid for gaps larger than one Debye length, along with the Derjaguin approximation to account for curvature, which is valid for the relatively large particle used in these experiments (i.e., $R >> \kappa^{-1}$).

The depletion/structural force here was calculated using the approach of Walz and Sharma[4]. Specifically, the force exerted on the particle by the depletants (i.e., micelles) in solution was calculated as

$$\mathbf{F}_{dep}(h)=\int_{\mathbf{x}}\rho(\mathbf{x})\nabla E(\mathbf{x})d\mathbf{x} \qquad [3\text{-}3]$$

where $\rho(\mathbf{x})$ is the number density of the depletants at position $\mathbf{x}$ and $\nabla E(\mathbf{x})$ is the gradient of the interaction energy between a depletant and larger surfaces. For an isolated particle, Eq. [3-3] will result in a net force of zero due to the symmetry of the depletant distribution. Because of the plate, however, this symmetry is disrupted and a net force acting normal to the plate develops.

The interaction energy between a depletant and larger surface was calculated as the sum of a hard sphere energy plus a screened electrostatic interaction. This latter contribution was calculated using the linear superposition approach of Bell *et al.*[74]. In

general, for two spherical particles of radii a_1 and a_2, separated by center-to-center distance r, the expression of Bell *et al*. can be written as

$$E_{elec}(h)=4\pi\varepsilon_0\varepsilon_r\left(\frac{k_BT}{e}\right)Y_1Y_2\frac{a_1a_2}{r}\exp(-\kappa h) \qquad [3\text{-}4]$$

where Y_1 and Y_2 are the reduced surface potentials of the interacting surfaces. Eq. [3-4] was used as it is valid for a 1:1 electrolyte at separation distances larger than the Debye length. As stated by Bell *et al*., it is also valid for all magnitudes of surface potential and all particle sizes.

In the Walz and Sharma model, the density distribution, $\rho(\mathbf{x})$, is calculated using a 2nd order virial expansion of the single particle distribution function, meaning that two-body interactions between the depletants (likewise assumed to consist of a hard wall plus a screened Coulombic repulsion) are included. This allows the model to calculate the onset of the structural interaction, namely a long-range repulsive force, though the model is incapable of predicting the complete oscillatory structural force. Piech and Walz suggest that the model is accurate at effective depletant concentrations less than roughly 1 vol.%[7].

3.5.2 Model Parameters

The physical parameters needed to perform the model calculations are the sizes and surface potentials of both the large particle and the depletant, the volume fraction of the depletant, and the solution Debye length.

The volume fractions of the C_{14}TAB solutions were calculated based on the parameters of a cmc of 3.5 mM[75], an aggregation number N of 75[76], and a micelle radius of 3.0nm[77]. The surface potential of the micelles has been given in literature as ~+90 mV[78].

The volume fractions of the SDS solutions were calculated based on the parameters of a cmc of 8.0 mM[79] and a micelle radius of 2.0 nm[80]. The aggregation number was calculated using

$$N=\gamma_1+\gamma_2(C_{SDS})^{1/4} \qquad [3\text{-}5]$$

where γ_1 and γ_2 are the constants 16 molecules and 105 molecules/(moles/liter)$^{1/4}$, respectively, and C_{SDS} is the concentration of SDS in moles/liter[17]. The surface potential of the micelles was assumed to be -90mV[81].

The Debye parameter of the solution was calculated using

$$\kappa^2=\frac{e^2}{\varepsilon_0\varepsilon_r k_BT}\left(2\rho_{cmc}+(\rho_s-\rho_{cmc})(\beta)\right) \qquad [3\text{-}6]$$

where ρ_s is the surfactant concentration and ρ_{cmc} is the cmc[82] in units of molecules per unit volume and β is the fraction of ionized surfactant molecules in the micelle. In this equation, the ionic strength of the solution is determined solely by the free ions (i.e., no screening by the micelles themselves, which is discussed further in the Discussion section, section 3.7). These ions come from surfactant molecules, assumed to be at the cmc concentration, and the free counter ions that are released into solution by the

partially ionized micelles. For C_{14}TAB, we used a partial ionization value β of 0.25[83], while a value of 0.2 was used for SDS[17].

The surface potentials of the silica particle and plate were determined using the SurPASS streaming potential instrument described in the Experimental section 3.4 (we assume the surface potentials to be equal to the measured zeta potentials). Zeta potential measurements for silica in solutions with and without C_{14}TAB were made at multiple concentrations. Without any C_{14}TAB in solution, the zeta potential of the silica surfaces was -90 mV. (A background of 1.75 mM KBr was used as the electrolyte). Upon the addition of C_{14}TAB, the zeta potential of the silica increased from -90 mV to +90 mV. This increase is caused by the adsorption of the positively charged $C_{14}TA^+$ ions to the negatively charged silica. The increase in zeta potential was observed below the cmc (0.5 cmc) and increasing the C_{14}TAB concentration above the cmc did not further increase the zeta potential. Further tests performed on SiO_2 spheres in solutions of varying concentrations of C_{14}TAB below and above the cmc also produced measured zeta potentials of +90 mV. Similar charge reversal was also observed by Lüderitz *et al*. for the adsorption of C_{16}TAB on to silica[84]. Based on these results, we assume the silica surfaces in our CP-AFM experiments with C_{14}TAB have a surface potential of +90mV.

Similarly, streaming potential measurements with and without SDS were also performed. Using a background of 4 mM NaCl, a zeta potential value of -90 mV was obtained for the silica surfaces at a neutral pH. When 4mM SDS was used in the solution, the zeta potential of the SiO_2 surfaces was reduced in magnitude to ~-40mV. Further increasing the SDS concentration continued this reduction, such that for 5, 10, and 20 cmc SDS solutions the measured zeta potential was -20 mV. This reduction in the zeta potential of the silica in SDS solutions can be attributed to the decrease in the solution pH upon the addition of SDS. The measured pH of the 5, 10, and 20 cmc SDS solutions ranged from 3.8-3.4, decreasing with increasing surfactant concentration. Comparing our results with previous results of Herman and Walz[85] for the zeta potential of bare silica at varying pHs, we find good agreement with their reported values. Specifically, Herman and Walz report the zeta potential to be -20 mV for 1 μm silica spheres in this pH range. We therefore model the silica surfaces in SDS solutions as having surface potentials equal to the zeta potentials reported by these authors.

3.6 Results

Plots of force versus separation distance for the interaction of a 5 μm silica sphere with a flat silica plate at various C_{14}TAB and SDS concentrations are shown in Figure 3-2 and Figure 3-3, respectively. (For each of these plots and in all remaining figures, the effects of virtual deflection have been removed. Details on the procedure used for this correction are given in Appendix A.) The plots clearly show that with increasing volume fraction the magnitude and number of oscillations in the force profile increases. Also, with increasing concentration, the location of the primary depletion

attraction and the point where repulsive electrostatic forces begin to dominate the depletion interactions shift closer to contact.

For C_{14}TAB, the onset of a depletion attraction (minimum in the force curve) is observed at 5 cmc and a long-range repulsive barrier is first observed at 10 cmc. Similarly, for SDS a repulsive barrier and depletion attraction are observed at 5 cmc while the curves at 10 and 20 cmc both display oscillatory force profiles and a jump-in feature. This jump-in occurs due to instabilities that arise from the use of weak spring constant cantilevers. Both the approach and withdraw curves are plotted for 10 and 20 cmc SDS to display the entire force profile as it is not symmetric upon approach and withdraw due to this jump-in feature.

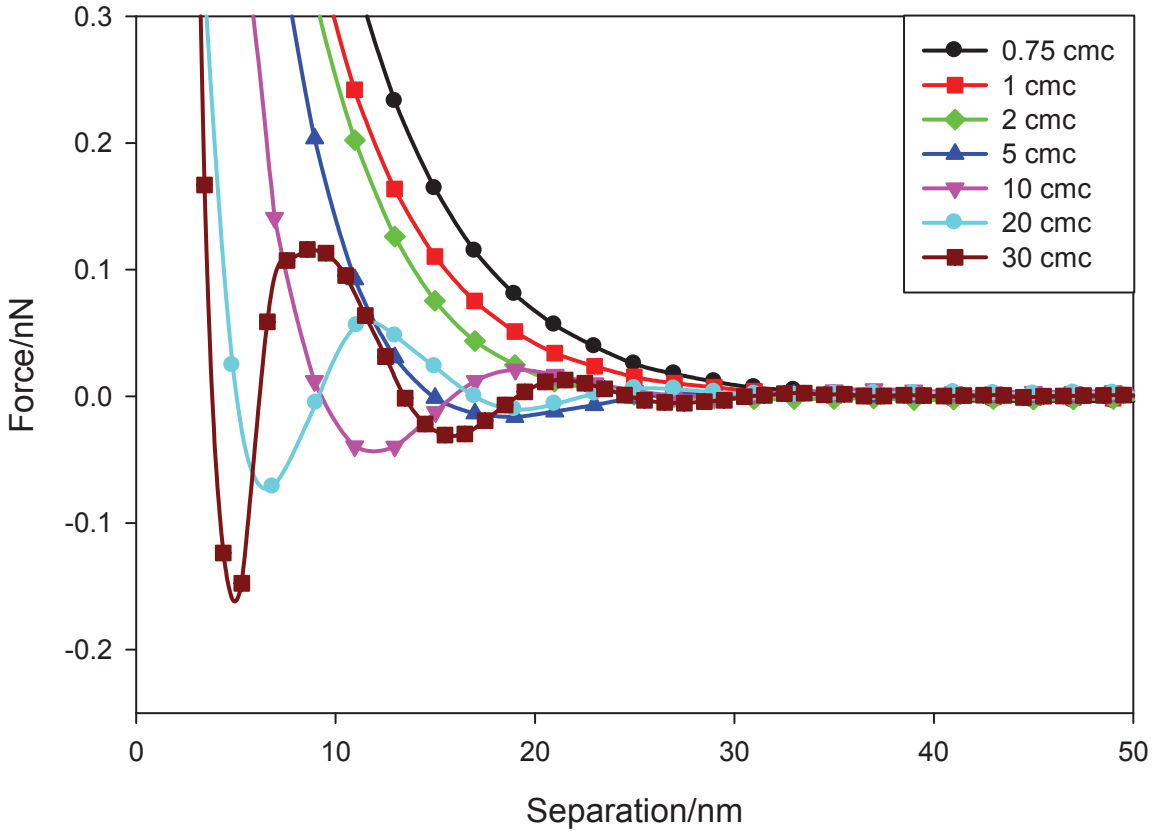

Figure 3-2. Plots of the measured force profiles between a 5 μm silica sphere and a flat plate in solutions of C_{14}TAB at varying concentrations. From low to high concentration the development of a depletion attraction and then structural forces can be observed. (Note: The lines through the measured data are simply to help guide the eye.)

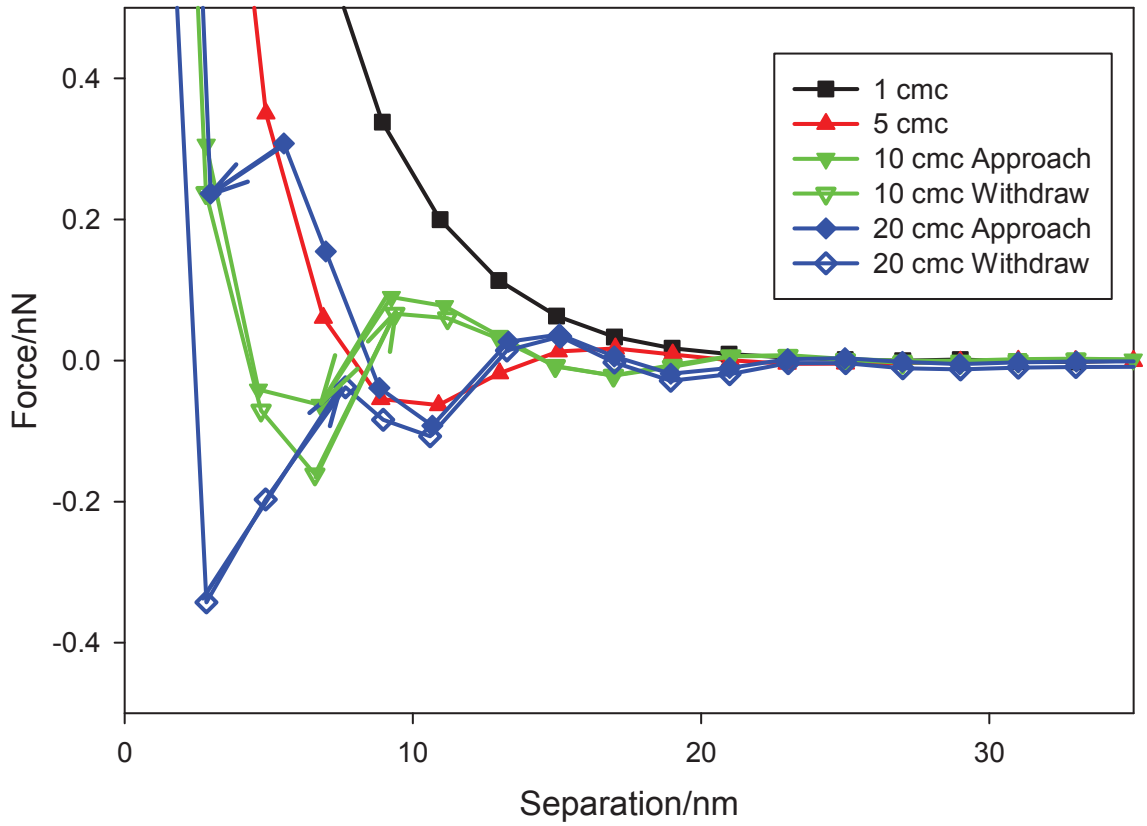

Figure 3-3. Plots of the measured force profiles between a 5 μm silica sphere and a flat plate in solutions of SDS at varying concentrations. From low to high concentration the development of a depletion attraction and then structural forces can be observed. The arrows represent unstable jump-in features. (Note: The lines through the measured data are simply to help guide the eye.)

In Figure 3-4 and Figure 3-5, we have separated each C_{14}TAB and SDS curve above 5 cmc into its own plot and added onto it the results from the Walz and Sharma model for a hard, charged depletant. The varying model parameters used in each case are listed in Table 3-1. (We focus on the data above 5 cmc as these measurements show a clearly resolvable depletion force.)

Concentration/Parameter	5 cmc	10 cmc	20 cmc	30 cmc
C_{14}TAB Volume Fraction	0.0127	0.0286	0.0604	0.0921
C_{14}TAB Debye Length (nm)	4.22	3.54	2.81	2.40
C_{14}TAB Zeta Potential (mV)	+90	+90	+90	+90
SDS Volume Fraction	0.010	0.020	0.037	--
SDS Debye Length (nm)	2.9	2.5	2.0	--
SDS Zeta Potential (mV)	-90	-90	-90	--

Table 3-1. Parameters used in model calculations of the depletion force.

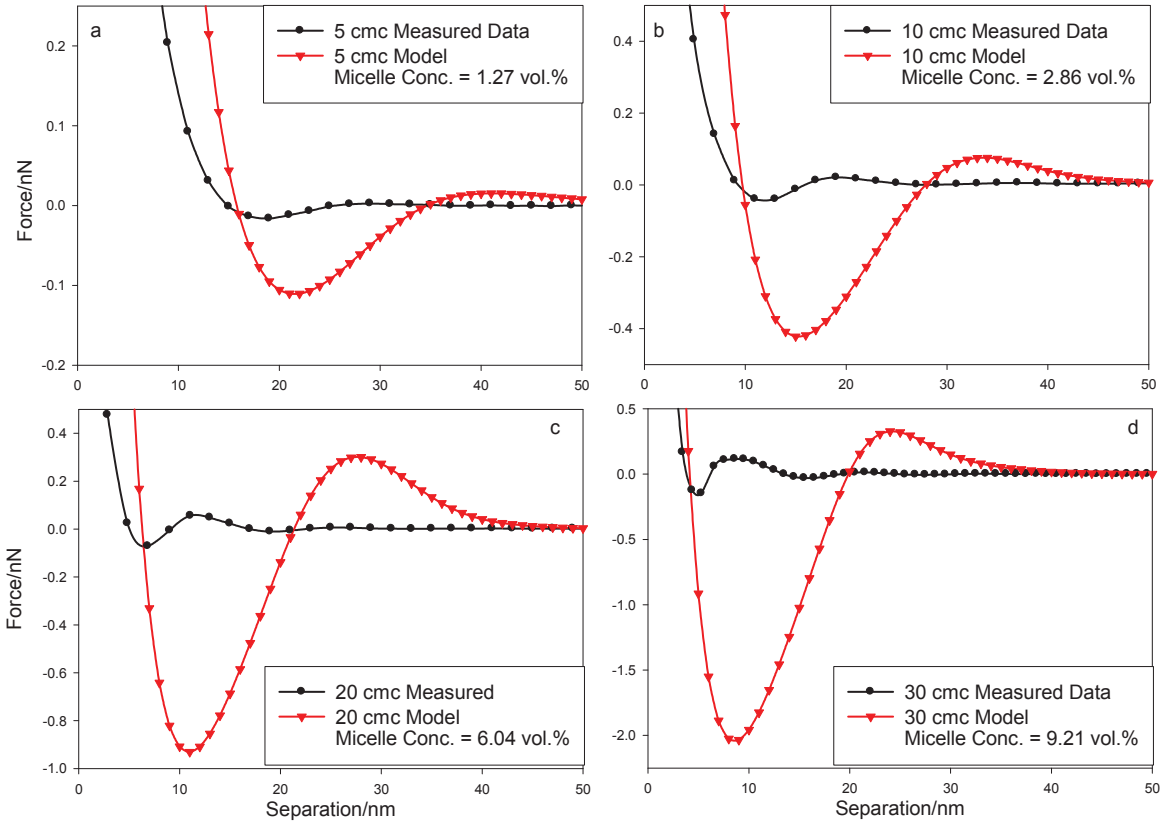

Figure 3-4. Plots showing both the measured and predicted force profiles at C_{14}TAB concentrations of (a) 5 cmc, (b) 10 cmc, (c) 20 cmc, and (d) 30 cmc. Discrepancies can clearly be seen in the magnitude of the modeled curves versus the measured data. An offset is also observed in the location of the maximum attractive force.

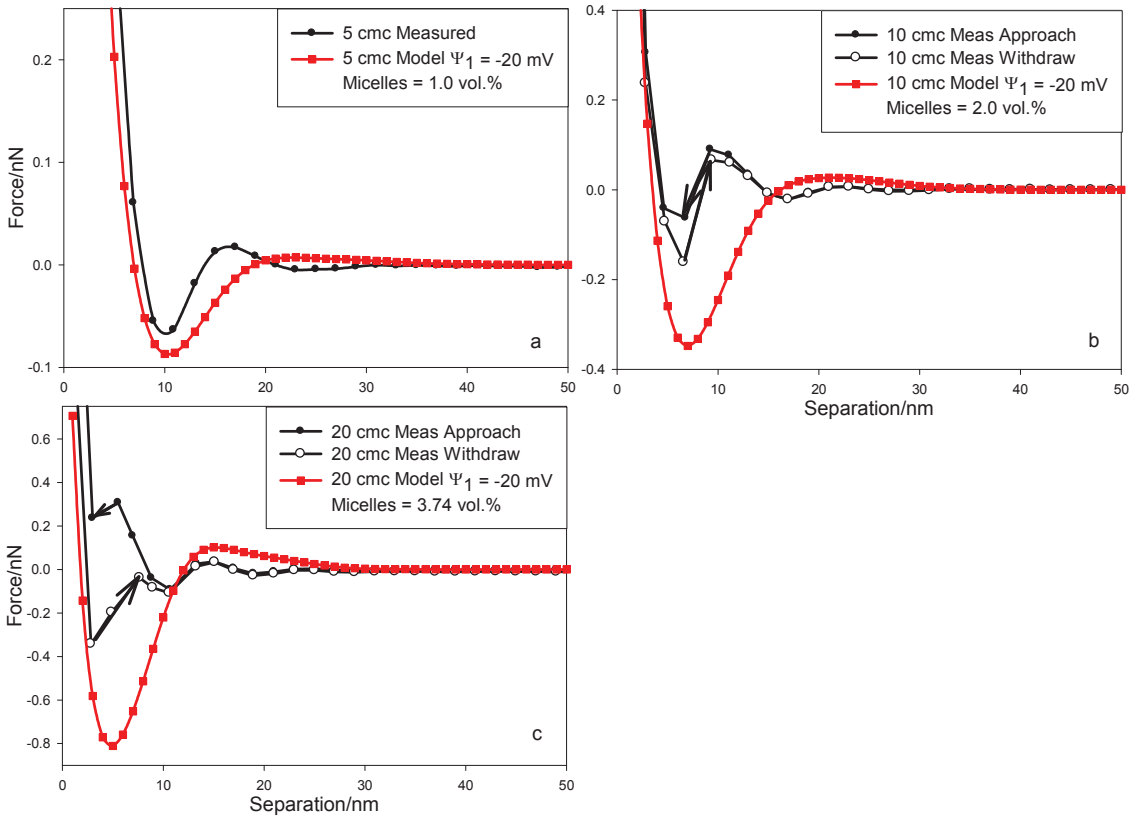

Figure 3-5. Plots showing both the measured and predicted force profiles at SDS at concentrations of (a) 5 cmc, (b) 10 cmc, and (c) 20 cmc. Variation can clearly be seen in the magnitude of the modeled curves versus the measured data. No offset is observed in the location of the maximum attractive force.

As can be seen in the plots of Figure 3-4, there are key differences between the measured results for C_{14}TAB and those predicted by the Walz and Sharma model. First, the magnitude of the maximum attractive force (i.e., lowest point in the curve) is significantly smaller in magnitude than that predicted by the model. Second, the positions of the minima and maxima in the force profile do not align.

For SDS, shown in Figure 3-5, similar deviations are also observed from the Walz and Sharma model. While the magnitude of the maximum attractive force is similarly overpredicted, the deviation is smaller than that observed with C_{14}TAB. Conversely, the location of the maximum attractive force observed with SDS does appear correct.

The observed experimental versus model deviation for both surfactants will be discussed in greater detail in the Discussion section 3.7.

3.7 Discussion

We have shown that the measured interaction between a SiO_2 microparticle and flat SiO_2 plate in ionic micellar solutions of C_{14}TAB and SDS do not agree with predicted results of the Walz and Sharma[4] model for the depletion interaction produced by hard,

charged spheres. For both surfactants the measured interaction is significantly weaker than that predicted. These findings agree qualitatively with the previous findings of both Sober and Walz[13] and Fazelabdolabadi *et al*.[10] We should again emphasize that the force profiles, obtained in the CP-AFM experiments with silica nanospheres by Piech and Walz[7] at depletant volume fractions similar to those listed in Table 3-1, showed good agreement with the Walz and Sharma model, suggesting that the discrepancy observed here is related to the model representation of the micelles.

In attempting to determine possible causes of the observed discrepancies, we considered the following three possible explanations:

(1) errors in the physical parameters characterizing the micelles,
(2) errors in the Debye length characterizing the range of the electrostatic interactions in the system, and
(3) errors in the magnitude of the electrostatic interaction between the micelles and surfaces or between the micelles themselves.

We discuss each of these in greater detail in the following sections.

3.7.1 Errors in the Physical Properties of the Micelles

Most of the model systems parameters for the micelles were taken from literature, while other required values were measured independently. The specific micelle properties needed were the micelle size, volume fraction, and surface potential. The SiO_2 surface potentials were determined by independent zeta potential measurements as described previously in the Experimental section, section 3.4.

To determine whether errors in the properties of the micelles could cause the deviations observed above, we performed a series of model simulations where the properties were allowed to vary by ±10%. Our feeling was that because these two surfactants, especially SDS, have been studied in great detail, their properties (i.e., cmc, size, aggregation number) are likely known within this level of uncertainty. In addition, as will be shown, the resulting changes in the force profiles were far from sufficient to explain the observed discrepancy.

As an example of how a small change in the physical properties would affect the predicted results, we present in Figure 3-6 graphs showing the effect of increasing and decreasing the diameter of the C_{14}TAB micelle by 0.5 nm (approximately 10% from the reported value of 6 nm). We chose the micelle diameter as the parameter to adjust as it has the largest effect on the micelle volume fraction and, therefore, on the predicted force curves.

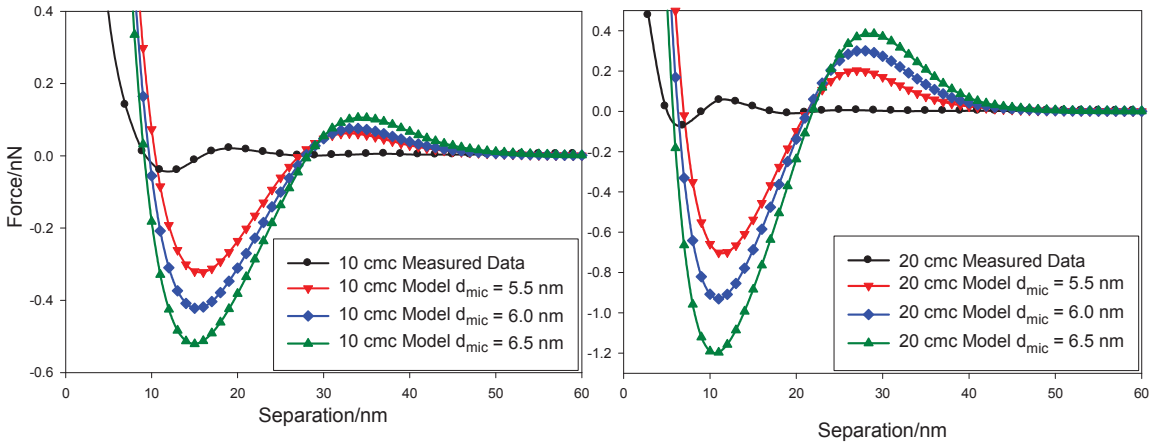

Figure 3-6. Plots of force versus separation for 10 and 20 cmc C_{14}TAB solutions. The model curves were produced using micelle diameters of 5.5, 6.0, and 6.5 nm. The deviation between the measured data and the model prediction is still not accounted for with the reduced micelle diameter.

As seen, while reducing the micelle diameter by 10% slightly improves the agreement, the model-predicted magnitude of the minimum and maximum force are still roughly an order-of-magnitude too large. (Note that we do not show the data for 5 and 30 cmc, however, the trends are the same.) Similar findings were made for variations in the micelle aggregation number; however, due to the smaller effect on the micelle volume fraction, the improvement between the model and predicted results was even smaller when changing this parameter. These results lead us to believe that deviations in the micelle properties are likely not the cause of the deviations observed between the measured and model results.

3.7.2 Errors in the System Debye Length

The second possible source of error considered was a deviation in the system Debye length. In this work, the assumption has been made that only free ions (i.e. those not bound to or incorporated into micelles) contribute to the Debye length. Previous studies have also shown this to be true for systems of C_{16}TAB [12,82] and SDS[86]. In each of these previous works, the authors measured the electrostatic interaction between mica surfaces in micellar solutions using the surfaces forces apparatus (SFA). Each set of authors concluded that below the cmc micellar solutions behave similar to completely dissociated ionic solutions, while above the cmc the micelles and their "bound counterions" do not contribute to the decay length of the electrostatic interaction.

Because the predicted depletion and structural interactions were significantly weaker than measured, matching the measured results required lowering the Debye length in the model. The Debye length for the 10 and 20 cmc C_{14}TAB solutions calculated using Eq. [3-6], which assumes no micelle screening, were 3.54 and 2.81 nm, respectively. Shown in Figure 3-7 are the results obtained by reducing each of these Debye lengths by a factor of approximately two-thirds. As seen, even with this

substantial reduction, the magnitude of the measured attractive force is still smaller than predicted. In addition, the location of this predicted maximum attraction in the 10 cmc system has now moved closer to contact than that measured.

Our feeling is that these results indicate that errors in the screening length are likely not the cause of the discrepancy between the predicted and measured force profiles observed in Figure 3-4. This issue is further reviewed later in the Discussion section 3.7.

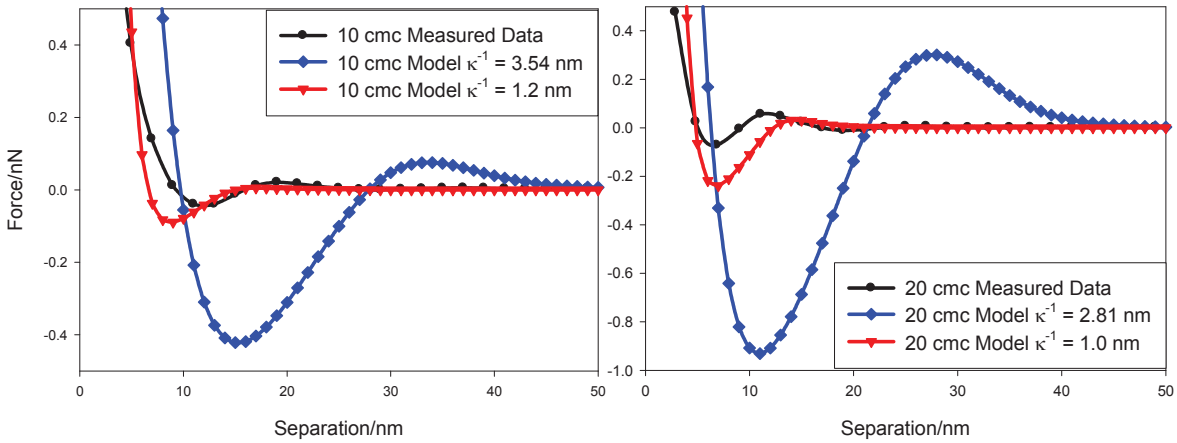

Figure 3-7. Plots of force versus separation for 10 and 20 cmc C_{14}TAB solutions. The red model curves (inverted triangles) were produced using a shorter Debye length than that predicted by Eq. [3-6]. Using these smaller Debye lengths does not account for the deviation between the measured data and model prediction.

3.7.3 Errors in the Nature of the Micelle-Surface or Micelle-Micelle Interaction

The final possible explanation considered for the discrepancy between the measured and predicted results is error in the predicted electrostatic interaction between the micelles and surfaces, or between the micelles themselves. These interactions are key parameters in predicting the depletion and structural forces using Eq. [3-3]. Specifically, the much weaker-than-predicted depletion and structural forces shown Figure 3-4 and Figure 3-5 compared to those predicted could arise if the electrostatic repulsive interactions between the various components, given by Eq. [3-4], was weaker than expected.

One possibility, for example, is that the charges on the micelle rearrange in response to an electric field to minimize the interaction. Previous studies by Miklavic *et al*.[87] and Rouzina and Bloomfield[88] have shown that when surfaces with mobile charge groups interact, they will always do so in a way that minimizes their interactions. Miklavic *et al*. studied this effect by modeling the interaction of two heterogeneous surfaces at constant charge or constant potential. They found that when surface charges were free to migrate the resulting force was always attractive. Rouzina and

Bloomfield found that macroions in solutions of multivalent electrolytes could attract each other by correlating their counterion environments.

A second, and perhaps more likely, possibility is that the micelle shape is distorted in response to the electric field created by another micelle or a charged surface, or by the viscous forces arising from the motion of the particle toward or away from the plate. (Finite deformability is clearly one significant difference between micelles and hard spheres.) Though very little work exists on this topic, if such deformation did occur, it could cause the electrostatic interactions to appear softer (i.e. weaker) than those predicted for hard spheres. It would also imply that the electrostatic interactions are specific to each type of surfactant and that the interactions could not be predicted *a priori*.

As further evidence that the interaction between the micelles may be weaker than predicted, we present rheological data on solutions of 20 cmc C_{14}TAB and compare this to data obtained with a solution of 6 nm silica nanoparticles (NexSil 6® solution, Nyacol Nanotechnologies, Inc. Ashland, MA, USA) at equal volume fractions and ionic strengths. In dispersions of charged particles, the solution viscosity is primarily a function of the particle volume fraction and the strength of the electrostatic repulsion between the particles[89]. This latter parameter is determined by the solution Debye length and the magnitude of the electrostatic surface potentials.

As seen in the viscosity results given in Table 3-2, even though the magnitude of the surface potential of the micelles (~+90 mV) is significantly greater than that of the silica nanoparticles (~-50 to -60 mV), the effect of the nanoparticles on increasing the solution viscosity (relative to that of pure water) is approximately four times that of the micelles at equal volume fractions and ionic strength. Although not a completely conclusive test, these differences do suggest that the effective repulsion between the micelles is weaker than expected based simply on the magnitude of their surface potential.

Also included in Table 3-2 is the viscosity result for a 20 cmc SDS solutions. As can be seen from the table, the viscosity of 20 cmc SDS is higher than that for 20 cmc C_{14}TAB. This result is counterintuitive, as SDS at a concentration of 20 cmc has a smaller volume fraction and higher ionic strength than 20 cmc C_{14}TAB, both of which would suggest a lower viscosity in the SDS solution. This result indicates that the electrostatic interactions between micelles vary based on individual surfactant molecules and micelle structure.

The conclusion that electrostatic interactions are individual to surfactants is further supported by the measured viscosity of an equal volume fraction tetradecyltrimethylammonium chloride solution (C_{14}TACl) also presented in Table 3-2. The viscosity of the C_{14}TACl solution is equal to that of the C_{14}TAB solution, indicating that the electrostatic interactions for micelles formed from C_{14}TA+ surfactants are

similar for the different counterions. (Note the small difference in ionic strength is due to the difference in cmc between C_{14}TACl and C_{14}TAB.)

It should be noted that the shear rate range of the measured viscosity data falls within the values present in the AFM system. For the system described, the maximum shear rate ranges from 3.5 to 309 s^{-1} for separation distances of 100 to 5 nm. This is well within the experimental range described in section 3.4.5.

Particle Type and Concentration	Ionic Strength, mol/L	Viscosity, Pa·s
C_{14}TAB 20 cmc (6.02 vol.%)	$11.7x10^{-3}$	$1.13x10^{-3}$
NexSil 6 6.02 vol.%	$11.7x10^{-3}$	$1.60x10^{-3}$
SDS 20 cmc (3.7 vol.%)	$22.9x10^{-3}$	$1.35x10^{-3}$
C_{14}TACl (6.02 vol.%)	$13.3x10^{-3}$	$1.13x10^{-3}$

Table 3-2. Comparison of the viscosity of a 20 cmc C_{14}TAB solution to a solution of 6 nm silica nanoparticles (NexSil 6®) at equal volume fractions and ionic strengths. Comparisons are also made with 20 cmc SDS and 20 cmc C_{14}TACl.

Incorporating a rigorous model for predicting the micellar interactions that includes the effect of charge rearrangement and/or deformation would clearly not be trivial and is beyond the scope of this work. As a simple alternative, we instead simulated this effect by lowering the effective surface potential of the micelles and any surfactant coated surfaces (i.e., weakening the electrostatic repulsion). Our procedure was to determine the effective surface potential that matched the magnitude of the maximum attractive force in the measured force profiles. As discussed previously, Piech and Walz[7] found that the Walz and Sharma[4] model was able to accurately predict the magnitude of the maximum attraction in systems of silica nanopspheres as the depletant, even at increasing nanosphere concentrations. In addition, using the maximum attractive force avoids any problems arising from errors in the measured separation distance, which are frequently an issue with CP-AFM experiments.

Note that we chose to reduce the surface potential of both the micelles and the SiO_2 surfaces in the case of C_{14}TAB. Due to the opposite charge of the C_{14}TA+ surfactant molecules and the SiO_2 surfaces, the SiO_2 surfaces will become coated in a bilayer or bilayer-like coating of C_{14}TA+ molecules[15]. We have thus assumed that the surfactant-coated surfaces will behave similarly to that of the micelles with respect to charge mobility and/or deformation. We should note that we clearly recognize that because of the vast differences in curvature, along with the fact that the bilayers are adsorbed onto a solid surface, this is a significant assumption. However, assuming that

the surface potential of the probe particle and plate remain unchanged (i.e., adjusting only the micelle surface potential) simply alters the resulting effective surface potential of the micelle needed to fit the maximum attractive force (i.e, the force curves can still be fit).

At the same time, for the SDS system, because we have no clear evidence of SDS adsorption onto the silica probe particle or plate, we only adjust the effective potential of the micelles. Our basis for lack of SDS adsorption comes from two experimental observations. First, the zeta potentials measured on silica particles in the presence of SDS agree with those Herman and Walz for pure silica[85]. Second, we have also obtained images of silica plates in solutions containing either C_{14}TAB or SDS surfactant using atomic force microscopy. With C_{14}TAB, there were clear changes in the surface features of the silica slide in the presence of the surfactant, indicating adsorption. With SDS, however, no such changes could be detected. We do note that there is some evidence of SDS adsorption onto silica nanoparticles from the work of Ahualli *et al*.[90]. In this work, the authors observed supercharging of the silica from SDS; however, no indication of supercharging was observed in our measurements.

The results of this matching exercise are shown in Figure 3-8 and Figure 3-9, and the resulting effective potentials are listed in Table 3-3. As seen, with increasing surfactant concentration, the effective surface potential needed to match the maximum attraction decreases. This trend is consistent with an increasing degree of micelle-micelle interactions at these higher surfactant concentrations.

It should be mentioned that with the SDS system, the jump-in feature, observed in the 10 and 20 cmc curves made fitting the magnitude of the maximum attraction somewhat difficult, as the actual value of this maximum force was not completely clear. Our approach used in these cases was to match the maximum attractive force to the measured force at the jump-out point on the withdraw curve. This procedure results in a model curve with the largest expected maximum attractive force, which serves as an upper bound for the effective micelle surface potential.

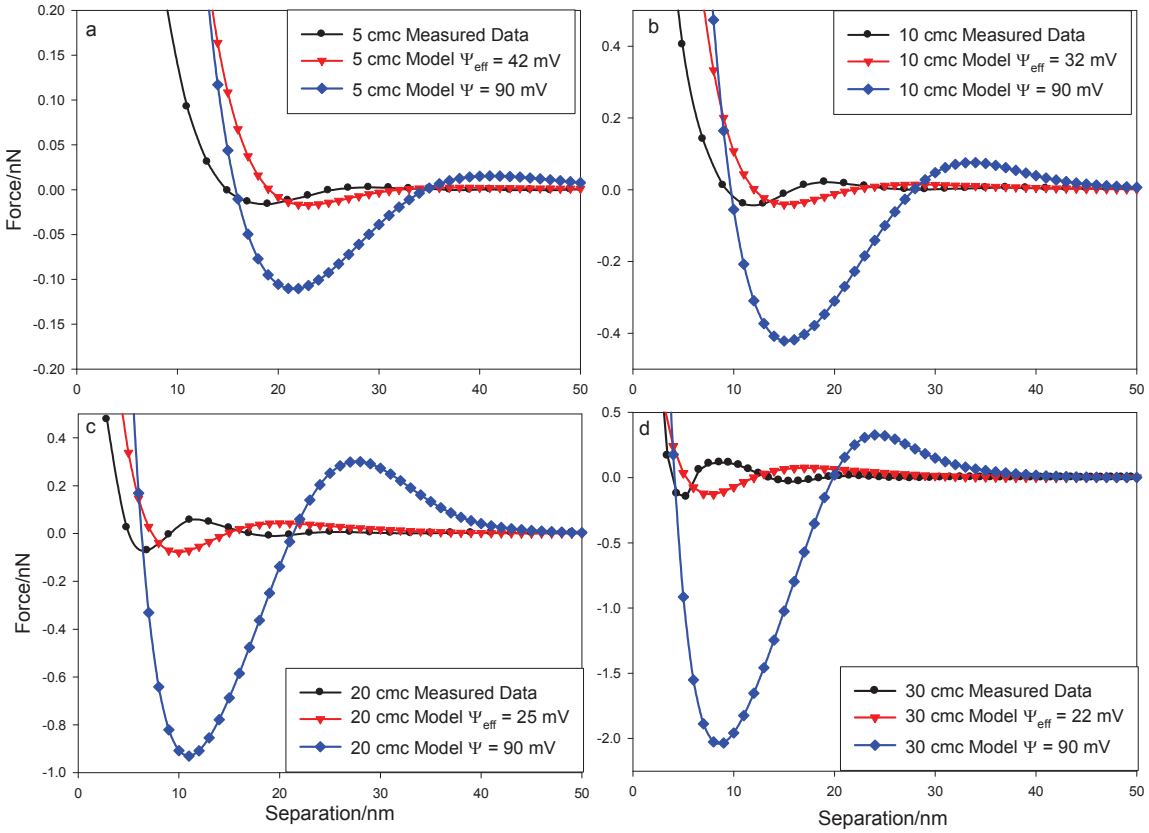

Figure 3-8. Plots of force vs. separation distance for C_{14}TAB solutions at (a) 5 cmc, (b) 10 cmc, (c) 20 cmc, and (d) 30 cmc using effective surface potentials in the charged, hard sphere model.

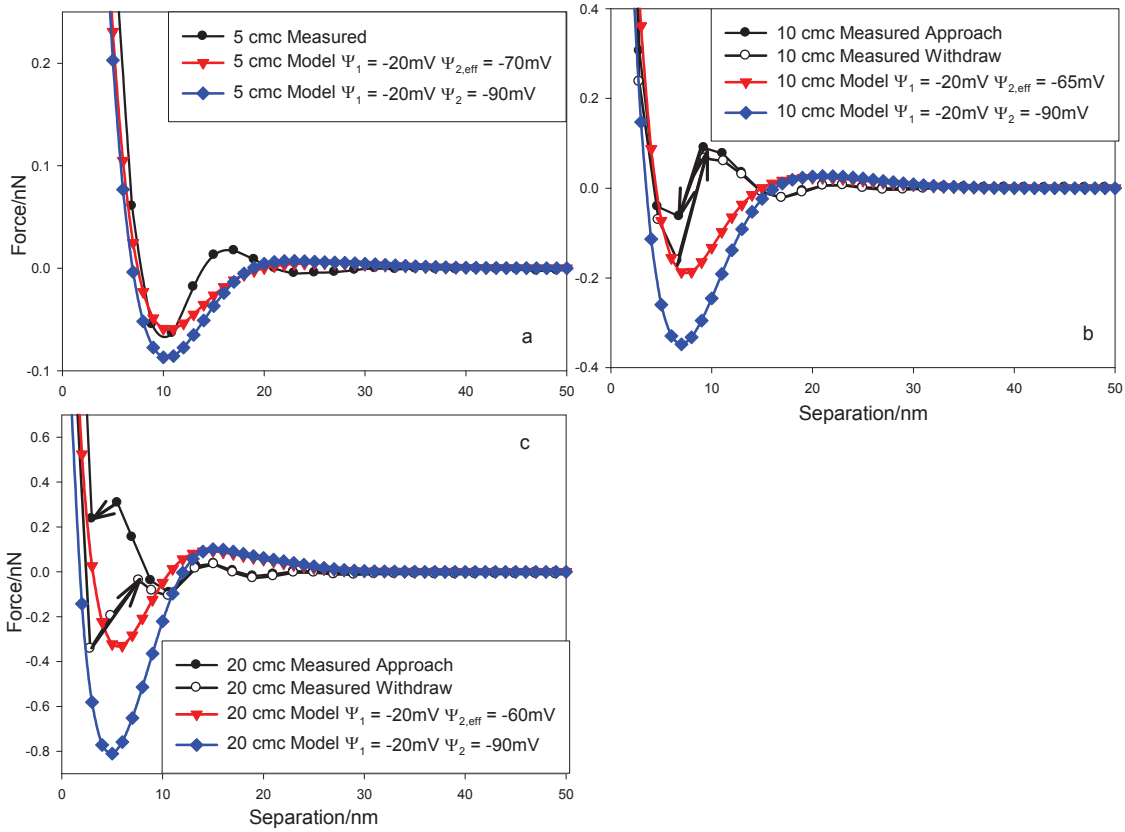

Figure 3-9. Plots of force vs. separation distance for for SDS solutions at (a) 5 cmc, (b) 10 cmc, and (c) 20 cmc using effective surface potentials in the charged, hard sphere model.

C_{14}TAB Concentration	Ψ_{eff}	SDS Concentration	Ψ_{eff}
5 cmc	42 mV	5 cmc	-70 mV
10 cmc	32 mV	10 cmc	-65 mV
20 cmc	25 mV	20 cmc	-60 mV
30 cmc	22 mV		

Table 3-3. Effective surface potential, Ψ_{eff}, needed to match the measured magnitude of the maximum attractive force.

As seen in Figure 3-8, lowering the effective surface potentials in the C_{14}TAB solution not only allows matching the magnitude of the maximum attraction, but the magnitude of the longer-range repulsive maximum is more closely predicted as well.

One noticeable remaining error in these plots, however, is that the location of the measured minima in the C_{14}TAB profiles (i.e., position of maximum attraction) is consistently smaller (i.e., closer to contact) than that predicted. We attribute this difference not to model error but rather to the weak cantilever (ORC-8 D-Lever) used in these experiments. Due to the large electrostatic repulsion between the large sphere and plate, it is likely that the cantilever experiences an effective constant compliance

region before actual hard contact. Similar finding have also been made for other low spring constant cantilevers by Piech and Walz[7] and Lüderitz and von Klitzing[84].

As evidence that this offset is due to the weak cantilever used in these experiments, we present data taken with a higher spring constant cantilever (ORC-8 A-Lever, nominal spring constant of 0.73 N/m). Figure 3-10 is a plot of force versus separation distance for 0.5 and 0.75 cmc C_{14}TAB solutions. As can be seen from the figure, a new jump-to-contact feature is observed (identified by the arrows on the figure). This jump is a result of the attraction between the layers of C_{14}TAB that coat both SiO_2 surfaces. In measurements using weaker cantilevers, this jump is not observed, ostensibly because the cantilever is not capable of overcoming the strong electrostatic repulsion between the surfaces.

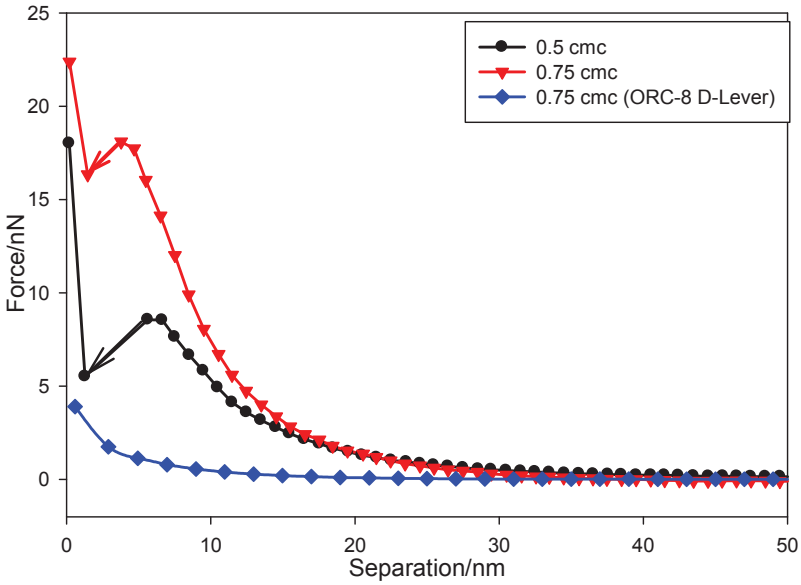

Figure 3-10. Plot of force versus separation distance for 0.5 and 0.75 cmc C_{14}TAB solutions using an ORC-8 A-Lever cantilever (nominal spring constant = 0.73 N/m). A jump-to-contact is observed that is not present in measurements with the weaker spring constant cantilevers (blue diamonds).

This inability to obtain true contact between the particle and plate would cause the separation distances for the measured force profiles to be lower than actual. To adjust for this error, we shift the measured results by an offset, δ, that aligns the location of the maximum attractive force in the results shown in Figure 3-8.

Table 3-4 lists the values for δ at each C_{14}TAB concentration. Note that δ decreases with increasing C_{14}TAB concentration. This result is physically consistent with the decrease in the system Debye length which would shorten the range of the electrostatic force between the large particle and the flat plate.

Concentration	δ/nm
5 cmc	4.25
10 cmc	3.0
20 cmc	2.5
30 cmc	1.0

Table 3-4. Offset, δ, values for the distance of shift of the measured data to align the primary depletion well.

The need for this offset also explains why the force measured with the weaker spring constant at 0.75 cmc in Figure 3-10 (blue diamonds) appears so much weaker than that measured with the higher spring constant (red inverted triangles). The problem is not with the measured forces but is instead with the separation distances measured with the weaker cantilever. In this system, the force curve obtained with the weaker spring needs to be shifted outward by roughly 13 nm to match that measured with the stiffer spring. This higher value of δ compared to the values listed in Table 3-4 arises from the fact that the ionic strengths used in the solutions for the results in Figure 3-10 were substantially lower than those used in Table 3-4, and the resulting stronger electrostatic repulsive force led to larger errors in the measured separation distance.

Figure 3-11 replots those figures shown in Figure 3-8 with the offset δ applied to the measured data. As seen, the model is now capable of capturing quite accurately the short range shape of the measured C_{14}TAB force profiles. It is also clear that the shape of the curve in the region dominated by the electrostatic repulsion between the particle and plate (i.e., region closest to contact) is matched quite well, especially in the 5, 10 and 20 cmc systems. This agreement further supports the claim that the micelles are not contributing to the screening of the electrostatic forces in the system, as such screening would cause deviations in this part of the force profile.

This correction to the separation distance for the measured C_{14}TAB results was not necessary for the SDS results as the measured and predicted location of the maximum attractive force were in agreement. Because SDS reduced the micellar solution pH and therefore the SiO_2 surface potentials, the electrostatic repulsion between the probe particle and plate in these systems was weaker and thus true hard contact between the surfaces was likely achieved.

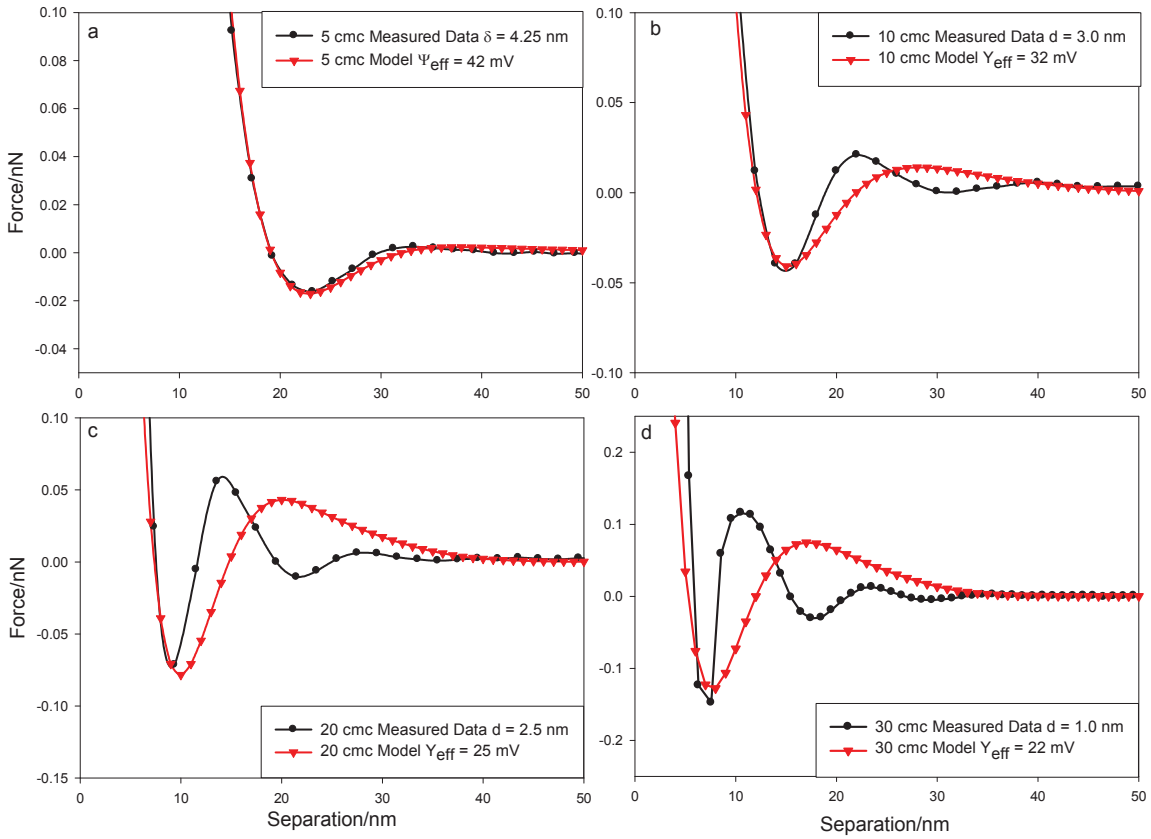

Figure 3-11. Plots of force vs. separation in (a) 5 cmc, (b) 10 cmc, (c) 20 cmc, and (d) 30 cmc C_{14}TAB solutions. Adjustment has been made to the separation distance of the measured data to align the minimum of the primary depletion well with the modeled primary deletion well.

Finally, it is clear that errors still remain in the long range component of the force profiles, specifically in the location of the first repulsive barrier and in the lack of oscillations in the predicted force (i.e., the structural force). As discussed earlier in the Background section, section 3.3, this discrepancy arises from the fact that the Walz and Sharma model uses only an approximate correction to account for the multi-body interactions between the micelles, which are the cause of these oscillations. Very similar disagreements were also obtained by Piech and Walz[7] in experiments using silica nanoparticles as the depletant.

As an example, shown in Figure 3-12 are two graphs taken from Piech and Walz which shows the model-vs.-experiment comparison of two different nanoparticle volume fractions. As seen, while the magnitude of the maximum attractive force was closely matched at both concentrations, there are clear deviations in the long-range portion of the graph. Furthermore, the nature of these deviations is very similar to those seen in Figure 3-9 and Figure 3-11 for the micelle systems. An important difference, however, is that no adjustment of the surface potential was necessary with the silica nanoparticle

system, which supports our claim that treating the micelles as simple hard, charged spheres is not appropriate.

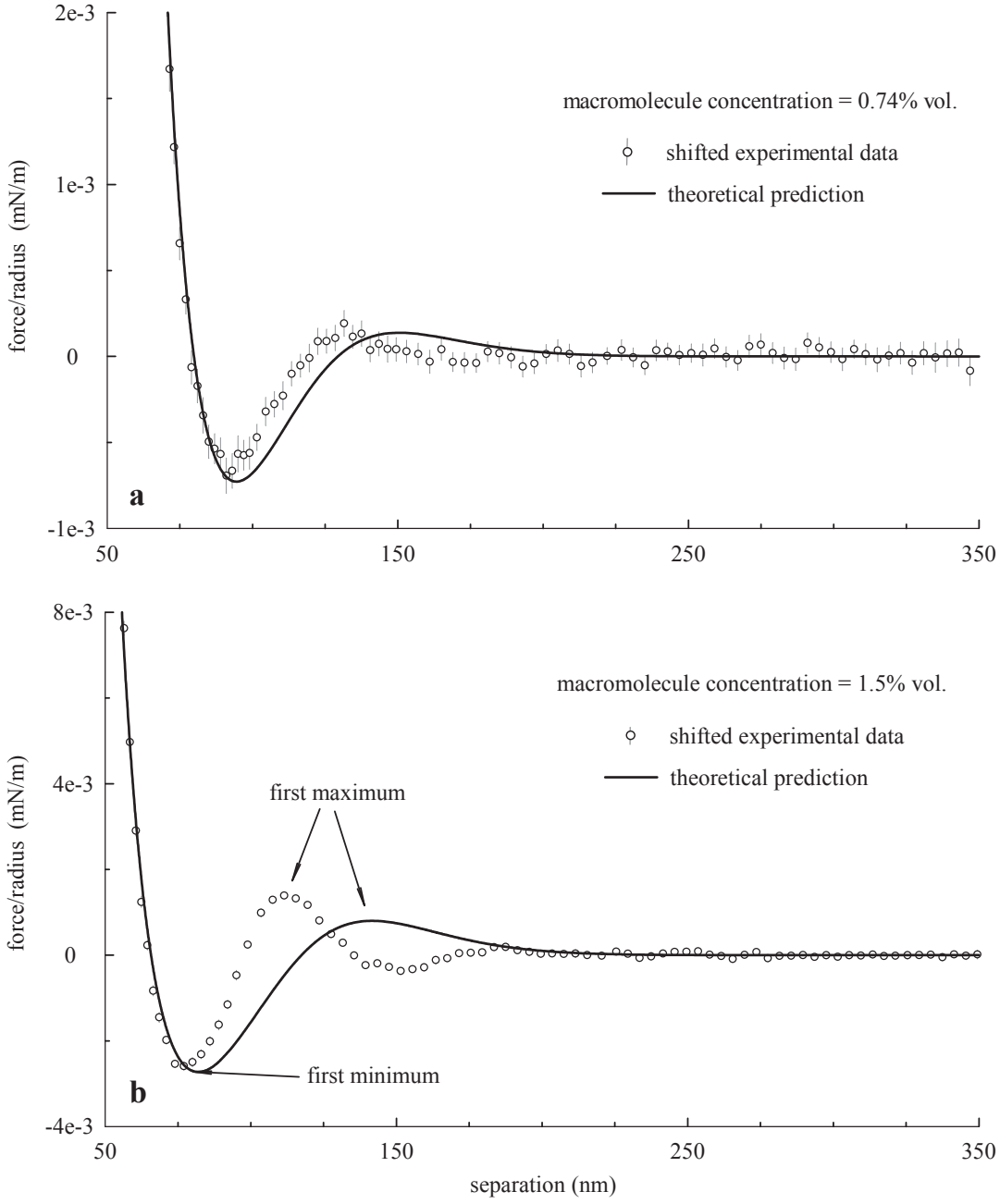

Figure 3-12. Force/radius versus separation curves for a silica microparticle interacting with a silicon oxide wafer in a solution of silica nanoparticles (Ludox TMA ®). Good agreement with model predictions is seen for low concentrations of nanoparticles. At higher concentrations the model properly predicts the magnitude of the attractive maximum but not the range of the interaction. Reproduced from Peich and Walz[7].

3.8 Conclusions

Measurements of the depletion force on a silica sphere moving normally toward a silica plate in solutions of C_{14}TAB and SDS micelles show a significant deviation from the forces predicted by modeling the components as charged, hard spheres with a known and constant surface potential. Specifically, the magnitude of the force was vastly over predicted using the model of Walz and Sharma[4]. Possible errors in the physical properties of the micelles and contributions of the micelles to screening of the electrostatic repulsive interactions in the system were considered as possible sources of the deviation; however the degree of adjustment in the relevant properties needed to match the measured force curves made these explanations unlikely. By reducing the surface potential of the micelles in the model, simulating weaker micelle-micelle and micelle-surface electrostatic interactions, it was possible to closely match the magnitude of the maximum attractive force. The resulting comparison between measured and predicted force profiles closely mirrors that obtained using charged silica nanospheres as the depletant. In the latter systems, however, no adjustment of the measured surface potential was required.

These results, coupled with viscosity measurements in both micellar and charged nanoparticles solutions, leads us to conclude that modeling the ionic micelles as simple hard, charged spheres may not be appropriate. However, the cause of this deviation is not known. Two possible mechanisms suggested here are rearrangement of mobile charge groups or physical deformation of the micelles in an external electric field. This latter possibility, physical deformation, would clearly be consistent with the results presented here, as such deformation would not occur with true hard, charged spheres, would also reduce the effect of the micelles on increasing the solution viscosity, and would vary with the inherent elasticity of each type of micelle.

Chapter 4 Investigation of the Stability Properties of Colloidal Dispersions in Ionic Micellar Solutions

The work described in this chapter has been accepted for publication in the Journal of Colloids and Interface Science. Reprinted with permission, Elsevier 2013.

4.1 Abstract

The effects of ionic micelles (C_{14}TAB and SDS) on the stability of a dispersion of highly charged silica particles was investigated both visually and using UV-vis absorption. As the surfactant concentration increased from 0 to 30 cmc, a clear critical flocculation concentration was observed with both surfactants. For SDS, restabilization was observed at 20 cmc. These stability results were compared to energy profiles that were calculated using measured force profiles between a single silica sphere and plate obtained with colloid-probe atomic force microscopy. It was found that flocculation would occur once the energy well formed by depletion attraction exceeded 3 k_BT, while restabilization occurred once the long range structural energy barrier exceeded 8 k_BT. These values are consistent with the energy levels needed for flocculation and restabilization predicted by other researchers.

4.2 Introduction

The stability properties of colloidal suspensions can be affected by depletion interactions through what is known as depletion flocculation. The depletion interaction and higher order structural interactions that affect colloidal stability have been thoroughly studied as discussed in Chapter 3 sections 3.2 and 3.3.

Depletion flocculation was first reported in the early 20th century when Traube observed the creaming of natural rubbers[1]. Since that time, the ability of negatively adsorbing materials to induce flocculation of larger particles has been well studied[91-96]. In particular, Sharma *et al*.[97], Cowell *et al*.[98], and Sperry *et al*.[99] investigated the critical flocculation and restabilization concentrations of varying colloidal dispersions. Restabilization, sometimes referred to as depletion stabilization, occurs when a colloidal dispersion remains stable at high concentrations of depletant due to repulsive structural forces between the particles arising from ordering of the depletant in the gap region.

As discussed in Chapter 3, micelles offer a unique type of negatively adsorbing material which can be used to induce depletion flocculation. Because micelles are only present above their critical micelle concentration (cmc), it is possible to effectively remove the depletant material (i.e. micelles) from the system by simple dilution.

Several authors have previously shown that micelles can act as flocculants in colloidal systems as a result of depletion interactions. Cockbain showed that oil particles could be aggregated in emulsions using soaps above their cmc[70]. Aronson also showed that emulsions of paraffin oil could be destabilized by anionic and nonionic micelles[100]. Ma presented findings on the stability behavior of polystyrene particles in varying concentrations of Triton X-100, a nonionic surfactant[101]. Flocculation of the polystyrene particles was observed at higher surfactant concentrations.

More recently, Furusawa *et al*. studied the flocculation behavior of dispersions of latex particles in both anionic and cationic surfactants using rheology[102]. These authors observed a maximum in the viscosity of the dispersion with increasing surfactant concentration, indicating the development of depletion flocculation at intermediate surfactant concentrations and then restabilization at higher concentrations. They found the flocculation to be fully reversible through simple dilution.

Iracki *et al*. studied the 2D colloidal configurations of silica particles in solutions sodium dodecylsulfate[72]. Agreement was found between video microscopy measurements and Monte-Carlo simulations for the ordering of the particles. Lüderitz *et al*. studied the interaction between a silica sphere and silicon wafer and a silica sphere and silica plate is a solution of hexadecyltrimethylammonium bromide (C_{16}TAB) micelles[84]. The authors observed that the interaction varied between the different surfaces and concluded that silica and silicon surfaces have differing aggregate morphologies.

Much of the previous work on micelle induced depletion flocculation has simply focused on its occurrence (i.e., does flocculation occur and at what conditions). In the

present work, we will compare observed phase behavior to the stability predicted using force profiles measured between a single particle and a plate obtained with the technique of colloid-probe atomic force microscopy. Our system consists of silica (SiO_2) particles and micelles of the common surfactants tetradecyltrimethylammonium bromide (C_{14}TAB) and sodium dodecylsulfate (SDS). The stability of suspensions of micron-size SiO_2 particles is measured using both UV-vis absorption measurements and simple visual observation.

4.3 Theory

4.3.1 Flocculation and Restabilization Theory

Consider two charged colloidal particles interacting in a solution containing a negatively adsorbed species, such as ionic micelles. As the particles approach, a number of interactions can arise. At the simplest level, repulsive electrostatic and attractive van der Waals forces comprise the well-known DLVO forces. However, the presence of the micelles makes the picture more complicated. At short distances, the micelles will be excluded from the gap region and an attractive depletion force can arise. At sufficiently high micelle concentrations, ordering of the micelles in the gap region will lead to longer-range, oscillatory, structural forces.

To predict the stability of a dispersion of such particles, we typically evaluate the pair interaction energy profile, $E(h)$, which is related to the force profile, $F(h)$, as

$$F(h) = -\frac{dE(h)}{dh}. \qquad [4\text{-}1]$$

If the charge on the particles is sufficiently large, such that flocculation in the near-contact primary energy well created by strong van der Waals forces is unlikely, then the stability of the dispersion will be controlled by the relative strengths of the depletion and structural interactions. We can then represent the essential components of the energy profile as shown in Figure 4-1. Here the energy well is created by the interplay between the repulsive electrostatic interaction and the attractive depletion interaction, while the longer-range barrier represents the short range component of the structural interaction.

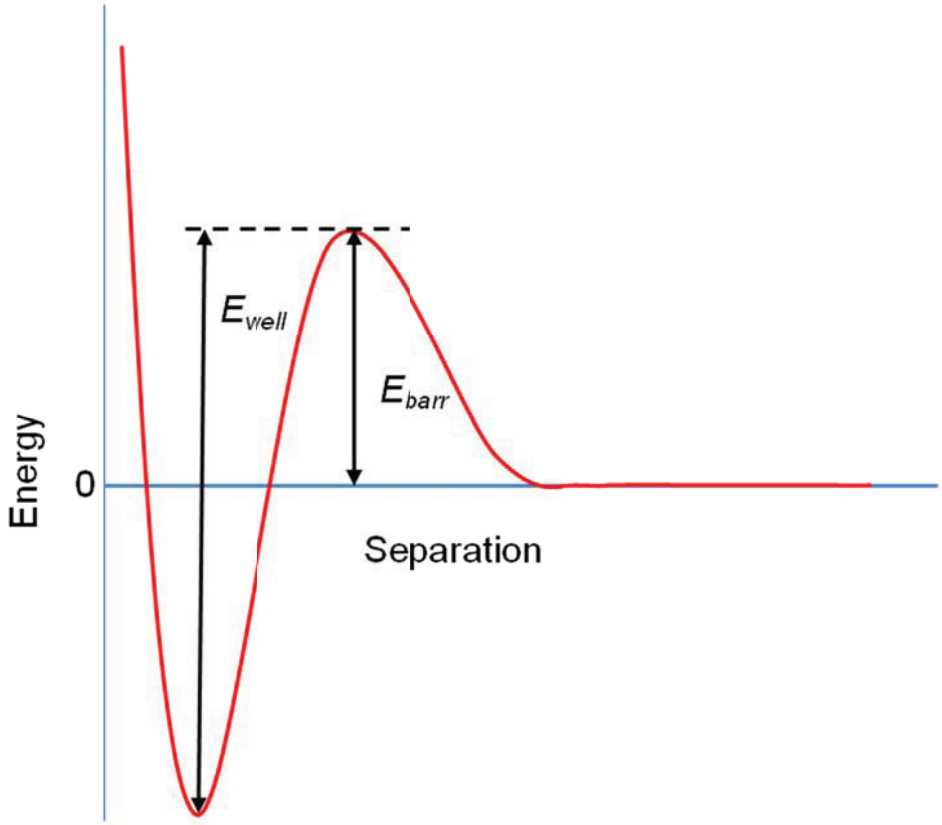

Figure 4-1. Schematic representation of the interaction of two particles in a dispersion containing a smaller depletant species.

The two primary determinants of stability in this system will be the depth of the secondary energy well, E_{well}, and the height of the long range energy barrier, E_{barr}. Previous work has shown that the stability of the system can be predicted using these two variables[97,103].

For low concentrations of depletants, both E_{well} and E_{barr} are small and the electrostatic force between the dispersed particles will be sufficient to maintain stability. As the concentration of depletants increases, E_{well} initially increases faster than E_{barr} because the latter parameter is a 2nd order concentration effect. That is to say, the depth of E_{well} is dependent upon depletant interactions with the larger species, and E_{barr} is dependent upon depletant-depletant interactions. At low concentrations, depletant-depletant interactions will be infrequent, and therefore, E_{barr} will be small. With increasing concentration, however, depletant-depletant interactions will increase and E_{barr} will eventually grow faster than E_{well}.

Once E_{well} becomes sufficiently larger, flocculation occurs (termed the critical flocculation concentration). At even higher depletant concentrations, E_{barr} increases to the point that the particles will not have sufficient energy to overcome it and stability is re-established. The point is termed the critical restablization concentration.

4.3.2 UV-vis Absorption Theory

UV-vis spectroscopy can be used as a means to quantify the flocculation behavior of a colloid dispersion. The total absorbance from a colloidal dispersion can be related to the wavelength of incident light through the simple power law expression

$$A=k\lambda^{n}, \qquad [4\text{-}2]$$

where A is the absorbance, k is a constant dependent upon particle size, density, and refractive index, λ is the wavelength of light, and n is the turbidity exponent which is a function of particle size[104].

Eq. [4-2] arises from the theory of Rayleigh scattering which describes the relationship between the intensity of scattered light and wavelength for systems where particle size is much smaller than the wavelength of incident light. For Rayleigh scattering, intensity scales as λ^{-4}. In our experiments, where the particle size is on the order of the wavelength of light used, the turbidity exponent will increase with increasing particle size. Therefore, flocculation behavior can be quantified as an increase in the turbidity exponent over time, which can be determined from the slope of a log-log plot of total absorbance versus wavelength. That is

$$\log A = \log k + n \log \lambda \qquad [4\text{-}3]$$

4.4 Experimental

4.4.1 Materials

Water was purified using a Barnstead EASYpure II water purification system (Thermo Fisher Scientific Inc., Asheville, NC, USA) equipped with a 0.22 μm final filter. Powdered myristyltrimethylammonium bromide (C_{14}TAB) (≥99%) (Sigma-Aldrich Co., St. Louis, MO, USA) and sodium dodecylsulfate (≥99%) (Sigma-Aldrich Co., St. Louis, MO, USA) were used to make micelle solutions. Note, similar to Chapter 3, we chose to use C_{14}TAB instead of the more common C_{16}TAB due to its similar characteristics but lower Krafft temperature. Specifically, the Krafft temperature of C_{14}TAB is below 10°C whereas that for C_{16}TAB is close to 18°C[73]. The lower Krafft temperature ensured that micelles are present in solution under all experimental conditions and that small changes in the ambient temperature will not significantly affect the measurements.

Microparticles used in the AFM experiments were silica spheres, 5 μm in diameter and having a measured rms roughness of <1.0nm over 1 μm^2 (Polysciences Inc., Warrington, PA, USA). The flat plates used in the AFM experiments were polished z-cut silica single crystals (MTI Corporation, Richmond, CA, USA) that measured 10.0 mm by 10.0 mm and had a thickness of 1.0 mm. The flats had a manufacturer's stated rms roughness of <1.0 nm over 1 μm^2. Microparticles used in flocculation experiments were silica spheres, 0.5 μm in diameter (Polysciences Inc., Warrington, PA, USA).

4.4.2 Solution Preparation

Micelle solutions were prepared in 30 mL polycarbonate bottles (Nalge Company, Rochester, NY, USA). When bottles were received they were cleaned with a 1% Liqui-Nox solution (Alconox, Inc., New York, NY, USA) for 2 h, rinsed with water and 200 proof ethanol, left in water for 2 h, and rinsed with water and ethanol again.

Powdered C_{14}TAB was recrystallized two times in an 80/20 solution of acetone and 200 proof ethanol. The solution ionic strength was not adjusted. Powdered SDS was recrystallized two times in a 70/30 solution of 200 proof ethanol and water. The solution ionic strength and pH were not adjusted.

4.4.3 AFM Measurements

Deflection-distance measurements were performed with a MFP-3D AFM (Asylum Research, Santa Barbara, CA, USA). These raw measurements were converted into force-separation data using the analysis method of Ducker *et al*.[50]. Silica microparticles were attached to AFM cantilevers (ORC-8, Bruker AFM Probes, Camarillo, CA, USA) using a temperature curable epoxy (EPON 1004F Resin, Momentive, Columbus, OH, USA). The D-lever on the ORC-8 cantilever chip was used, which had a manufacturer-reported spring constant of 0.05 N/m. The spring constant for each cantilever used in the experiments was independently measured using the method of Hutter and Bechhoefer[51] and this measured value was used in the data analysis.

Prior to each experiment the silica flats were soaked in 200 proof ethanol for 2 h and then rinsed with ethanol and water. The flats where then soaked for 30 min in a weak (pH < 10) KOH solution. The flats were rinsed with water and dried with ultrahigh purity nitrogen before use. The silica spheres and AFM cantilevers were cleaned using UV radiation for 15 min. The AFM fluid cell was sonicated in 200 proof ethanol for 1 h, rinsed with water and then blown dry with nitrogen.

Approximately 20 approach and withdrawal runs were performed in each experiment and average force curves were calculated to reduce noise. Scan ranges were ~1.35 μm with a scan speed 50 nm/s (hydrodynamic forces were found to be negligible at this scan speed). At the end of each run, data was collected after the piezo stopped moving to determine the undeflected position (zero position) of the cantilever. Measurements were performed at room temperature, which was a steady 23°C.

4.4.4 UV-vis Spectroscopy Measurements

UV-vis absorption data was taken using an Agilent 8453 UV-vis Spectrometer (Agilent Technologies, Santa Clara, CA, USA). The instrument was allowed a 1 h warm-up time before a blank sample was taken. Time between sample measurements varied between 3 and 5 min, with total sample duration ranging from 60-120 min. A wavelength range of 700-900 nm was used in the experiments.

Poly(methyl methacrylate) (PPMA) cuvettes (VWR, Radnor, PA, USA) were used for all samples. Microparticle concentrations in each sample were 0.1 vol.%

Microparticles were added to each cuvette just before measurements were started. Cuvettes were gently inverted three times to evenly distribute the microparticles before being inserted into the spectrometer.

4.5 Results and Discussion

4.5.1 AFM Force Measurements

Figure 4-2 and Figure 4-3 present AFM force curves for the interaction of a 5 μm diameter silica microparticle and a flat silica plate in varying concentrations of C_{14}TAB and SDS, respectively. (For each of these plots and in all remaining figures, the effects of virtual deflection have been removed. The procedure for this is discussed in Appendix A.) The plots clearly show that with increasing volume fraction the magnitude and number of oscillations in the force profile increases. Also, with increasing concentration, the location of the primary depletion attraction and the point where repulsive electrostatic forces begin to dominate the depletion interactions shifts closer to contact due to the increase in ionic strength.

For C_{14}TAB, the onset of a depletion attraction (minimum in the force curve) is observed at 5 cmc and a long-range depletion repulsion is first observed at 10 cmc. Similarly, for SDS a depletion repulsion and depletion attraction are observed at 5 cmc while the curves at 10 and 20 cmc both display oscillatory force profiles and a jump-in feature. This jump-in phenomenon, which was also observed in the CP-AFM experiments of Tulpar *et al*.[18] with SDS micelles, is an instability that arises from the use of low spring constant cantilevers. Both the approach and withdraw curves are plotted for 10 and 20 cmc SDS to display the entire force profile as it is not symmetric upon approach and withdraw due to this jump-in feature.

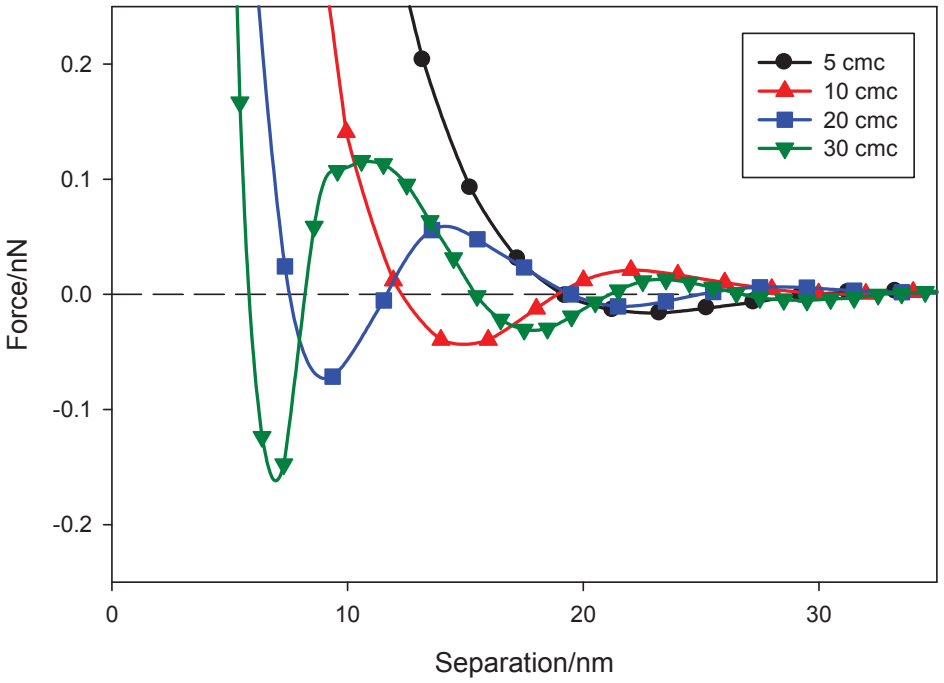

Figure 4-2. Force versus separation plot for the interaction of a 5 μm silica particle with a flat plate in varying solutions of C_{14}TAB. (Note: Lines through the measured data are simply to help guide the eye.)

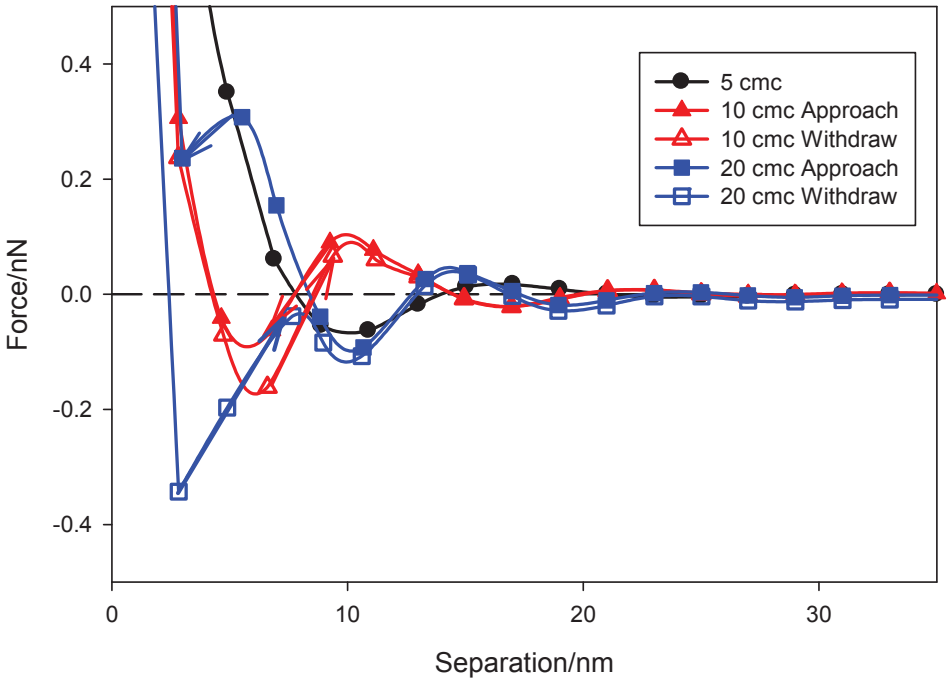

Figure 4-3. Force versus separation plot for the interaction of a 5 μm silica particle with a flat plate in varying solutions of SDS. (Note: Lines through the measured data are simply to help guide the eye.)

The Derjaguin approximation is used to convert the measured force curves in Figure 4-2 and Figure 4-3 from sphere-plate interactions to sphere-sphere interactions (i.e., the interaction between a sphere and identical plate is twice that between two identical spheres). The measured force is then scaled by the particle radius to account for the different particle sizes used between the AFM and UV-vis measurements. Finally, the resulting force curves were fit by a spline function in MATLAB® and then integrated to produce interaction energy versus separation distance curves.

For the case of SDS a "combined curve" is used for the spline fitting and integration to account for the non-uniformity between the approach and withdraw curves. For these combined curves, the approach curve was used for long-range separations down to the jump-in point on the approach curve. This jump-in point was then connected to the jump-out point on the withdraw curve. The withdraw curve was then used for the remaining points to contact (i.e. zero separation). Creating combined curves by this method captured the full depth of the primary depletion attraction and full height of the depletion repulsive barrier in the force curves. These combined curves are shown in Figure 4-4.

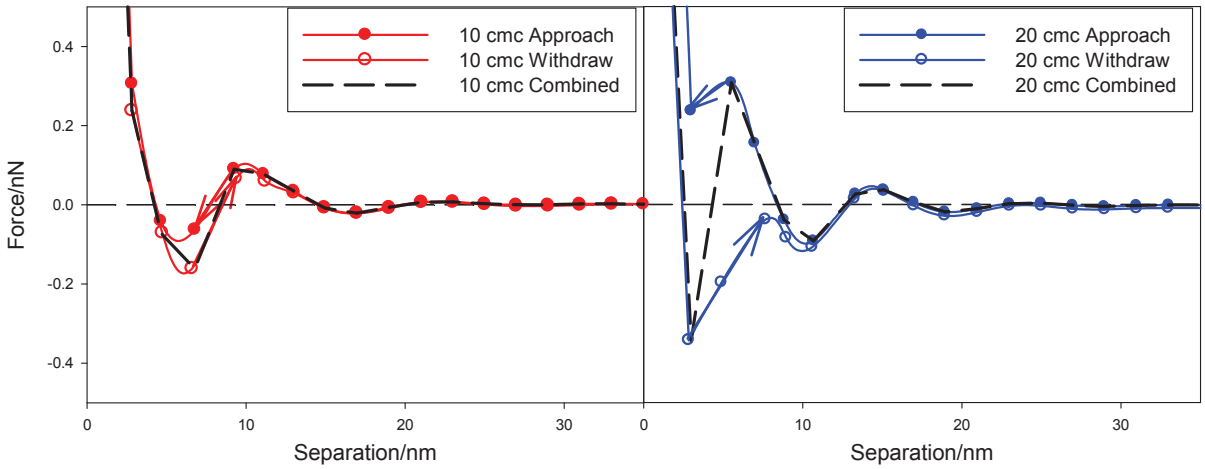

Figure 4-4. Force versus separation plots showing the combined curves used for spline fitting the interaction of a 5 µm silica particle and a flat plate. The combined curve is needed due to the lack of symmetry between the approach and withdraw curves.

Figure 4-5 and Figure 4-6 show interaction energy versus separation curves for the interaction of two 0.5 µm diameter silica spheres in varying micellar solutions. Correlating with Figure 4-2 and Figure 4-3, an increase is observed in the height of the repulsive energy barrier and depth of the depletion energy well with increasing concentration. Table 4-1 summarizes the depletion energy well depths and repulsive energy barrier heights for each system. An example of how E_{well} and E_{barr} are calculated is shown in the 10 cmc plot of Figure 4-5 (upper right plot).

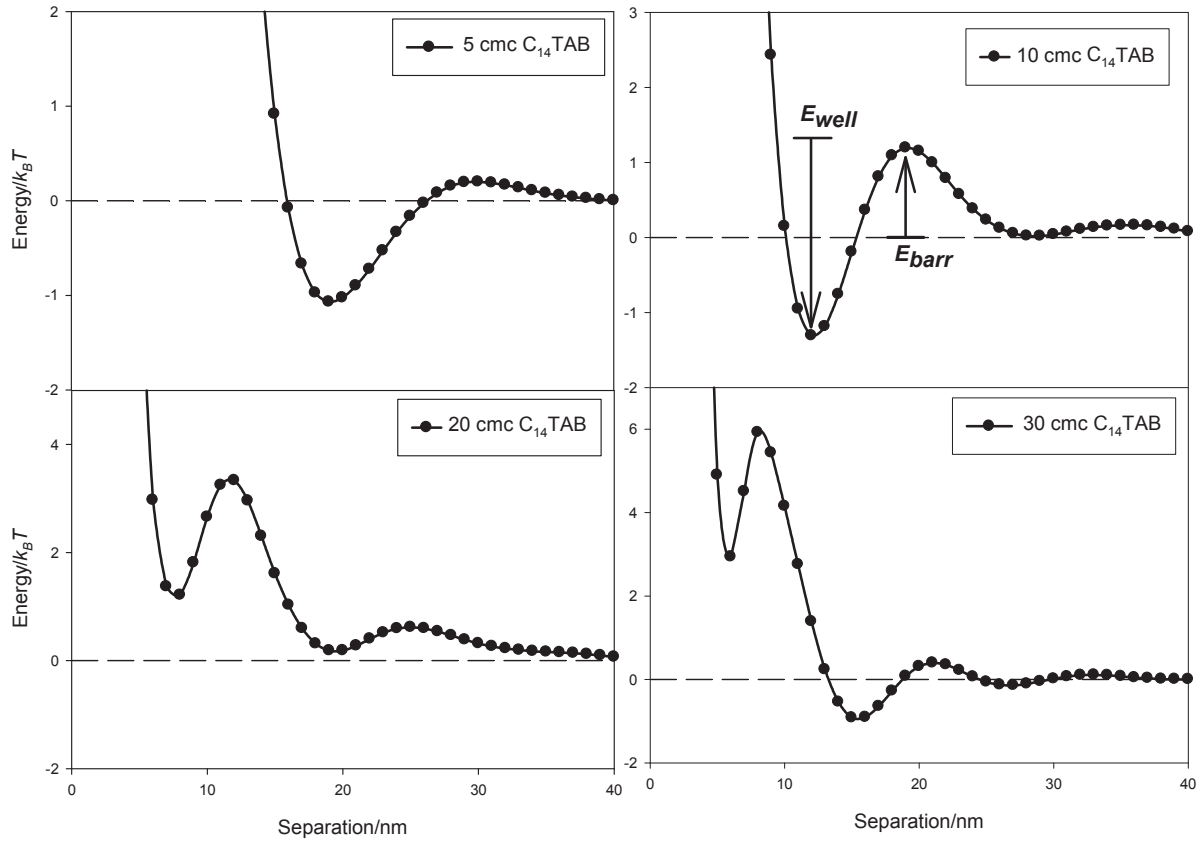

Figure 4-5. Interaction energy profiles for two 0.5 μm diameter silica spheres in varying solutions of C_{14}TAB. An example of how E_{well} and E_{barr} was determined is shown in the 10 cmc C_{14}TAB plot.

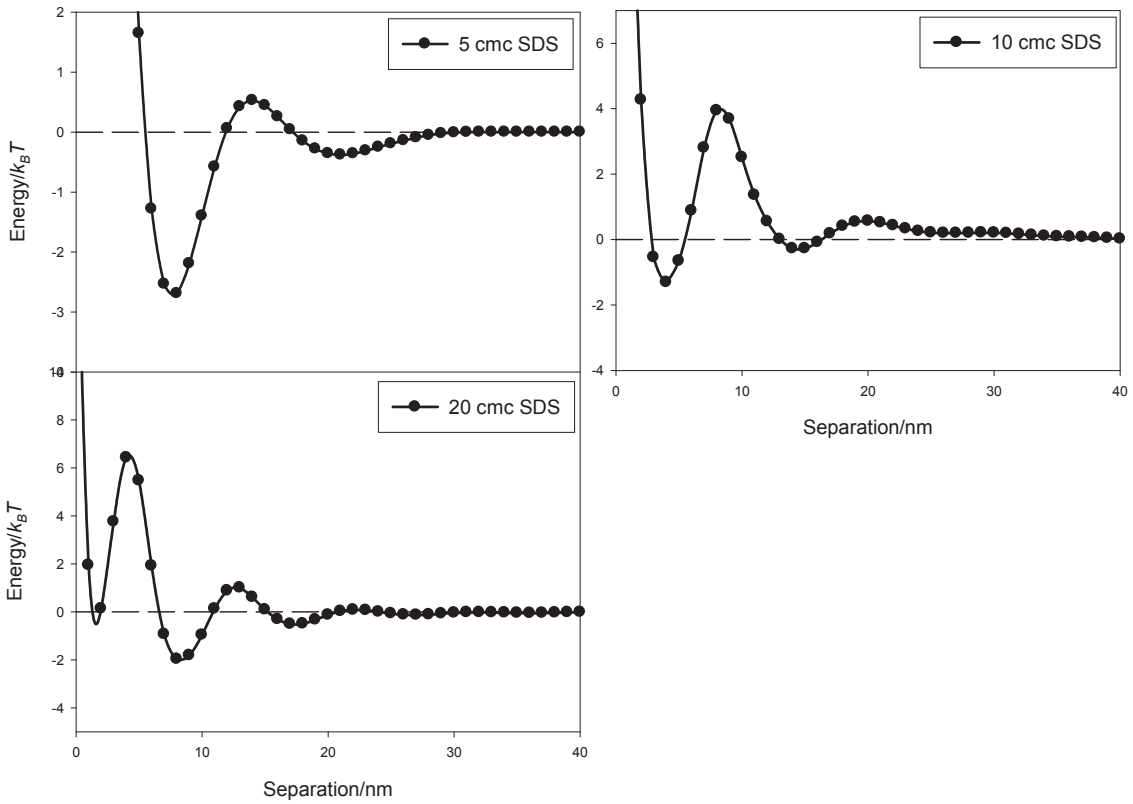

Figure 4-6. Interaction energy profile for two 0.5 μm diameter silica spheres in varying solutions of SDS.

Sample	E_{well}/k_BT	E_{barr}/k_BT
5 cmc C_{14}TAB	1.35	0.25
10 cmc C_{14}TAB	2.75	1.25
20 cmc C_{14}TAB	2.50	3.50
30 cmc C_{14}TAB	3.00	7.00
5 cmc SDS	4.00	1.00
10 cmc SDS	5.50	4.50
20 cmc SDS	6.50	8.50

Table 4-1. Depletion energy well depths and repulsive barrier heights for the interaction of two 0.5 μm diameter silica spheres in varying solutions of C_{14}TAB and SDS.

4.5.2 UV-vis Spectroscopy Results

Figure 4-7 displays an example of a log-log plot of absorbance, *A*, versus wavelength, λ, as described by Eq. [4-3], for a solution of 0.5 μm diameter silica particles in a solution of C_{14}TAB. As seen, the plot is clearly linear, confirming the validity of the power-law relationship, and the turbidity parameter, *n*, can be determined from the slope of a linear fit of the data.

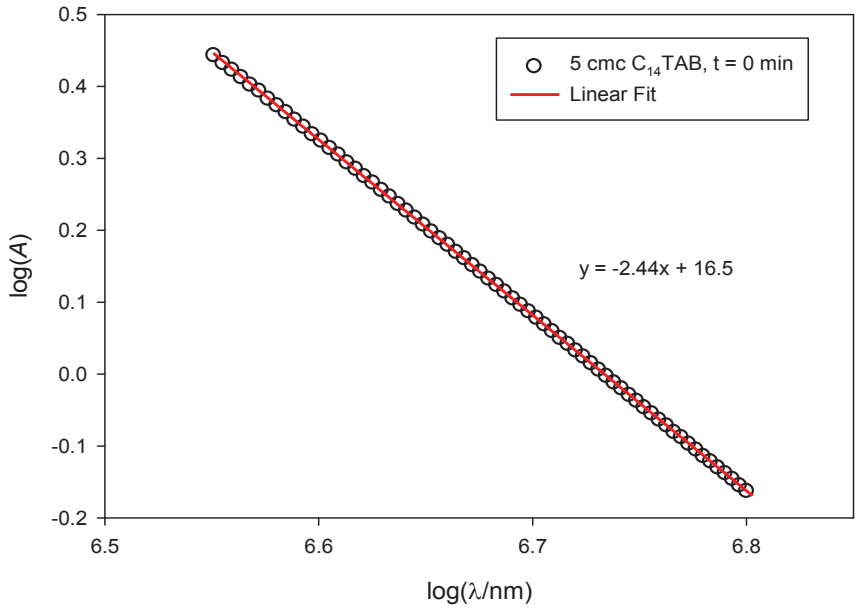

Figure 4-7. Example log-log plot of absorbance for wavelength for 0.5 μm diameter particles in a 5 cmc solution of C_{14}TAB. The turbidity parameter, *n*, can be determined from the slope of the linear fit.

Figure 4-8 and Figure 4-9 plot the turbidity exponent versus time for solutions of 0.5 μm silica spheres in both C_{14}TAB and SDS at various concentrations. Also included in these figures are the results of control experiments where the micellar solution was replaced with a salt solution at equal ionic strength and pH. (Note: KBr was used as a control for C_{14}TAB and NaCl was used as a control for SDS) A summary of the ionic strength and pH for each solution is given in Table 4-2.

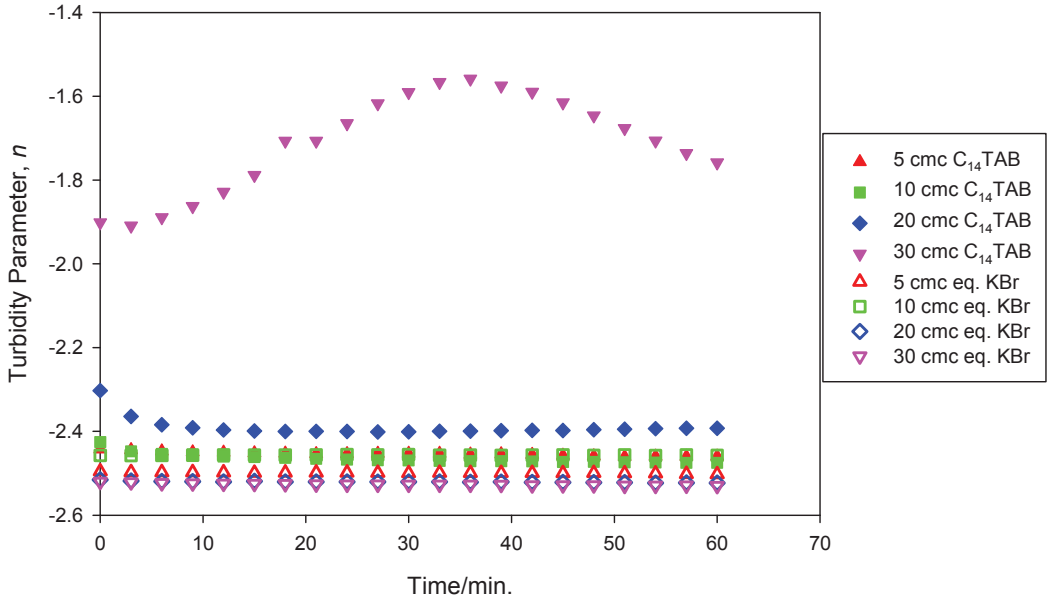

Figure 4-8. Turbidity parameter, *n*, for varying solution of C_{14}TAB containing 0.5 μm diameter silica spheres at 0.1 vol.%. Also shown are the results of control experiments in which KBr replaced C_{14}TAB at equal ionic strength and pH (open symbols).

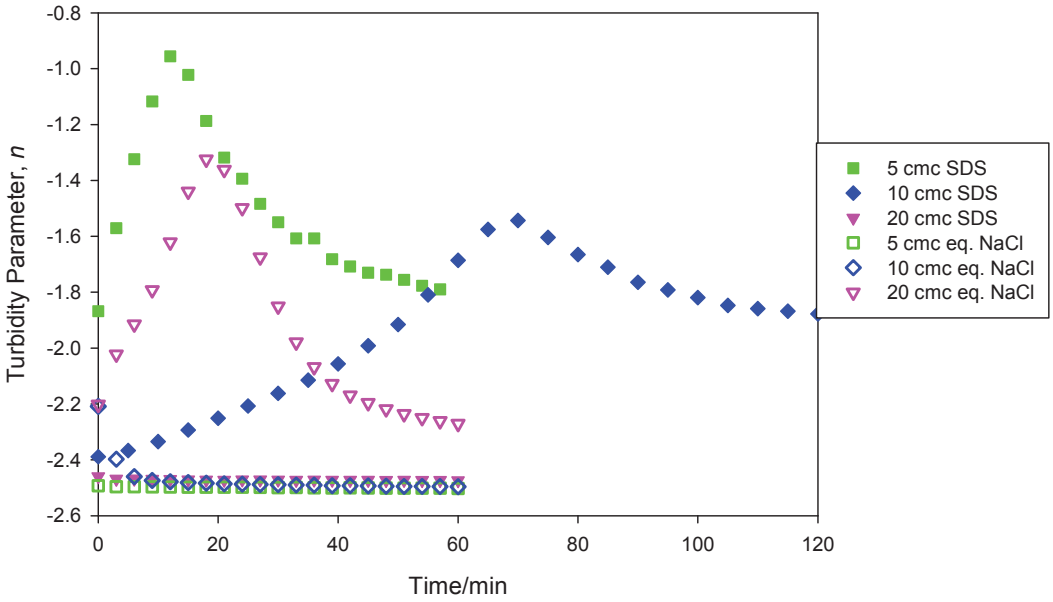

Figure 4-9. Turbidity parameter, *n*, for varying solution of SDS containing 0.5 μm diameter silica spheres at 0.1 vol.%. Also shown are the results of control experiments in which NaCl replaced SDS at equal ionic strength and pH (open symbols).

Sample	pH	Ionic Strength (mM)
5 cmc C_{14}TAB	4.8	5.2
10 cmc C_{14}TAB	4.9	7.4
20 cmc C_{14}TAB	5.0	11.7
30 cmc C_{14}TAB	4.9	16.0
5 cmc SDS	3.8	11.0
10 cmc SDS	3.6	14.8
20 cmc SDS	3.4	23.1

Table 4-2. Summary of the pH and ionic strength of the varying ionic micellar solutions used in CP-AFM and stability measurements.

As can be seen in Figure 4-8 and Figure 4-9, an increase in turbidity exponent was observed for 30 cmc C_{14}TAB and 5 and 10 cmc SDS. There was also an increase in the turbidity exponent for NaCl control solution equivalent to 20 cmc SDS. As described previously, the increase in the turbidity exponent indicates that these solutions are unstable (i.e. flocculating). All other solutions show no increase in the turbidity exponent and are therefore assumed to be stable (i.e. dispersed).

It should be noted that each increase in the turbidity exponent is followed by a subsequent decrease. This trend arises from sedimentation of the larger flocculates, such that the average particle size in the path of the incident light beam decreases.

4.5.3 Photographic Results

The spectroscopy results are further confirmed by photographs of the sample solutions. Figure 4-10 and Figure 4-11 show a series of long term images from stability tests of 0.5 μm silica spheres in micellar and salt solutions of varying concentration at different times. With time, instability of the silica spheres is observed in 30 cmc C_{14}TAB, 5 and 10 cmc SDS, and 20 cmc eq. NaCl. This instability can be seen as a decrease in the turbidity of the solution.

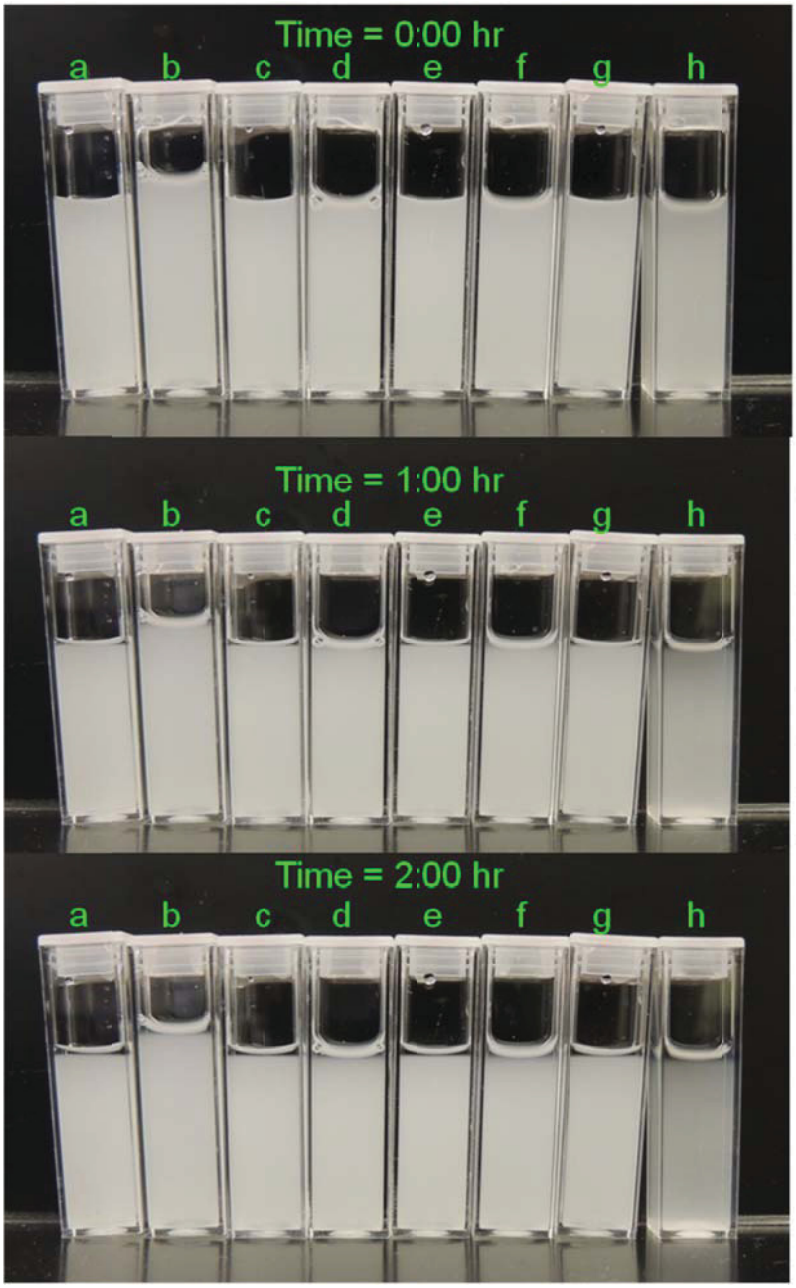

Cuvette	Solution
a	5 cmc eq. KBr
b	5 cmc C_{14}TAB
c	10 cmc eq. KBr
d	10 cmc C_{14}TAB
e	20 cmc eq. KBr
f	20 cmc C_{14}TAB
g	30 cmc eq. KBr
h	30 cmc C_{14}TAB

Figure 4-10. Photographs showing the stability of 0.5 μm silica microparticles in C_{14}TAB and control KBr solutions (equal ionic strength and pH). From left to right the solutions are a) 5 cmc eq. KBr, b) 5 cmc C_{14}TAB, c) 10 cmc eq. KBr, d) 10 cmc C_{14}TAB, e) 20 cmc eq. KBr, f) 20 cmc C_{14}TAB, g) 30 cmc eq. KBr, and h) 30 cmc C_{14}TAB. Weak flocculation in the 30 cmc C_{14}TAB solution can be observed as change in the opaqueness of cuvette h.

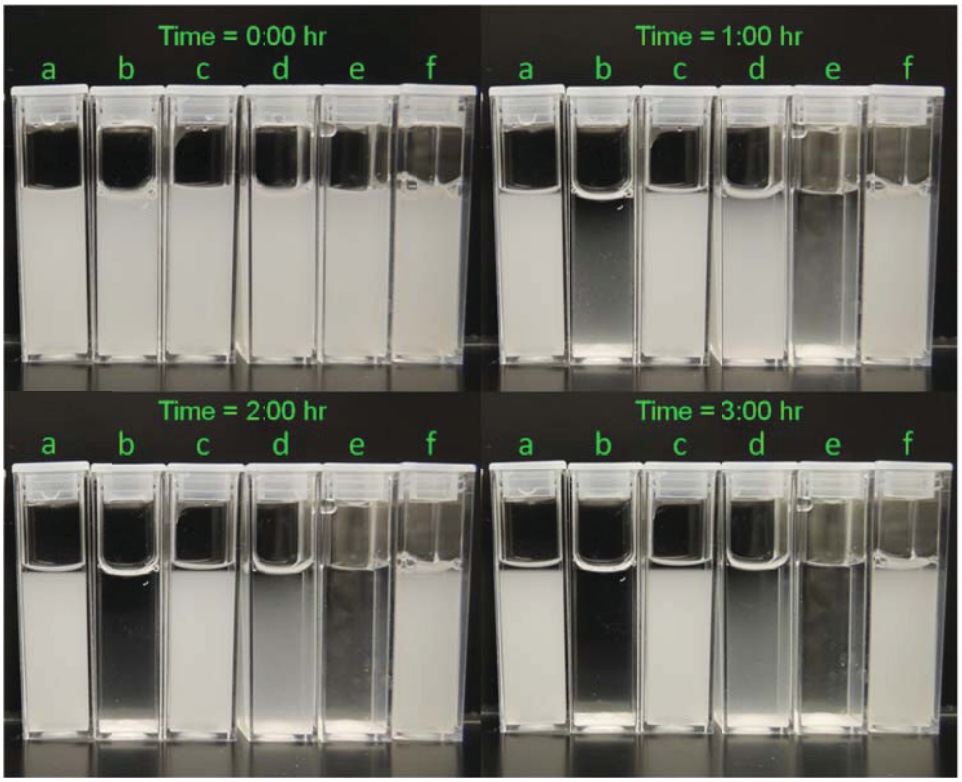

Cuvette	Solution
a	5 cmc eq. NaCl
b	5 cmc SDS
c	10 cmc eq. NaCl
d	10 cmc SDS
e	20 cmc eq. NaCl
f	20 cmc SDS

Figure 4-11. Photographs showing the stability of 0.5 μm silica microparticles in SDS and control NaCl solutions (equal ionic strength and pH). From left to right the solutions are a) 5 cmc eq. NaCl, b) 5 cmc SDS, c) 10 cmc eq. NaCl, d) 10 cmc SDS, e) 20 cmc eq. NaCl, and f) 20 cmc SDS. Flocculation in the 5 and 10 cmc SDS and 20 cmc eq. NaCl solutions can be observed as a change in the opaqueness of cuvettes b, d, and e respectively. Also note that the flocculation in 10 cmc SDS is slower than for 5 cmc SDS or 20 cmc eq. NaCl.

The photographs confirm and provide additional information about the results from the UV-vis spectroscopy measurements. For example, while UV-vis spectroscopy indicated that the 30 cmc C_{14}TAB solution (Figure 4-10 cuvette h) was unstable, the sample still remained relatively cloudy. This indicates that the solution may be only weakly unstable or metastable and that a portion of the silica particles remain dispersed in the solution. This is further supported by the smaller and more gradual change in turbidity exponent (Figure 4-8) when compared with that of 5 or 10 cmc SDS (Figure 4-9).

In addition, we note the fact the 20 cmc SDS solution (Figure 4-11 cuvette f) is stable, while its control solution (20 cmc eq. NaCl), as well as 5 and 10 cmc SDS (Figure 4-11 cuvettes e,b,d respectively), are unstable, is an indication of restabilization arising from the onset of structural forces. We theorize that 20 cmc eq. NaCl is unstable due to the high ionic strength and lower pH of the solution (i.e., lower surface charge density on the silica surfaces).

Finally, the photographs also confirm the UV-vis result (seen in Figure 4-8) that the 10 cmc SDS solution (Figure 4-11 cuvette d) is slower to destabilize than the 5 cmc SDS solution (Figure 4-11 cuvette b). This can be observed as the slower change in

opaqueness of the 10 cmc SDS solution when compared to 5 cmc SDS. This difference in flocculation time is likely caused by the larger repulsive barrier height in the 10 cmc SDS solution.

4.5.4 Phase Diagram Analysis

The results of the stability tests are summarized in the simple phase diagram presented in Figure 4-12, in which the stability is indicated in a plot of the barrier height and well depth of each solution obtained from the measured force profiles. As can be seen from the figure, the stability of the microparticles can be predicted by dividing the plot into two regions. The silica particles remain stable when the interaction of two particles produces a depletion energy well depth less than 3 k_BT. The silica particles will be unstable, however if the depletion energy well depth is greater than 3 k_BT but the repulsive energy barrier height does not exceed 8 k_BT. Finally, particles will remain stable if the repulsive barrier between them exceeds 8 k_BT.

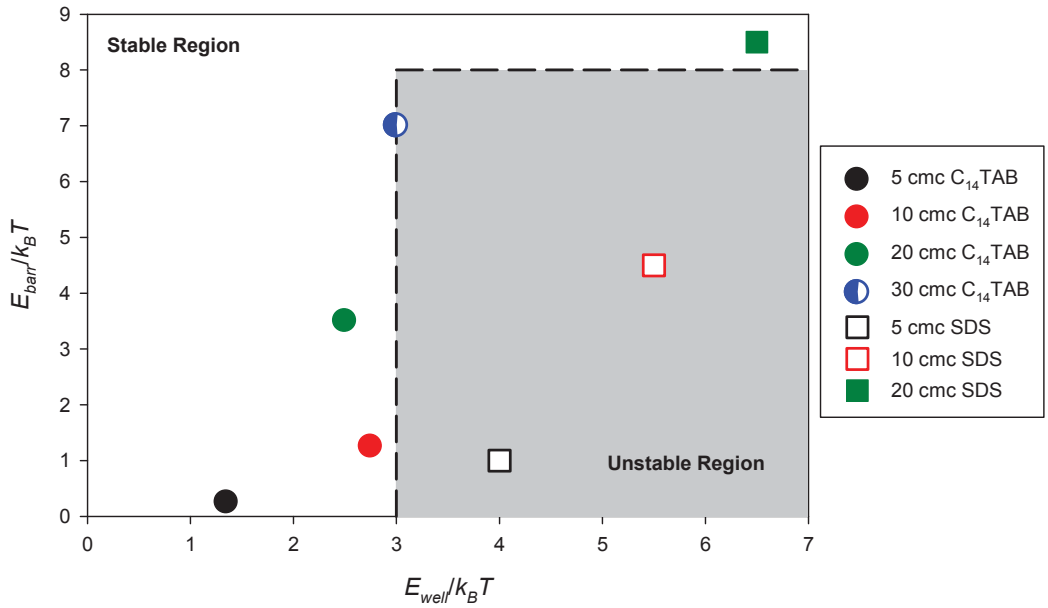

Figure 4-12. Comparison of the stability properties of varying solutions of C_{14}TAB and SDS. Solid points indicate stable solutions, half-point indicate metastable solutions, and open points indicate unstable solutions. Stability is observed for systems in which E_{well} is smaller than 3 k_BT. Instability is observed for systems in which E_{well} is 3 k_BT or larger but E_{barr} is smaller than 8 k_BT. Resabilization is observed for systems where E_{barr} is larger than 8 k_BT.

The observed results agree well with previous predictions for the depth of E_{well} needed to induce flocculation. Previously, Hogg and Yang suggested a well depth of 1.5–10 k_BT was needed in order to induce flocculation[105]. Similarly, Feigin and Napper suggested a well depth of 3 k_BT was necessary to destabilize a colloidal system[103].

Regarding restabilization, we find that a barrier height of 8 k_BT is sufficient to produce restabilization, though we should emphasize that this is based on only one

sample. As a comparision, Feigin and Napper suggest restabilization requires a barrier height of 15-20 k_BT.

4.6 Conclusions

Force-versus-distance measurements for a silica sphere interacting with a flat silica plate in a variety of ionic micellar solutions were converted into energy-versus-distance measurements for the interaction of two silica spheres. These energy profiles display both a depletion energy well and repulsive energy barriers ranging from 1.35-6.5 k_BT and 0.25-8.5 k_BT respectively.

UV-vis spectroscopy was used to determine the turbidity parameter, n, of silica microparticles dispersed in these ionic micellar solutions. Increases in the turbidity parameter indicated an increase in particle size resulting from particle flocculation. This flocculation behavior was consistent with visual observations of the samples. For solutions of C_{14}TAB, flocculation was observed at a concentration of 30 cmc. For solutions of SDS, flocculation was observed at 5 and 10 cmc, while restabilization was observed at 20 cmc.

Comparing the results of these two experiments showed that flocculation will occur when the depth of the depletion energy well is at least 3 k_BT and the height of the repulsive energy barrier does not exceed 8 k_BT. This result generally agrees well with those predicted previously for other systems[103,105].

Chapter 5 Conclusions and Suggestions for Further Work

5.1 Conclusions

This work has presented findings on the topics of colloidal hydrodynamics in nanoparticle dispersions and depletion forces and colloidal stability in micellar dispersions. The three major conclusions that have been drawn are:

(1) *Significant reduction of the effective viscosity is observed as two charged particles approach contact in a complex fluid due to pure fluid regions that form around the particles.* Chapter 2 described the use of CP-AFM to measure the effective viscosity between a particle and a flat plat in a solution of smaller depletant particles, finding that the effective viscosity was reduced to that of the pure dispersing fluid as contact was approached. This experimental work confirmed the theoretical findings of Bhattacharya and Blawzdziewicz[35]. This work also suggests that in the range of most colloidal forces (i.e. <100 nm), particle motion is determined by the viscosity of the dispersing fluid and not by that of the bulk fluid, especially in solutions of low ionic strength.

(2) *The interactions between micelles and other charged surfaces are weaker than those predicted by the charged, hard sphere model in which the surface charge properties of the micelles and surfactant-coated surfaces are assumed to remain uniform.* Chapter 3 presented CP-AFM measurements of the depletion force created by dispersions of ionic micelles. These results illustrated that the model of Walz and Sharma[4] overestimated the magnitude of the depletion force for C_{14}TAB and SDS micellar systems. The results suggest that the physical properties of micelles play a key role in their electrostatic interactions, and that charged, hard sphere electrostatic models are insufficient for properly modeling micelle interactions.

(3) *The stability of a colloidal dispersion in an ionic micellar solution can be predicted using the measured force profile.* Chapter 4 presented findings on the stability of colloidal dispersions in ionic micellar solutions. Destabilization of the colloidal dispersion was observed in both C_{14}TAB and SDS solutions. Restabilization was also observed in the SDS solution. A simple phase diagram was proposed for predicting the stability of the colloidal dispersion based solely on the depletion energy well depth and repulsive energy barrier height.

These results have applications throughout the fields of colloids and surface science. Specifically, they apply to any system where particles of multiple sizes are pumped or moved simultaneously. Example applications include injection molding of reinforced polymers, pumping of mineral slurries, and biological modeling of blood transport.

Additionally, the depletion and stability studies have impacts across fields where surfactants are commonly used as stabilizers including rubbers and mineral transport. Surfactants are also used to stabilize emulsions of immiscible liquids and can be used to contain the fuel source in class B fires[106]. In particular, these results display the important impact surfactant concentration can have solution stability.

5.2 Suggestions for Further Work

From the work presented here, it is clear that there remain several topics upon which further study is called for. For example, as observed in Figure 2-2 and reprinted here as Figure 5-1, it is unclear why at higher scan speeds the oscillations created by structural forces are lost. Tulpar *et al.*[9] theorized a Peclet number analysis to explain this phenomenon, however, in our work the Peclet number remains below one and these oscillations are lost. Further analysis where the scan speed of the AFM is tightly controlled could help to shed light on this subject. Specifically, a study looking for a cross-over-point between oscillations and no oscillations should be performed. This would open the possibility of adapting the Peclet number developed by Tulpar *et al*.

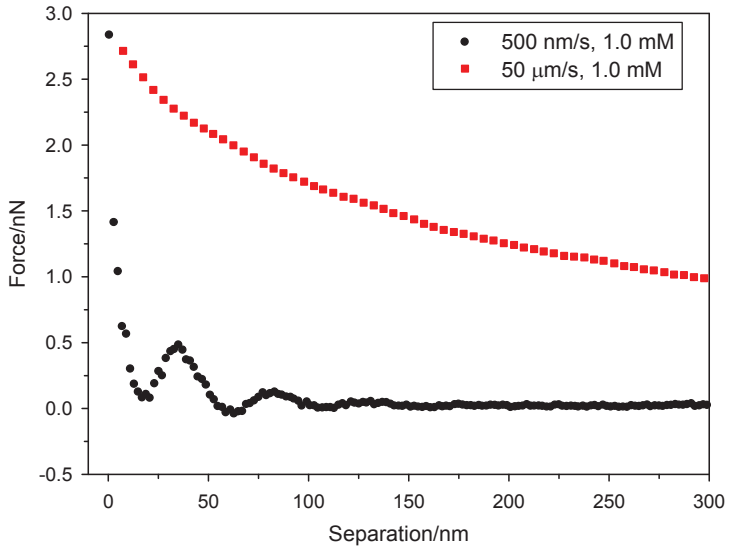

Figure 5-1. Comparison of the force profile at scan speeds of 500 nm/s and 50 μm/s. This data was taken in an 8 vol.% nanoparticle solution at 1 mM ionic strength.

Additionally, the work measuring and modeling depletion forces in micellar solutions shows a clear need for more research into the interactions between micelles. The first and largest need would be a more rigorous model for describing multibody interactions in binary colloidal solutions. While the model of Walz and Sharma[4] does an excellent job of modeling these interactions for low concentrations of depletants, more work is needed for higher order interactions.

Additionally, experimental work could be completed to determine what may cause the deviations observed between solutions of micelles and charged, hard spheres. As suggested in this work and by others[72], the effects of confinement on micelles are clearly important in their interactions and further study is needed to understand these phenomena.

It may also be of interest to study what effects, if any, micelle surface adsorption plays in the depletion force. For example, further studies of the depletion effects between two positively charged surfaces in solutions of C_{14}TAB and SDS could prove interesting when compared with the results of this study. Specifically, does micelle surface adsorption or a lack thereof, change the effective micelle surface potential needed for matching the results of the Walz and Sharma model to the measured experimental results.

Appendix A Review of the Technique of Colloid-Probe Atomic Force Microscopy

A.1 Review of the Atomic Force Microscope

The Atomic Force Microscope (AFM) was first developed by Binnig and Quate[107] in 1986 and has today become a crucial instrument in the field of interfacial science. The first AFMs where used as imaging devices and allowed nanometer or in some cases Angstrom level resolution on conducting and nonconducting surfaces. The AFM's ability to image nonconducting surfaces is what sets it apart from other high resolution microscopy techniques including scanning electron microscopy (SEM) and scanning tunneling microscopy (STM).

Figure A-1 is a schematic representation of an AFM. Piezoelectric drives control the sharpened cantilever tip and/or the surface being analyzed. These drives allow for Angstrom level control of the cantilever or surface position in three dimensions. Initial imaging work used a feedback loop to hold the sharpened cantilever tip onto the surface with a fixed deflection (*i.e.*, magnitude of force). This deflection is measured using a laser reflected off the back of the cantilever and onto a photo detector. As the tip moves over the surface of interest the cantilever must be driven toward or away from the surface in the z-direction by the piezo drive to maintain the force. Plotting z-directional movement versus x-y position produces a topographical image of the sample. Imaging by this technique has come to be known as "contact mode imaging."

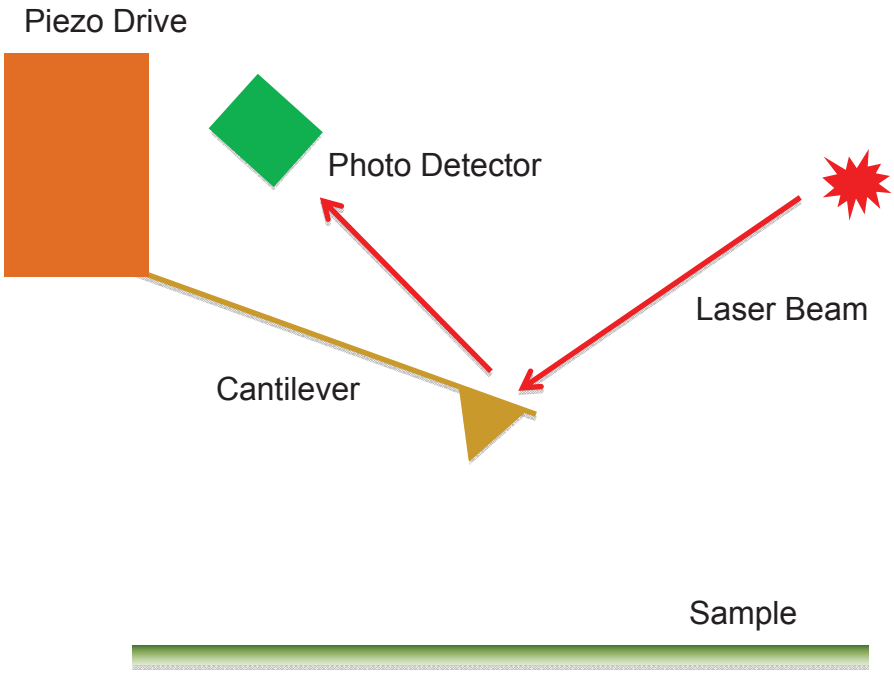

Figure A-1. Schematic Representation of an AFM

Contact mode imaging is limited in application to “hard” surfaces. That is surfaces that are not damaged by the force applied from the cantilever. A second technique known as noncontact or tapping mode imaging also has been developed for “soft” samples. In this technique, the cantilever is driven at its resonance frequency and an image produced by measuring the changes that occur in the amplitude of oscillation. Noncontact imaging has many applications in the biological, polymer, and materials characterization fields due to its nondestructive nature. Because this work focuses on contact mode techniques, no further elaboration on noncontact techniques will be made here; however, a review of noncontact AFM is available from Morita and coworkers[108].

Besides imaging, the AFM can also be used to measure the force acting between two surfaces. In this technique, the AFM cantilever is driven towards or away from the surface of interest at a known velocity, and the deflection of the cantilever is measured. This technique is valuable for measuring force; however, in early work characterizing the exact properties of the cantilever tip proved difficult. These issues in tip characterization lead to the development of the technique of Colloid-Probe AFM (CP-AFM) which allowed for better definition of the probing tip properties. CP-AFM is the major technique used in this work and will be elaborated on further.

A.2 Colloid-Probe Atomic Force Microscopy

The technique of colloid-probe AFM was first developed by Ducker *et al*.[50] and Butt[109] in 1991. In their pioneering work, the authors glued a silica sphere and a glass sphere, respectively, onto the end of an AFM cantilever. This adaptation to the cantilever created many improvements to force measurements using AFM.

The first improvement was well defined probe properties. Because the mounted spheres were of known size and material properties, they were better defined than the AFM cantilever tips of the day. This allowed for a more quantitative analysis of the force between surfaces. Secondly, the larger particles increased the magnitude of the force applied to the cantilever from the surface giving more resolution to the measurements. Later, hydrodynamic force measurements became possible with the combination of colloid-probes and AFMs with high scan rates.

A.3 Surface Characterization

Any hard material that can be made into a smooth spherical surface can be used as a probe particle. In practice, the attached colloidal particles range from 2 to 30 μm in size. Silica and glass are by far the most widely used type of colloidal particle due to their commercial availability and minimal rms roughness. Figure A-2 is an SEM image of a colloidal particle glued to an AFM cantilever.

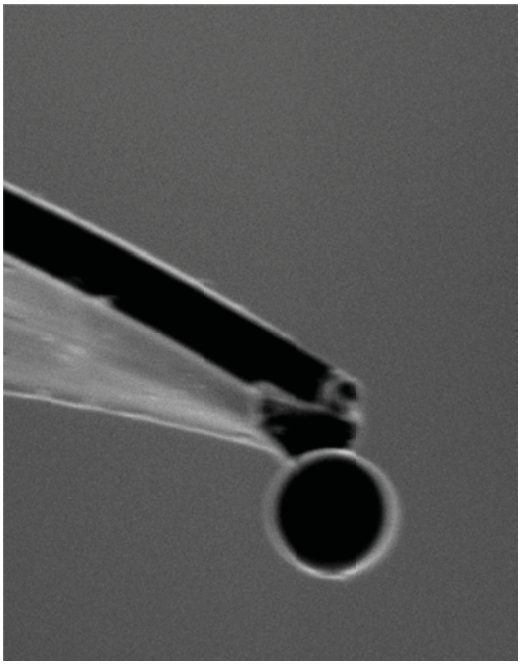

Figure A-2. SEM image of a micron-sized silica particle glued to an AFM cantilever

For this work, characterization of the physical properties of the probe surfaces is performed using several techniques. (1) Optical microscopy is used to measure the size of the particles and (2) probe surface roughness is measured using the inverse tip grating technique.

To measure the size of the particle, the probe is imaged using an optical microscope with a 50x objective connected to a computer. A pixel counting ruler is then used to measure the diameter of the particle. The ruler is calibrated using an AFM grating with known step sizes.

To measure the surface roughness, the colloid probe is contact mode imaged against an AFM tip grating. This grating is made up of many cone shaped tips with very small radii of curvature (~2 nm) at their tips. As the colloid-probe passes over the tip, the z-displacement of the cantilever gives an image of the colloidal topography. Figure A-3 is a schematic of this technique and Figure A-4 is an example of a topographical image of 5 μm colloidal particle.

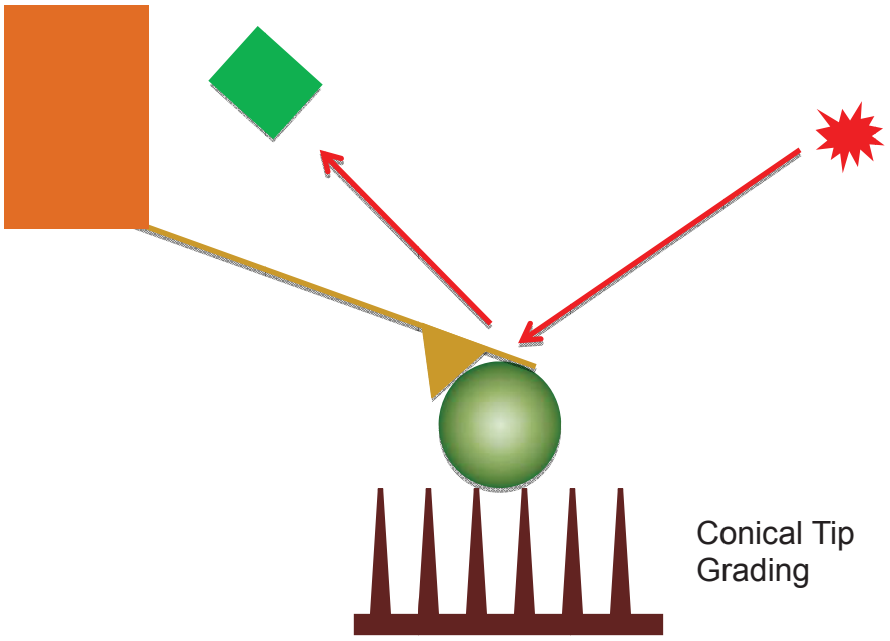

Figure A-3. Schematic of the imaging of the surface topography of a colloidal particle

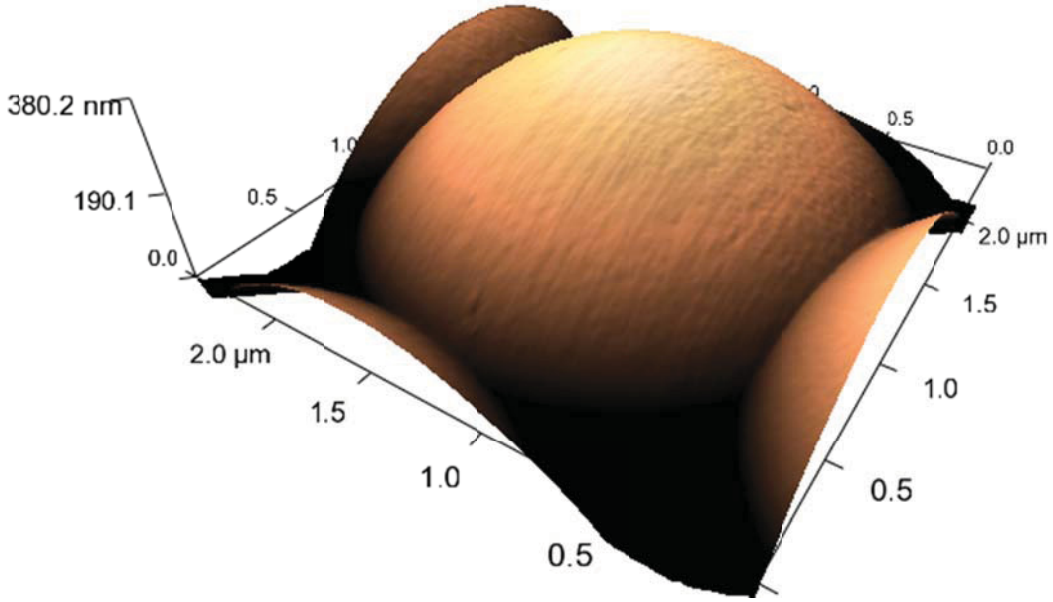

Figure A-4. AFM topographical image of a 5 µm silica sphere. Note: The secondary peaks around the image are additional pictures of the sphere as it mapped over other conical tips on the grading.

Measuring the surface topography is important in eliminating surface roughness as an error in the force measurement. Surface asperities can cause deviation in the absolute separation distance between the colloidal-probe and the surface. For this

reason, colloidal particles used in experiments had a measured rms roughness less than 1 nm over 1 μm^2.

A.4 Cantilever Spring Constant Calibration

The force acting on the colloidal-probe from the surface is balanced by the cantilever's restoring force. This restoring force is what is actually measured in the AFM experiment. The magnitude of the restoring force is the product of the cantilever's spring constant and the cantilever's deflection.

Theoretical and experimental methods have been developed for determining the cantilever spring constant. In practice experimental methods are preferred for determining the spring constant because they do not require knowing the exact dimensions of the cantilever. Because AFM cantilevers are produced in mass quantities, small variances exist between each individual cantilever and these variances can have significant effects on the cantilever spring constant.

In this work, the thermal noise method of Hutter and coworkers[51] is used to measure cantilever spring constants. The cantilever is modeled as a harmonic oscillator which results in the mean square deflection, $\langle \Delta Z_c^2 \rangle$, given by

$$\frac{1}{2} k \left\langle \Delta Z_c^2 \right\rangle = \frac{1}{2} k_B T \qquad \text{[A-1]}$$

where k is the cantilever spring constant, k_B is the Boltzman constant, and T is the absolute temperature. Simple rearrangement allows Eq. [A-1] to be solved for the spring constant

$$k = \frac{k_B T}{\left\langle \Delta Z_c^2 \right\rangle}. \qquad \text{[A-2]}$$

Solving for $\langle \Delta Z_c^2 \rangle$ is accomplished by measuring the thermal fluctuations of the cantilever over a range of frequencies to obtain power spectral data. Removing any background noise allows the primary resonance frequency peak to be isolated and fit to a Lorentzian curve. The area under the primary resonance frequency peak, P, is equal to the mean square deflection of the cantilever, $\langle \Delta Z_c^2 \rangle$. Integrating the fitted Lorentzian curve and rewriting Eq. [A-2] so that

$$k = \frac{k_B T}{P} \qquad \text{[A-3]}$$

allows for the experimental determination of the cantilever spring constant, k. It should be noted that the AFMs used in this work have built in program functions that allow for the automation of cantilever spring constant calibration.

A.5 Force Curve Data Analysis

The piezo drive distance and deflection data generated by an AFM must be manipulated to generate Force versus Probe-Plate Separation curves. In 1992, Ducker and coworkers developed a method for performing this manipulation[50].

Figure A-5 shows a representative example of raw AFM data. In this figure, cantilever deflection in volts is plotted against piezo drive distance in nanometers.

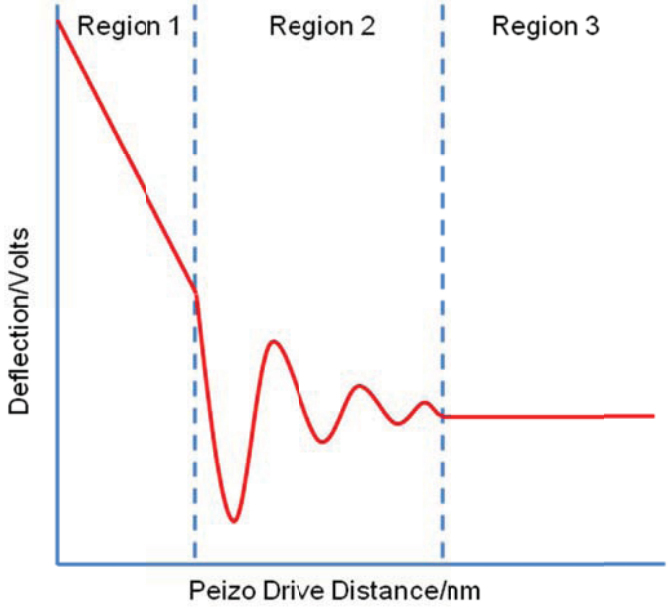

Figure A-5. Example of raw AFM data. Each region represents a different aspect of the curve.

Figure A-5 is broken down into three regions. Region 1 represents the contact region between the probe and plate. This region is defined by its linear characteristic. Region 2 is the near contact region between the cantilever and plate and is defined by probe-plate interactions along with other colloidal interactions. Region 2 is the region of interest in most CP-AFM experiments. Region 3 represents particle plate separations at long ranges. In this region there is typically no interaction between the probe and plate at low approach velocities and only hydrodynamic interactions at high approach velocities.

To convert the raw AFM data into force versus separation data three steps must be taken: (1) the cantilever deflection must be converted from the arbitrary unit of volts to non-arbitrary distance units, (2) the voltage representing zero cantilever deflection must be defined, and (3) the position of contact between the particle and the plate must be defined.

To convert the cantilever deflection from volts to a non-arbitrary distance unit (for AFM measurements this unit is typically nanometers) region 1 of Figure A-5 is used. In this region, known as the constant compliance region, the deflection, *Defl*, changes linearly with the piezo drive distance, *Drive*, because the probe and plate are in contact.

For hard surfaces, like those used in this work, the slope of Figure A-5 in region 1 is known as the optical-lever sensitivity (OLS) and is defined as

$$OLS = \frac{dDefl(volts)}{dDrive(nm)}. \quad [A\text{-}4]$$

Because the cantilever is significantly more compliant than either the probe or plate, it may be assumed that the cantilever will deflect equally with the piezo drive distance when the probe and plate are in contact. That is

$$\frac{dDefl(nm)}{dDrive(nm)} = 1 \quad [A\text{-}5]$$

for hard surfaces in contact.

Using the hard surfaces assumption, the inverse of Eq. [A-4], known as the invOLS, can now be used to convert the arbitrary deflection voltage to deflection distance. That is

$$Defl(nm) = invOLS \times Defl(volts). \quad [A\text{-}6]$$

Step 2 in creating a force versus separation plot is defining zero deflection of the cantilever. For typical force curves taken at low velocities (those velocities that do not produce measurable hydrodynamic forces), region 3 of Figure A-5 is used. At large separation distances an average of the arbitrary deflection value is calculated and subtracted from the entire force curve. This defines the value of the force in region 3 as zero.

For the high approach velocities used in hydrodynamic measurements a variation to this procedure must be used. When using high velocities (>10 μm/s), the cantilever deflection, even at large separations (> 5μm) of probe and plate, will not be equal to zero; therefore, region 3 cannot be used to define zero deflection. Instead, data is taken after the cantilever comes to rest (*i.e.*, velocity = 0) away from the plate. The average value of deflection of the nonmoving cantilever is then used to define zero deflection.

Finally, the actual separation distance between the probe and the plate can be determined. To do this, separation distance, *h*, is defined as a function of both deflection and piezo drive. This gives

$$h - h_0 = Defl - Defl_0 + Drive - Drive_0 \quad [A\text{-}7]$$

where h_0, $Defl_0$, and $Drive_0$ are the arbitrary zero positions of separation, deflection, and piezo drive respectively. Because h_0 is dependent upon $Defl_0$ and $Drive_0$ and $Defl_0$ and $Drive_0$ are both arbitrary, these three unknowns can be combined into a single unknown variable h_0' giving

$$h = Defl + Drive + h_0'. \quad [A\text{-}8]$$

Solving for h_0' can then be accomplished using the relationship that h=0 while the cantilever undergoes constant compliance.

A.6 High Velocity Force Curve Analysis: Virtual Deflection and Cantilever Drag

Figure A-6 shows raw approach and withdrawal data curves for the interaction of a ~30 μm diameter silica particle and a flat silica plate in 8 vol.% nanoparticle solution (this data was taken at a scan speed of 20 μm/s) as described in Chapter 2. At large separations (>4000 nm), the data appears to show a linear force on both approach and withdrawal (the positive slope in both curves from 4000 to 7000 nm). This slope is caused by virtual deflection, which is present in top-scanning AFM systems due to their design. This deflection has been seen in other experiments and is well documented. Zhu *et. al*.[110] describes virtual deflection as being caused by flexure on the edges of the Z-stage when pressure is applied by the centrally placed piezo transducer. This flexing slightly changes the distance and angle between the laser, cantilever, and detector, causing what appears to be deflection of the cantilever. Since the bending of the Z-stage is elastic in nature, it occurs with the same sign and magnitude in both the approach and retraction curves. Honig and Ducker[45,111] found that by 'wiggling' the laser and detector positioning wheels to relieve tension, virtual deflection could be minimized but not eliminated. It is our belief that virtual deflection is caused by a combination of Z-stage flexure and tension on the laser and detector components.

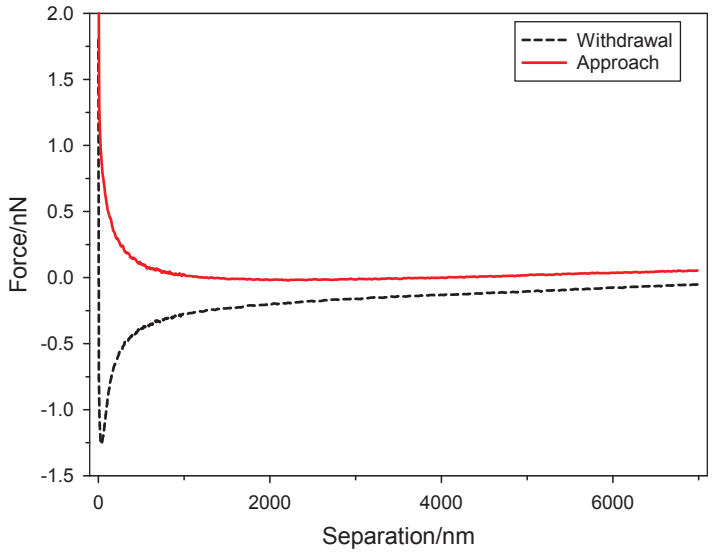

Figure A-6. Measured approach and withdrawal curves in an 8 vol.% nanoparticle solution taken at a scan rate of 20 μm/s. The positive and equal slope of the approach and withdrawal curves at large separations is caused by virtual deflection – an artifact in the type of AFM used here.

To correct for virtual deflection, the fact that the hydrodynamic force (the only force that should be acting at large separations) is symmetrical on approach and withdrawal is used; thus in this regime, the forces measured upon approach and retraction should sum to zero. With virtual deflection, however, this symmetry is broken, and we can write

$$F_{virtual} = \frac{F_{measured,approach} + F_{measured,withdrawal}}{2}, \qquad \text{[A-9]}$$

where $F_{virtual}$ is a hypothetical 'equivalent force' arising from virtual deflection. Using Eq. [A-9] and the data at large separations (*i.e.*, >4000 nm), a simple straight line representing virtual deflection is obtained, which can then be subtracted from the approach and withdrawal curves.

This method is very similar to that used by Zhu *et. al*.[110], however these authors calculated the relative slope of the approach and retraction curves at large separations before summing and dividing by two. We prefer our method for calculating the virtual deflection because it also corrects for any errors in the piezo zero position (zero deflection position) that might be caused by virtual deflection.

Figure A-7 shows a comparison between a measured approach curve, corrected for virtual deflection, with the theoretically-predicted curve (as explained in Section 2.5, the force measured upon approach of the particle to the plate will be focused on). These results were obtained with a 50 μm/s scan speed. The theoretical curve was generated using Eq. [2-12] and the MATLAB ode solver as described previously (the specific conditions used are given in the figure caption). We see that the measured force values are greater than those predicted at large separations. As discussed in section 2.2, Bhattacharya and Blawzdziewicz[35] predicted that at the effective viscosity characterizing the drag force exerted on the sphere can change with position and that this effect can extend to relatively large distances. (The theoretical curve in Figure A-7 was calculated using the bulk viscosity.) However, as can be seen in the Figure A-7, differences between the measured and theoretical force curve are observed at separation distances as large as 6000 nm (nearly 300 times the diameter of the nanoparticles) and based on the predictions of Bhattacharya and Blawzdziewicz, the effective viscosity should be essentially equal to that of the bulk fluid at separation distances this large. In addition, Bhattacharya and Blawzdziewicz predicted that the effective viscosity never exceeded the bulk viscosity, which cannot explain the results in Figure A-7 (the measured force at large distances in Figure A-7 is *greater* than that predicted, which would require an effective viscosity larger than the bulk).

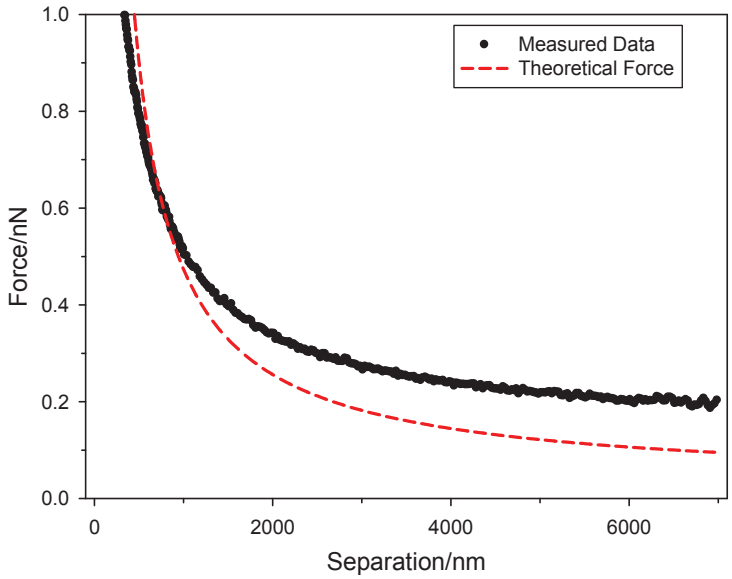

Figure A-7. Measured data corrected for virtual deflection compared to theoretical force curve in an 8 vol.% nanoparticle solution. The theoretical curve was calculated using Eq. [2-12] and the following parameters: particle radius = 14.4 μm, initial separation distance = 7 μm, scan speed = 50 μm/s, spring constant = 0.0573 N/m, solution viscosity = 2.2×10^{-3} Pa-s.

It is our hypothesis that the cause of this discrepancy at large distances is due to hydrodynamic force exerted on the AFM cantilever as it is pushed toward the plate. Thus the total force measured consists of that exerted on the particle plus that exerted on the cantilever. Cantilever drag has been reported by a number of other authors[9,45,111], although the methods for correcting for it vary. As further evidence that this is the cause of the discrepancy, shown in Figure A-8 are the results of a series of measurements that were performed in an 8 vol.% nanoparticle solution using a cantilever only (*i.e.*, without a particle glued to the tip). The force is clearly detectable at the scan speeds used in the experiments, and at any given separation distance the force increases proportionally with scan speed. In addition, this force increases at smaller separation distances, presumably because of a squeezing flow developing between the cantilever and plate.

Although the magnitude of the force in Figure A-8 looks comparable to the force in Figure A-7 (with an attached particle), it must be kept in mind that the separation distances here are quite different. In an experiment with an attached particle, the cantilever never gets closer to the plate than the particle diameter, which is approximately 30 μm in the experiments. At these large distances, the force on the cantilever would obviously be much smaller than those shown in Figure A-8.

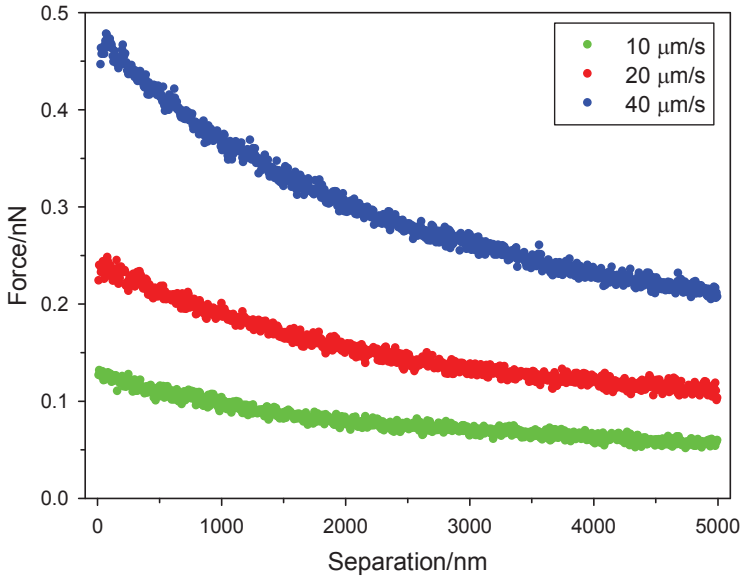

Figure A-8. Hydrodynamic forces measured at different scan speeds on an AFM cantilever with no attached particle. These measurements were obtained in an 8 vol.% nanoparticle solution at 1 mM ionic strength.

To determine the contribution of the cantilever resistance in the results, it is first assume that the hydrodynamic force at large separation distances can correctly be predicted using Eq. [2-12] assuming a constant viscosity equal to that of the bulk dispersion. Specifically, for separation distances larger than 5000 nm, it is assumed that the effective viscosity is equal to that of the bulk. It can thus be written

$$F_{cantilever} = F_{measured} - F_{theoretical} \quad \text{for } h > 5000 \text{ nm} \qquad \text{[A-10]}$$

where the theoretical force is calculated using the known bulk viscosity. This cantilever contribution is then fit to a linear expression with separation distance and subtracted from the measured results. (Note that the force on the cantilever is also adjusted proportionally with changes with the approach rate, dh/dt, since the particle slows as contact is approached.) It should be emphasized that this procedure was actually performed in each nanoparticle solution.

While we clearly recognized that the function form of the cantilever resistance may not be linear over all separations, the assumption is that the linear form will be an adequate approximation at the large separation distances encountered here. (Recall that at zero separation distance in Figure A-7, the cantilever is actually 30 μm from the surface.)

As a test of the validity of this approach, Figure A-9 presents the results of an experiment conducted in a 1 mM aqueous solution with no nanoparticles. Since the viscosity is constant here, Eq. [2-5] should be valid over the entire range of separations. In this figure, the filled red circles represent the measured hydrodynamic force, corrected for virtual deflection, while the solid green line is the model prediction made

using a constant viscosity of $1x10^{-3}$ Pa-s and Eq. [2-12]. As seen, there is a significant discrepancy at large separation distances, which is the result of the hydrodynamic force on the cantilever. Subtracting the predicted force from that measured at each separation distance yields the curve represented by the blue diamonds. While this force looks almost flat on this scale, there actually is a slight negative slope. Following the procedure that is used for the data taken in the nanoparticle solutions, we fit this cantilever drag to a straight line using only the forces above 5000 nm – this is represented by the black dashed line. It is clear that this approach provides a good fit to the data over nearly the entire range of separations.

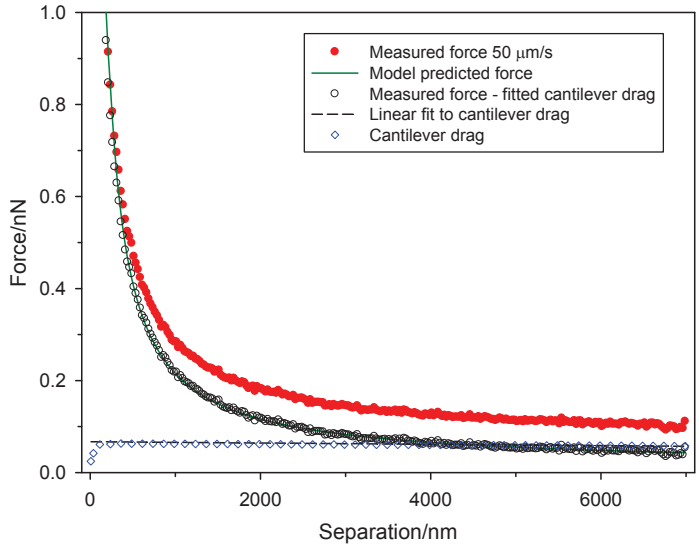

Figure A-9. Results of an experiment conducted in 1 mM water with a scan speed of 50 μm/s illustrating the effects of cantilever drag. The red filled circles represent the measured force (corrected for virtual deflection) while the solid green line is the force predicted using Eq. [2-12]. The difference between these two curves is represented by the open blue diamonds – this is the cantilever contribution. The dashed black line is a linear fit to this cantilever drag using the data beyond 5000 nm separation, and the black open circles is the measured force minus the cantilever drag.

As can be seen, the cantilever drag appears to suddenly drop off at very small separation distances (*i.e.*, <50 nm). There are several possible explanations for this. First, colloidal forces, such as van der Waals forces or electrostatic forces between the charged test particle and plate, become more significant at smaller separations, meaning that the measured force in Eq. [A-10] will no longer be solely due to hydrodynamic forces. Second, there could be a finite amount of amount of roughness on the surface of the test particle and plate, which will cause the measured separation distances to be slightly incorrect. Specifically, in an AFM experiment, separation distance is measured relative to the point of hard contact between the particle and plate. If either surface contained small asperities, the true distance between the mathematical surfaces of the sphere and plate would be larger than that measured, meaning that the measured drag force on the particle would be less than that predicted. Smart and

Leighton[112] showed that a small surface coverage of hemispherical asperities would not have a significant effect on the flow in the lubrication layer but would simply limit the minimum approach distance. (This assumption was also used to explain some anomalies in the results of Tulpar and Walz[9] described in section 2.2.) Because of the 1/*h* dependence of the drag force on separation, this effect becomes more pronounced at smaller separations. Although both the silica plate and large silica particles were found to be quite smooth (*i.e.*, rms roughness <1nm over 1μm^2), the divergent nature of the drag force near contact means that even small offsets in separation distance can cause significant difference in the predicted drag.

However, it should be emphasized that while these effects may cause the cantilever drag force to be slightly distorted at small separations, the effect is relatively unimportant, primarily because at these separations, the cantilever drag becomes a minor component of the total force. The open circles in Figure A-9 show the measured force with the cantilever drag subtracted. As seen, the agreement between theory and measurement is now very good over all separations, which supports our method for correcting for the cantilever contribution.

A.7 Low Velocity Force Curve Analysis

For lower approach velocities (<100 nm/s) a variation to the procedure described in section A.6 is used to correct for virtual deflection. Figure A-10 shows a raw approach data curve for the interaction of a 5 μm diameter silica particle and a flat silica plate in a 1 cmc C_{14}TAB solution. Similar to Figure A-6, at large separations (>500 nm), the data appears to show an attractive force as the particle approaches the plate (the positive slope in the curve from 500 to 1000 nm).

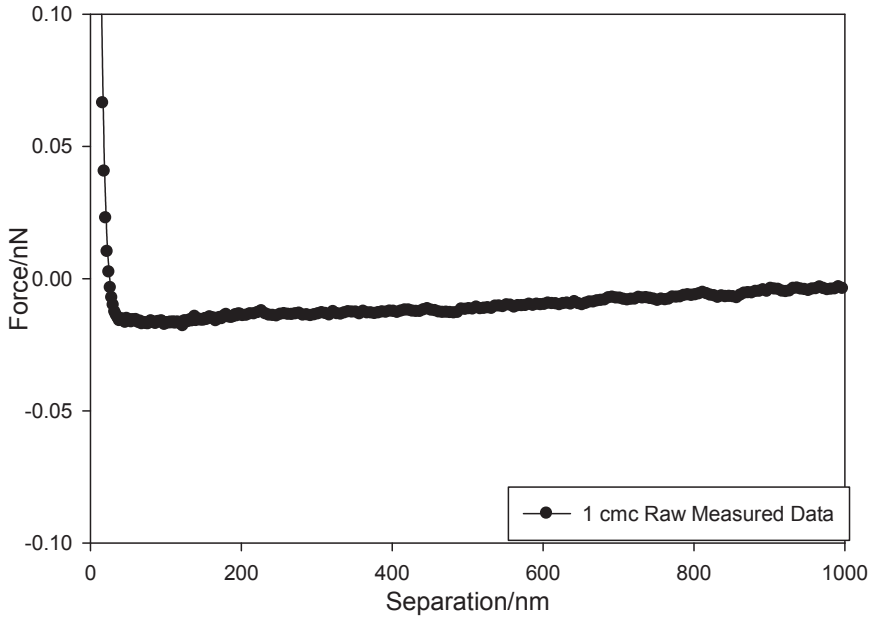

Figure A-10. Measured approach curve in a 1 cmc C_{14}TAB solution taken at a scan rate of 50 nm/s.

To correct for virtual deflection, it is assumed that the hydrodynamic force (the only force that should be acting at large separations) is effectively zero at low approach velocities. Using the data at large separations (*i.e.*, >500 nm), a simple straight line representing virtual deflection is obtained, which can then be subtracted from the approach curve. This difference in technique from that described in section A.6 stems from a lack of symmetry in the virtual deflection due to the slow approach velocities used. At these slow approach velocities, thermal drift is significant between the approach and withdrawal curves and, therefore, virtual deflection does not act on approach and withdrawal symmetrically.

Appendix B Additional Work Performed

B.1 Measurement of the Hydrodynamic Force in Solutions of Nanorods

Upon completion of the hydrodynamic force work with nanoparticles described in Chapter 2, attempts were made to perform similar measurements with nanorods. Silica nanorods were synthesized by the method of Philipse *et al*.[113] that was later expanded upon by van Bruggen[114]. The rods consisted of a boehmite (AlOOH) core coated in silica. The rods had an average length of 236 nm and an average diameter of 64 nm. Figure B-1 is an SEM of a dried sample of some of the nanorods produced.

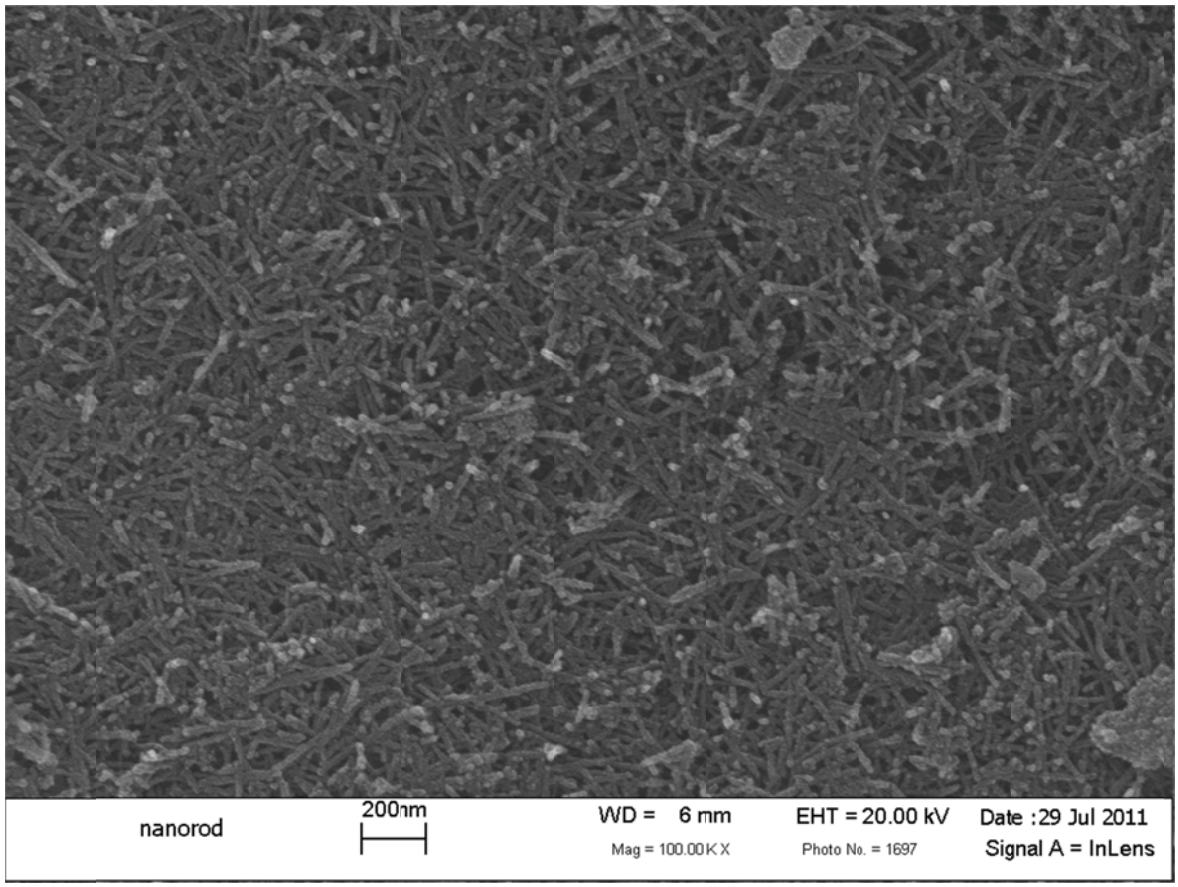

Figure B-1. SEM image of synthesized silica nanorods

It was hypothesized that the rods would show similar characteristics to those seen in the previous measurements with nanospheres. The possibility of rod alignment due to sheer was also considered. Studying the combination of these two effects via AFM appeared promising. Also, few studies of the depletion force created by nanorods exist[115-116]; therefore, directly measuring this force was also of interest.

However, working with nanorods presented many unforeseen challenges. First, producing the rods took a minimum of three weeks due to the long periods of dialysis needed. Secondly, high enough concentrations of rods to create a measurable change

in the solution viscosity were never able to be produced. Thirdly, when concentrated, the rods produced an opaque, white solution. This solution was incompatible with use in the AFM because the laser would be unable to transmit through it. For these reasons, work on solutions of nanorods was terminated.

B.2 Results and Discussion for the Measurement of the Hydrodynamic Force Produced in Ionic Micellar Systems

Following the procedure outlined in section 2.4, additional hydrodynamic force measurements were also performed in solutions of sodium dodecyl sulfate (SDS) micelles. The goal of these experiments was to determine if the results presented in section 2.5 for hard, charged spheres also applied to micelles.

These experiments were performed at a single concentration of 30 times the cmc for SDS. At this concentration, the micelles have a radius of 2.0 nm, a concentration of 5.25 vol.%, and the solution has a Debye length of 1.75 nm. The calculation of these values is discussed in detail in Chapter 3. The measured solutions viscosity was 1.58x 10^{-3} Pa*s.

Figure B-2 shows the effective viscosity results for a ~30 μm diameter sphere approaching a flat plate in a solution of 30 cmc SDS micelles at varying approach velocities. The effective viscosity is calculated by the same method as that described for Figure 2-5. As can be seen from the figure, a slight reduction is observed in the effective viscosity but not to the same degree as the nanoparticle solution (*i.e.*, the effective viscosity does not equal that of the pure fluid at contact).

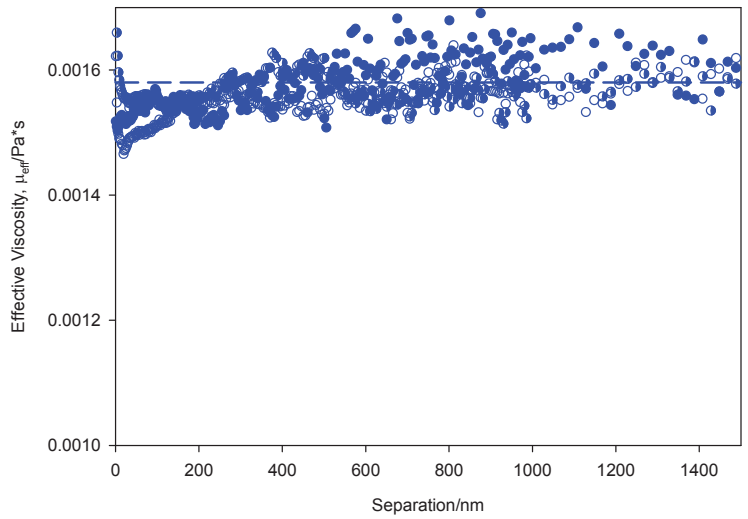

Figure B-2. Effective viscosity vs. separation distance in a 30 cmc solution of SDS micelles at varying scan speeds. The symbols represent: ● 20 μm/s, ○ 40 μm/s, amd ◑ 50 μm/s

There are several possible reasons for the differences that are observed between the SDS solution and nanoparticle solutions. The first, and likely most important reason for the differences observed, is the differences in Debye length of the SDS and nanoparticle solutions. In the SDS solutions, the Debye length is determined by the micelle physical properties and cannot be controlled as it is in the case of the nanoparticle solutions. That being the case, the Debye length of the SDS solution is only 1.75 nm. This greatly reduces the pure fluid regions around the microparticle and plate as described in section 2.6. The reduction in the pure fluid region limits its range of influence from ~25-100 nm as is the case in the nanoparticle solutions down to <10 nm for the case of the micelles. This reduction in the pure fluid region is true for not just the microparticle and plate, but also for the micelles themselves.

Additionally, the size of the micelles is much smaller than the nanoparticles. SDS micelles have a diameter of 4.0 nm. This is less than $1/5^{th}$ the size of the nanoparticles used in this work. Therefore, it would be possible for the micelles to stay in the gap region to much smaller particle-plate separation distances than was possible with the nanoparticle system. Also, due to the combination of their smaller size and smaller Debye length, the micelles could remain closer to the lubrication region of the sphere even when depleted from the gap region as contact is approached. If this is the case, this would result in a larger effective viscosity than that of the pure fluid, similar to the experimental results observed.

This result confirms the role that solution ionic strength plays in determining the effective viscosity experienced between interacting particles and surfaces. Shortening the solution Debye length not only limits the pure fluid region, but it also decreases the range of structural interactions. This decrease is further observed through reducing the depletant size, which further serves to limit the range of structural interactions.

References

1 Traube, I. Gummi Ztg. 1925, 39, 434.
2 González-Mozuelos, P.; Medina-Noyola, M. *J. Chem. Phys.* **1990**, *93*, 2109-2215.
3 González-Mozuelos, P.; Medina-Noyola, M. *J. Chem. Phys.* **1991**, *94*, 1480-1486.
4 Walz, J. Y.; Sharma, A. *J. Colloid Interface Sci.* **1994**, *168*, 485-496.
5 González-Mozuelos, P.; Alejandre, J. *J. Chem. Phys.* **1996**, *105*, 5949-5955.
6 Sharma, A.; Walz, J. Y. *J. Chem. Soc., Faraday Trans.* **1996**, *92*, 4997-5004.
7 Piech, M. Depletion and Structural Interactions in Charged Colloidal Systems. Ph.D. Dissertation, Yale University, New Haven, CT, **2003**.
8 Drelich, J.; Long, J.; Xu, Z.; Masliyah, J.; Nalaskowski, J.; Beauchamp, R.; Liu, Y. *J. Colloid Interface Sci.* **2006**, *301*, 511-522.
9 Tulpar, A.; Walz, J. *Colloids Surf., A* **2007**, *300*, 268-280.
10 Fazelabdolabadi, B.; Walz, J. Y.; van Tassel, P. R. *J. Phys. Chem. B* **2009**, 13860-13865.
11 Zeng, Y.; von Klitzing, R. *Soft Matter* **2011**, *7*, 5329-5338.
12 Richetti, P.; Kékicheff, P. *Phys. Rev. Lett.* **1992**, *68*, 1951-1954.
13 Sober, D. L.; Walz, J. Y. *Langmuir* **1995**, *11*, 2352-2356.
14 Vlachy, V. *Langmuir* **1996**, *12*, 2881-2883.
15 Subramanian, V.; Ducker, W. *J. Phys. Chem. B* **2001**, *105*, 1389-1402.
16 McNamee, C. E.; Tsujii, Y.; Matsumoto, M. *Langmuir* **2004**, *20*, 1791-1798.
17 McNamee, C. E.; Tsujii, Y.; Ohshima, H.; Matsumoto, M. *Langmuir* **2004**, *20*, 1953-1962.
18 Tulpar, A.; Van Tassel, P. R.; Walz, J. Y. *Langmuir* **2006**, *22*, 2876-2883.
19 Piech, M.; Walz, J. Y. *J. Phys. Chem. B* **2004**, *108*, 9177-9188.
20 Zeng, Y.; von Klitzing, R. *Soft Matter* **2011**, *7*, 5329-5338.
21 Milling, A.; Biggs, S. *J. Colloid Interface Sci.* **1995**, *170*, 604-605.
22 Milling, A. J. *J. Phys. Chem.* **1996**, *100*, 8986-8993.
23 Sharma, A.; Tan, S. N.; Walz, J. Y. *J. Colloid Interface Sci.* **1997**, *191*, 236-246.
24 Kuhl, T.; Guo, Y.; Alderfer, J. L.; Berman, A. D.; Leckband, D.; Israelachvili, J.; Hui, S. W. *Langmuir* **1996**, *12*, 3003-3014.
25 Milling, A. J.; Kendall, K. *Langmuir* **2000**, *16*, 5106-5115.
26 Biggs, S.; Prieve, D. C.; Dagastine, R. R. *Langmuir* **2005**, *21*, 5421-5428.
27 Rudhardt, D.; Bechinger, C.; Leiderer, P. *J. Phys.: Condens. Matter* **1999**, *11*, 10073-10078.
28 Bechinger, C.; Rudhardt, D.; Leiderer, P.; Roth, R.; Dietrich, S. *Phys. Rev. Lett.* **1999**, *83*, 3960-3963.

29 Mao, Y.; Cates, M. E.; Lekkerkerker, H. N. W. *J. Chem. Phys.* **1997**, *106*, 3721-3729.
30 Helden, L.; Koenderink, G. H.; Leiderer, P.; Bechinger, C. *Langmuir* **2004**, *20*, 5662-5665.
31 Piech, M. *J. Colloid Interface Sci.* **2000**, *232*, 86-101.
32 Odiachi Jr., P. C.; Prieve, D. C. *Colloids Surf., A* **1999**, *146*, 315-328.
33 Brenner, H. *Chem. Eng. Sci.* **1961**, *16*, 242-251.
34 Cox, R. G.; Brenner, H. *Chem. Eng. Sci.* **1967**, *22*, 1753-1777.
35 Bhattacharya, S.; Blawzdziewicz, J. *J. Chem. Phys.* **2008**, *128*, 214704.
36 Goldman, A. J.; Cox, R. G.; Brenner, H. *Chem. Eng. Sci*. **1967**, *22*, 637-651.
37 Chan, D. Y. C.; Horn, R. G. *J. Chem. Phys*. **1985**, *83*, 5311-5324.
38 Brown, M. A.; Smith, A. L.; Staples, E. J. *Langmuir* **1989**, *5*, 1319-1324.
39 Brown, M. A.; Staples, E. J. *Langmuir* **1990**, *6*, 1260-1265.
40 Frej, N. A.; Prieve, D. C. *J. Chem. Phys*. **1993**, *98*, 7552-7564.
41 Pagac, E. S.; Tilton, R. D.; Prieve, D. C. *Chem. Eng. Commun*. **1996**, *150*, 105-122.
42 Adamcyzk, Z.; Dabros, T.; Czarnecki, J.; Van de Ven, T. G. M. *Adv. Colloid Interface Sci.* **1983**, *19*, 183-252.
43 Walz, J. Y.; Suresh, L. *J. Chem. Phys.* **1995**, *102*, 10714-10725.
44 Oetama, R. J.; Walz, J. Y. *J. Chem. Phys.* **2006**, *124*, 164713.
45 Honig, C. D. F.; Ducker, W. A. *J. Phys. Chem. C* **2007**, *111*, 16300-16312.
46 Oetama R. J.; Walz, J. Y. *Langmuir* **2006**, *22*, 8318-8325.
47 Russel, W. B.; Saville, D. A.; Schowalter, W. R. Colloidal Dispersions; Cambridge University Press: Cambridge,1989.
48 Van Blaaderen, A.; Kentgens, A. P. M. *J. Non-Cryst. Solids* **1992**,*149*, 161-178.
49 Scales, P. J.; Grieser, F.; Healy, T. W. *Langmuir* **1992**, *8*, 965-974.
50 Ducker, W. A.; Senden, T. J.; Pashley, R M. *Langmuir* **1992**, *8*, 1831-1836.
51 Hutter, J. L.; Bechhoefer, J. *Rev. Sci. Instrum*. **1993**, *64*, 1868-1873.
52 Bonaccurso, E.; Butt, H.-J.; Craig, V. S. J. *Phys. Rev. Lett*. **2003**, *90*, 144501.
53 Vinogradova, O. I.; Yakubov, G. E. *Phys. Rev. E*, **2006**, *73*, 045302.
54 Maali, A.; Wang, Y.; Bhushan, B. *Langmuir* **2009**, *25*, 12002-12005.
55 Henry, C. L.; Craig, V. S. J. *Phys. Chem. Chem. Phys*. **2009**, *11*, 9514-9521.
56 Bhushan, B.; Wang, Y.; Maali, A. *Langmuir* **2009**, *25*, 8117-8121.
57 Honig, C. D. F.; Ducker, W. A. *Phys. Rev. Lett*. **2007**, *98*, 028305.
58 Piech, M.; Walz, J. Y. *Langmuir* **2000**, *16*, 7895-7899.
59 Asakura, S.; Oosawa, F. *J. Chem. Phys*. **1954**, *22*, 1255-1256.
60 Trokhymchuk A.; Henderson, D.; Nikolov, A.; Wasan, D. T. *J. Phys. Chem. B*. **2003**, *107*, 3927-3937.
61 Van Winkle, D. H.; Murray, C. A. *J. Chem. Phys*. **1988**, *89*, 3885-3891.

62 Murray, C. A.; Sprenger, W. O.; Wenk, R. A. *J. Phys.: Condens. Matter* **1990**, *2*, SA385-SA388.
63 Murray, C. A.; Grier, D. G. *Annu. Rev. Phys. Chem*. **1996**, *47*, 421-462.
64 von Klitzing, R.; Thormann, E.; Nylander, T.; Langevin, D.; Stubenrauch, C. *Adv. Colloid Interface Sci.* **2010**, *155*, 19-31.
65 Tata, B. V. R.; Boda, D.; Henderson, D.; Nikolov, A.; Wasan, D. T. *Phys. Rev. E*. **2000**, *62*, 3875-3881.
66 Asakura, S.; Oosawa, F. *Journal of Polymer Science* **1958**, *33*, 183-192.
67 Garibay-Alonso, R.; Mendez-Alcaraz, J. M.; Klein, R. *Physica A* **1997**, *235*, 159-169.
68 Mendez-Alcaraz, J. M.; Klein, R. *Physical Review E* **2000**, *61*, 4095-4099.
69 Trokhymchuk, A.; Henderson, D.; Nikolov, A.; Wasan, D. T. *Langmuir* **2001**, *17*, 4940-4947.
70 Cockbain, E. G. *Trans. Faraday Soc.* **1951**, *48*, 185-196.
71 Horn, R. G. *The Journal of Chemical Physics* **1981**, *75*, 1400.
72 Iracki, T. D.; Beltran-Villegas, D. J.; Eichmann, S. L.; Bevan, M. A. *Langmuir* **2010**, *26*, 18710-18717.
73 Łuczak, J.; Jungnickel, C.; Joskowska, M.; Thöming, J.; Hupka, J. *J. Colloid Interface Sci.* **2009**, *336*, 111-116.
74 Bell, G. M.; Levine, S.; McCartney, L. N. *J. Colloid Interface Sci.* **1970**, *33*, 335.
75 Sakai, H.; Nakamura, H.; Kozawa, K.; Abe, M. *Langmuir* **2001**, *17*, 1817-1820.
76 Hansson, P.; Jönsson, B.; Ström, C.; Söderman, O. *J. Phys. Chem. B* **2000**, *104*, 3496-3506.
77 Tominaga, T.; Nishinaka, M. *J. Chem. Soc., Faraday Trans.* **1993**, *89*, 3459.
78 Abuin, E. B.; Lissi, E. A.; Núñez, R.; Olea, A. *Langmuir* **1988**, *5*, 753-757.
79 Nikolov, A. D.; Wasan, D. T. *J. Colloid Interface Sci.* **1989**, *133*, 1-12.
80 Dederen, J. C.; Van der Auweraer, M.; De Schryver, F. C. *J. Phys. Chem.* **1981**, *85*, 1198-1202.
81 Healy, T. W.; Drummond, C. J.; Grieser, F.; Murray, B. S. *Langmuir* **1990**, *6*, 506-508.
82 Pashley, R. M.; Ninham, B. W. *J. Phys. Chem.* **1987**, *91*, 2902-2904.
83 Del Castillo, J. L.; Suárez-Filloy, M. J.; Castedo, A.; Svitova, T.; Rodríguez, J. R. *J. Phys. Chem. B* **1997**, *101*, 2782-2785.
84 Lüderitz, L. A. C.; v. Klitzing, R. *J. Colloid Interface Sci.* **2013**, *402*, 19-26.
85 Herman, D.; Walz, J. Y. *Langmuir* **2013**, *29*, 5982-5994.
86 Marra, J.; Hair, M. L. *J. Colloid Interface Sci.* **1989**, *128*, 511-522.
87 Miklavic, S. J.; Chan, D. Y. C.; White, L. R.; Healy, T. W. *J. Phys. Chem.* **1994**, *98*, 9022-9032.
88 Rouzina, I.; Bloomfield, V. A. *J. Phys. Chem.* **1996**, *100*, 9977-9989.
89 Jeffery, D. J.; Acrivos, A. *AIChE J.* **1976**, *22*, 417-432.
90 Ahualli, S.; Iglesias, G. R.; Wachter, W.; Dulle, M.; Minami, D.; Glatter, O. *Langmuir* **2011**, *27*, 9182-9192.
91 Kiratzis, K.; Faers, M.; Luckham, P. F. *Colloids Surf., A* **1999**, *3*, 461-471.
92 Seebergh, J. E.; Berg, J. C. *Langmuir* **1994**, *10*, 454-463.

93 Liang, W.; Tadros, T. F.; Luckham, P. F. *Langmuir* **1994**, *10*, 441-446.
94 Radford, S. J.; Dickinson, E. *Colloids Surf., A* **2004**, *238*, 71-81.
95 Chanamai, R.; McClements, D. J. *J. Food Sci.* **2001**, *66*, 457-463.
96 Sun, X.; Danumah, C.; Liu, Y.; Boluk, Y. *Chem. Eng. J.* **2012**, *198-199*, 476-481.
97 Sharma, A.; Tan, S. N.; Walz, J. Y. *J. Colloid Interface Sci.* **1997**, *190*, 392-407.
98 Cowell, C.; Li-In-On, R.; Vincent, B. *J. Chem. Soc., Faraday Trans.* **1978**, *74*, 337-347.
99 Sperry, P. R.; Hopfenberg, H. B.; Thomas, N. L. *J. Colloid Interface Sci.* **1981**, *82*, 62-76.
100 Aronson, M. P. *Langmuir* **1989**, *5*, 494-501.
101 Ma, C. *Colloids Surf.* **1987**, *28*, 1-7.
102 Furusawa, K.; Sato, A.; Shirai, J.; Nashima, T. *J. Colloid Interface Sci.* **2002**, *253*, 273-278.
103 Feigin, R. I.; Napper, D. H. *J. Colloid Interface Sci.* **1980**, *75*, 535-541.
104 Long, J. A.; Osmond, D. W. J.; Vincent, B. *J. Colloid Interface Sci.* **1973**, *42*, 545-553.
105 Hogg, R.; Yang, K. C. *J. Colloid Interface Sci.* **1976**, *56*, 573-576.
106 Moody, C. A.; Field, J. A. *Environ. Sci. Technol.* **2000**, *34*, 3864-3870.
107 Binnig, G.; Quate, C. F. *Phys. Rev. Lett.* **1986**, *56*, 930-933.
108 Morita S., Wiesendanger R., Meyer, E. *Noncontact Atomic Force Microscopy*, 1st ed.; Springer: Berlin, 2002.
109 Butt, H.-J. *Biophys. J.* **1991**, *60*, 1438-1444.
110 Zhu, L.; Attard, P.; Neto, C. *Langmuir* **2011**, *26*, 6712-6719.
111 Honig, C. D. F.; Ducker, W. A. *J. Phys. Chem. C* **2008**, *112*, 17324-17330.
112 Smart, J. R.; Leighton, D. T. *Phys. Fluids A-Fluid* **1989**, *1*, 52-60.
113 Philipse, A. P.; Nechifor, A.; Patmamanoharan, C. *Langmuir* **1994**, *10*, 4451-4458.
114 van Bruggen, M. P. B. *Langmuir* **1998**, *14*, 2245-2255.
115 Lin, K.-h.; Crocker, J.; Zeri, A.; Yodh, A. *Phys. Rev. Lett.* **2001**, *87*, 088301.
116 Helden, L.; Koenderink, G. H.; Leiderer, P.; Bechinger, C. *Langmuir* **2004**, *20*, 5662-5665.